Pilot tone–based prospective respiratory motion correction for cardiac MRI

vorgelegt von

M. Sc.

Juliane Ludwig

ORCID: 0000-0003-4042-8071

an der Fakultät V – Verkehrs- und Maschinensysteme

der Technischen Universität Berlin

zur Erlangung des akademischen Grades

Doktorin der Naturwissenschaften

– Dr. rer. nat. –

genehmigte Dissertation

Promotionsausschuss:

Vorsitzender: Prof. Dr. Marc Kraft

Gutachter: Prof. Dr. Ingolf Sack

Gutachter: Prof. Dr. Tobias Schäffter

Tag der wissenschaftlichen Aussprache: 30. Juni 2022

Berlin 2022

Zusammenfassung

Kardiovaskuläre Erkrankungen (CVD), einschließlich Koronarer Herzkrankheit, Herzinsuffizienz, Kardiomyopathie und Myokarditis sind für 32% aller Todesfälle verantwortlich und bleiben weltweit die häufigste Todesursache (17,9 Millionen pro Jahr; WHO, 2019). In der Kardiologie ist die Magnetresonanztomographie (MRT) wegen des hervorragenden Weichteilkontrasts ein wichtiges klinisches Bildgebungsinstrument zur Differentialdiagnose.

Mit einer MR-Untersuchung können nicht-invasiv verschiedene Parameter des Herzens untersucht werden, die z.B. Aufschluss über die Funktionsfähigkeit, den Blutfluss oder die Gewebezusammensetzung geben. Dabei werden je nach Anwendungsgebiet spezielle kardiale MRT-Techniken eingesetzt. Zur Darstellung von Herzbewegungen und regionalen Herzwandbewegungsstörungen eignet sich beispielsweise die Cine-MRT, während die Beurteilung des Verlaufs einer Myokarditis mit Hilfe des T_1-Mappings möglich ist.

Von Nachteil für viele Techniken ist jedoch die für MR-Untersuchungen typisch lange Aufnahmedauer pro Bild, die hauptsächlich auf physiologische Bewegungen zurückzuführen ist. Um sicherzustellen, dass die Bildqualität nicht durch Bewegungsartefakte beeinträchtigt wird, kommt in der klinischen Praxis häufig die Atemanhaltestrategie zum Einsatz, bei der die Atembewegung unterdrückt wird. Für eine vollständige Untersuchung müssen die PatientInnen jedoch mehrere instruierte Atemanhaltephasen bewältigen, was für Kranke, ältere Menschen oder Kinder oft schwierig sein kann.

Daher wurden Methoden entwickelt, die eine kardiale MR-Untersuchung unter freier Atmung ermöglichen. Häufig basieren diese Ansätze auf einer zusätzlichen Messung eines MR-Navigators, welcher Informationen über den Atembewegungszustand liefert. Für eine kontinuierliche Messung ist der MR-Navigator jedoch ungeeignet, da seine Erfassung die Bildaufnahme unterbricht.

Eine neue Alternative für ein Bewegungssurrogat ist der Pilotton (PT). Der PT ist ein zusätzliches in den Scanner eingebrachtes RF-signal, welches während der Messung aus den aufgenommenen MR-Daten extrahiert werden kann. Die Intensität des nicht skalierten Signals ändert sich in Abhängigkeit von der Atembewegung. Daher kann der PT als Bewegungssurrogat verwendet werden. Quantitative Bewegungsinformationen, die für eine Bewegungskorrektur genutzt werden könnten, wurden mit dem PT bisher noch nicht gewonnen.

In dieser Dissertation wurde erstmals eine PT-basierte Atembewegungskorrektur für die kardiale MRT entwickelt. Auf Basis von Phantom- und *in vivo*-Daten konnte nachgewiesen werden, dass die Bewegungskorrektur mit dem PT zu einer Verbesserung der Bildqualität im Vergleich zu unkorrigierten Bildern führt.

Die zeitliche Stabilität des PT wurde für ca. 50 Minuten gezeigt. Aus einem Kalibrierungsscan wurden personenspezifische Bewegungsmodelle abgeleitet, die es ermöglichen, den qualitativen PT in ein quantitatives Signal umzuwandeln, das In-

formationen über die Atembewegung liefert. Darüber hinaus wurde ein Vergleich des PT mit anderen Bewegungssurrogaten durchgeführt. Bei einem 3D-MR-Scan verbesserte die retrospektive Bewegungskorrektur mit dem PT die Sichtbarkeit der Koronararterien ähnlich wie mit dem MR-Navigator.

Ferner wurde ein prospektiver PT-basierter Ansatz zur Bewegungskorrektur entwickelt, der schon während der Messung, eine atemangepasste Schichtmitführung (Slice Tracking) ermöglicht. Bewegungsartefakte in funktionellen Cine-Aufnahmen mit kartesischem Aufnahmeschema konnten mit dieser prospektiven Bewegungskorrektur stark reduziert werden. Das Kontrast-Rausch-Verhältnis in Bezug auf Bewegungsartefakte und auch die Kantenschärfe des Endokards verbesserten sich im Vergleich zu den unkorrigierten Bildern signifikant. Darüber hinaus wurden die linksventrikulären Blutpoolflächen bestimmt, wobei es keinen signifikanten Unterschied zwischen der Referenzmethode und dem vorgestellten bewegungskorrigierten Ansatz gab.

Ähnliche Verbesserungen wurden bei der quantitativen Messmethode T_1-Mapping erzielt. Hier wurde ein radiales Akquisitionsschema für die Datenerfassung verwendet. Ohne Bewegungskorrektur führte die Atembewegung zu einer Überschätzung der T_1-Werte im Vergleich zu den Referenzdaten, was mit der Anwendung der PT-basierten Methode korrigiert werden konnte.

Die vorgestellten Ergebnisse zeigen, dass die PT-basierte Atembewegungskorrektur robust, akkurat und vielseitig einsetzbar ist und damit zukünftigen Entwicklungen, wie beispielsweise hochauflösenden Bildgebungsstrategien unter freier Atmung den Weg ebnet.

Abstract

Cardiovascular disease (CVD), including coronary artery disease, heart failure, cardiomyopathy, and myocarditis, accounts for 32% of deaths and remains the leading cause of death worldwide (17.9 million per year; WHO, 2019). In cardiology Magnetic resonance imaging (MRI) is an essential clinical imaging tool because it provides excellent soft-tissue contrast.

MR examination can be used to examine non-invasively various parameters of the heart, providing information on, for example, functionality, blood flow, or tissue composition. Depending on the intended application, different cardiac MRI techniques are utilized. For example, cine MRI is suitable for visualizing cardiac motion and regional wall motion abnormalities, while the assessment of the progression of myocarditis can be achieved with the use of T_1 mapping.

Of disadvantage to many techniques are the long examination times mainly due to physiological motion such as breathing. To ensure that image quality is not compromised by motion artifacts, the breathhold strategy is commonly used in clinical practice. But for a complete examination, the patients must manage several instructed breath-holding phases, which can often be difficult for the sick, elderly, or children.

Therefore, methods have been developed that allow cardiac MR examination under free breathing. Often these approaches are based on an additional measurement of an MR-navigator, which provides information about the respiratory motion state. However, the MR-navigator is not suitable for continuous measurements because its acquisition interrupts the steady-state during the measurement.

A novel alternative for a motion surrogate is the pilot tone (PT). The PT is an additional RF signal introduced into the scanner, which can be extracted from the acquired MR data during the measurement. The intensity of the scale-free signal changes depending on the respiratory motion and can, therefore, be used as a motion surrogate. Nevertheless, quantitative motion information is required for motion correction.

In this thesis, a new PT-based method for respiratory motion correction for cardiac MRI was developed. Using phantom- and *in vivo* data, it was demonstrated that motion correction using the PT leads to an improvement in image quality and accuracy of quantitative parameters compared with uncorrected images.

The temporal stability of the PT was shown for at least 50 min. Subject-specific motion models were derived from a calibration scan, that allow to convert the qualitative PT into a quantitative signal providing information about respiratory motion. Furthermore, a comparison of the PT with other motion surrogates was performed. For a 3D MR scan, retrospective motion correction using the PT improved the visibility of the coronary arteries similar to the MR-navigator.

Thereafter, a novel prospective PT-based motion correction approach was developed, which enables slice tracking during the running sequence. The quantitative

PT was used to adapt the slice position during the measurement to ensure the current imaging slice follows the respiratory motion of the heart. Motion artifacts in functional cine images with Cartesian acquisition scheme could be strongly reduced with this prospective motion correction approach. The contrast-to-noise ratio with respect to motion artifacts and also the sharpness of the endocardium improved significantly compared with the uncorrected images. Furthermore, left ventricular blood pool areas were determined, and there was no significant difference between the reference breathhold method and the presented motion-corrected free-breathing approach.

Similar improvements were achieved for quantitative T_1-mapping of the myocardium. Here a radial acquisition scheme was used for data acquisition. Without motion correction respiratory motion led to an overestimation of T_1 values compared to breathhold data, which was successfully corrected with the PT-based approach.

The presented results demonstrate that PT-based respiratory motion correction is robust, accurate, and versatile, and thus may enable future developments such as high-resolution imaging strategies under free-breathing.

Contents

Abbreviations

1 | **Introduction**

In the last 60 years, the prevention, management, and treatment of cardiovascular diseases (CVD) have advanced significantly. As a result, the worldwide CVD mortality rate has already decreased by over 60%. An important factor driving this development is the use of cardiovascular magnetic resonance imaging (CMR) [1].

CMR helps physicians to diagnose cardiac diseases, such as myocardial ischemia, cardiomyopathies, myocarditis, iron overload, vascular diseases, and congenital heart disease [2]. With the use of CMR, the beating heart and heart valves, as well as coronary arteries and heart defects can be visualized and the viability of the heart muscle can be assessed. Usually various imaging techniques are utilized to depict the different cases of interest. Cine imaging, for example, is often used in clinical routine because the heart motion is captured, which enables the assessment of the heart function [3]. For the depiction of coronary arteries, 3D whole-heart imaging is often utilized, and measurements of the spatial distribution of the T_1 relaxation time allow assessment of diffuse fibrosis [4].

A major challenge of CMR is respiratory motion, as it causes artifacts in MR images that can degrade the image quality strongly, impeding medical diagnosis. Therefore, it is an important requirement for many 2D cardiac examinations that patients hold their breath to suppress respiratory motion during the acquisition. However, this can become a problem for some patient groups who cannot control their breathing behavior, e.g., children or elderly [5]. Especially patients suffering from cardiac diseases can find it very challenging to repeatedly hold their breath.

For 3D imaging, respiratory gating techniques based on the so called MR-navigator is commonly used. The MR-navigator monitors the motion of the right hemidiaphragm by an additional MR measurement, which is interleaved within the MR scan. Only data from a specific respiratory phase and not all available data are used for the final image reconstruction [6–8]. This reduces respiratory motion artifacts but leads to longer scan times.

To address this issue, respiratory motion correction methods have been developed that allow free-breathing CMR. These methods can be subdivided into retrospective and prospective approaches. Retrospective approaches apply a motion correction after data acquisition. This type of correction is suitable for 3D whole-heart imaging because motion is captured in all three spatial directions and can retrospectively be corrected. However, for 2D imaging, like cine imaging or T_1 mapping, retrospective motion correction refers only to the motion captured in the image plane, whereas a correction of through-plane motion is not possible.

To minimize through-plane motion, slice tracking, often based on the MR-navigator, can be used. Slice tracking is an efficient through-plane motion cor-

rection method, where the slice position is updated according to the respiratory motion in real-time during data acquisition. However, for the acquisition of the MR-navigator, additional radio frequency (RF) pulses are used in the acquisition sequence and, consequently, it is not applicable to continuous scans, i.e., scans that cannot be interrupted because the magnetization of the continuous scan would be disturbed.

For continuous scans, other motion surrogates describing the respiratory motion must be used. The surrogate information can be evaluated during the measurement, and thus enable a prospective respiratory motion correction. Respiratory belts, for example, are suitable for this purpose. Respiratory belts are strapped around the body and measure the change in circumference at a certain position based on an air pressure method, but they can suffer from signal drifts and are mainly used for gating rather than motion correction [9].

Recently a new approach, the pilot tone (PT) technology, was introduced to determine respiratory motion [10]. The PT is an RF signal sent into the bore of the scanner. Its signal intensity is modulated by the underlying tissue motion and it can be extracted in real-time from the acquired MR data. The PT signal is a useful tool to monitor patient motion but it does not provide any quantitative information about organ motion.

A particular advantage of the PT over the MR-navigator is, that the PT is applicable for continuous imaging sequences because image data recording does not have to be interrupted. Although the PT is an external surrogate created by a setup separated from the MR scanner, no effort must be made regarding the temporal synchronization with the MR data. Because the PT is extracted from the MR raw data, it is intrinsically synchronous with the MR acquisition.

In order to exploit the PT regarding promising new capabilities for motion navigation, it is currently being investigated for many applications. The PT has been used so far for monitoring respiratory motion [10, 11].

In this thesis the question to be addressed is: Can the PT be used for a reliable prospective respiratory motion correction for cardiac MRI?

This question divides into the following aspects:

1. The pilot tone as a qualitative signal must be converted into a quantitative signal describing the heart motion with high temporal resolution, in order to allow reliable rigid motion correction.

2. For prospective motion correction the slice position is updated in real-time during a scan. A framework must be developed which can access the PT and apply a position shift for the current slice.

3. There may still be remaining non-rigid motion, not captured with the PT, that affects the image quality. The prospective correction must, therefore, be combined with a retrospective approach to correct for residual motion.

1.1 Scope of this thesis

In this work, a novel PT-based motion correction method is developed and its application is demonstrated with 3D whole-heart imaging, 2D cine imaging and 2D T_1 mapping.

1. A PT signal is generated and analyzed regarding its robustness. The PT signal is then quantified by calibrating it to the registered motion via motion models.

2. The PT is compared to other commonly used motion surrogates, i.e., MR-navigator and respiratory belt. 3D data is motion corrected retrospectively using three surrogates.

3. Further an online-framework is developed that enables translational PT-based prospective motion correction (slice tracking). The prospective correction is presented on free-breathing 2D cine data acquired with Cartesian trajectory.

4. A non-rigid retrospective correction is performed additionally to the prospective rigid correction using a T_1 mapping sequence with radial trajectory.

1.2 Outline

This thesis contains eight chapters:

Chapter 2 The structure and physiology of the heart will be presented, as well as fast techniques to acquire cardiac MRI data. Thereafter, strategies will be discussed, that correct for cardiac- and respiratory motion during the MR acquisition. The chapter finishes with three important applications of MR in radiology and their respective use cases for the heart, 3D anatomical imaging, cine imaging and T_1 relaxation time mapping.

Chapter 3 The PT is introduced as a novel motion surrogate and the experimental setup, acquisition and signal extraction are demonstrated. In addition, the optimal parameter settings are identified to obtain a stable signal. Furthermore, a method to minimize image impairment is described and frequently occurring artifacts are presented.

Chapter 4 A calibration scan is developed to correlate the PT with the cardiac motion. Subject-specific linear motion models are derived from the data and the initially qualitative PT signal is converted into a quantitative signal which provides heart position values. Furthermore, the PT is compared with other common motion surrogates, i.e., the MR-navigator and respiratory belts. Also, the long-term stability of the PT and its robustness are evaluated on a motion phantom and healthy subjects.

Chapter 5 The three motion surrogates introduced in chapter 4 are now used for a retrospective motion correction of 3D anatomical images of the heart. In a further step, a first proof-of-concept of a PT-based prospective motion correction is performed on dynamic 2D cardiac images with transverse orientation. Also, an existing dataset of 23 subjects is analyzed with respect to the predominant respiratory cardiac motion directions.

Chapter 6 This chapter demonstrates the PT-based prospective motion correction for free-breathing cine imaging. For this clinically relevant application, various angulated (oblique) slices of the heart are recorded during continuous measurements. Phantom and *in vivo* measurements are performed, motion models are derived, and the new correction approach is applied to Cartesian cine imaging.

Chapter 7 The prospective motion correction approach is extended by an image-based non-rigid retrospective correction. The additional correction relies on motion fields and the PT. The combined approach is applied to T_1 mapping and cine imaging on a phantom and healthy subjects. The T_1 maps and cine images are reconstructed from data acquired using a continuous radial trajectory.

Chapter 8 The main results of this work are shortly presented and the challenges that still need to be overcome for future application areas are discussed.

2 | Cardiac MRI and motion

Significant advances in cardiovascular MRI have been accomplished over the past few decades. Today, various cardiac magnetic resonance imaging techniques exist, that allow non-invasive assessment of cardiac anatomy, function, tissue composition, and disease progression. Other diagnostic imaging modalities such as echocardiography or X-ray computed tomography are also available for the examination of the heart [12–14], but CMR stands out for its superior soft-tissue characterization and versatility with regards to the diagnosis and treatment assessment of patients [15].

This chapter begins with an overview of the anatomy and function of the heart as well as the challenges for cardiac MRI arising due to physiological motion associated with breathing and the heartbeat. Current methods for motion correction are discussed. Further, three common applications of MR in radiology are presented.

2.1 Anatomy and physiology of the heart

This section is based on the references [16–19].

The heart, as the central organ of the blood circuit, serves mainly as a pump to transport 5-6 liter per minute of blood through the body. The heart weighs $\approx$300 g, has a size of $\approx$ (12$\times$8$\times$6) cm and is located in the mediastinum between the lungs and the diaphragm. The longitudinal axis of the heart runs from the base to the apex. Figure 2.1A illustrates the anatomy of the heart and Figure 2.1B its position in the thorax. On the inner surface of the muscle is the endocardium, on the outer surface the epicardium, which covers the myocardium and the coronary vessels and secretes a fluid that allows the heart to move freely within the sac, the pericardium.

Anatomically, the heart consists of two ventricles, two atria, and four valves attached to connective tissue rings of the cardiac skeleton shown in Figure 2.1C. The two ventricles are separated by the septum, labeled in Figure 2.1A. The mitral and tricuspid valves (atrioventricular valves), separate the atria from the ventricles. These valves act like inlet valves. The aortic and pulmonary valves (semilunar valves) are located at the outlet of the arterial outflow tracts from the ventricles.

Coronary vessels surround the heart muscle in the shape of a crown and originate from the aorta directly after its exit from the left ventricle. They supply the heart muscle tissue with oxygen and nutrients. About 5% of the cardiac output flows through the coronary arteries. Under physical stress, blood flow can increase up to fourfold. An occlusion in the coronary arteries often results in undersupply of the heart resulting in infarction of myocardium. More information on the disease of coronary heart vessels can be found in section 2.5.

The myocardium or heart muscle contributes the majority of the cardiac mass. Its

(A)

(B)

(C)
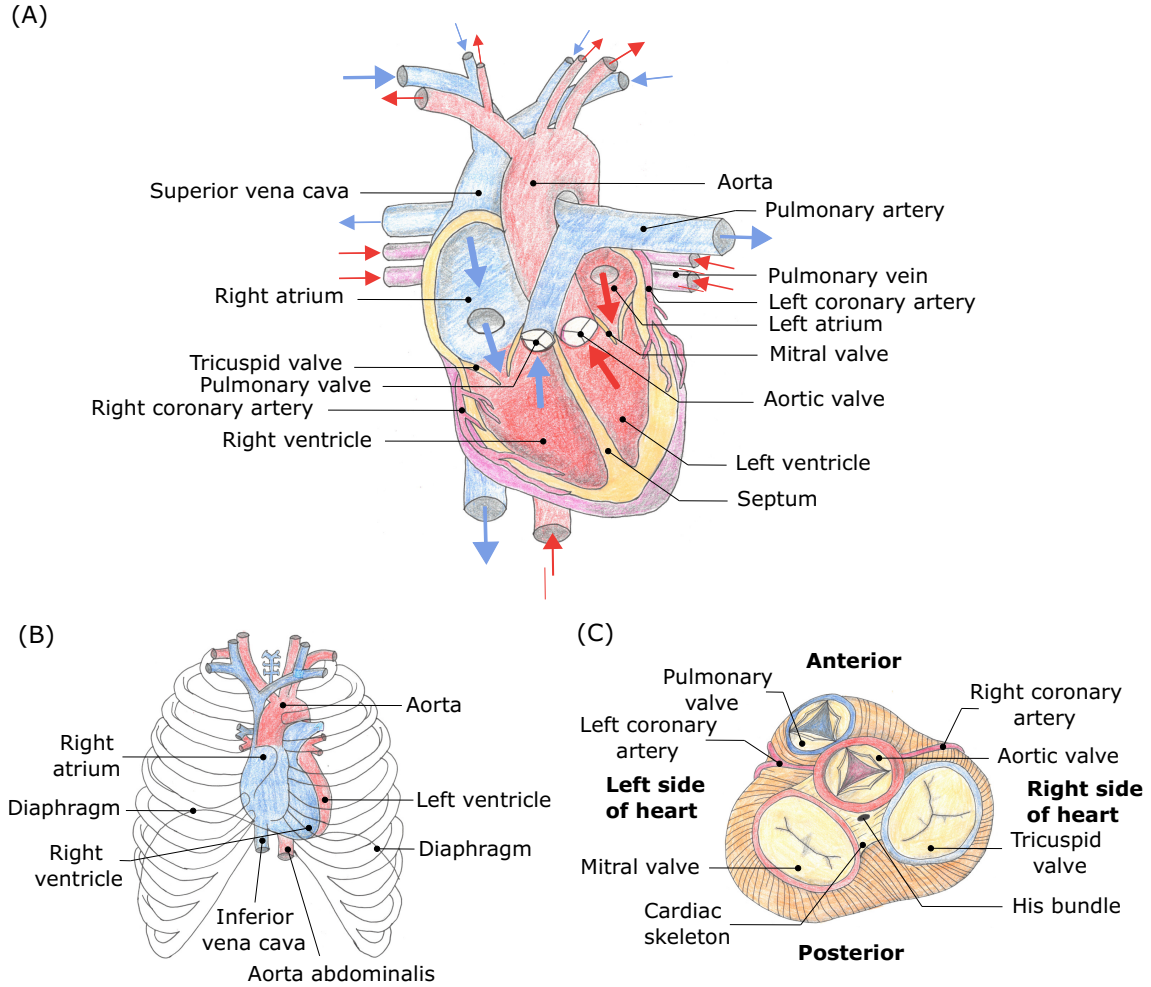
Figure 2.1: *(A) Anatomy of the heart (B) Heart position in the thorax (C) Cardiac valves. Illustration based on [16], p. 25*

glycogen-rich muscle fibers transport excitation signals, that trigger the rhythmic contractions and relaxation phases. In consequence of the contraction of the heart chambers, blood is transported through the body. Two blood flow circuits are supported by the heart, the small circuit, which is the pulmonary circuit, and the large circuit, which supplies organs and the body's periphery. Figure 2.2 illustrates the blood circulation in the body. Because the left ventricle myocardium pumps blood throughout the body circuit at higher pressure it is stronger and bigger than the right ventricle, which supplies only the pulmonary circulation at much lower pressure. The same applies to the associated valves. The pulmonary valve and the aortic valve have a similar structure, however, the aortic valve is thicker and bigger than the pulmonary valve due to higher pressure conditions and mechanical stresses.

The cardiac cycle can be separated into the two phases systole and diastole. Inlet valves control the bloodflow and pressure in the ventricles and atria. When the pressure in the ventricles exceeds the pressure in the atria, systole, i.e., the contraction phase, begins. The ventricles pump about 70 ml of blood through the aortic and pulmonary valves into the aorta and the arteria pulmonalis. After the ven-
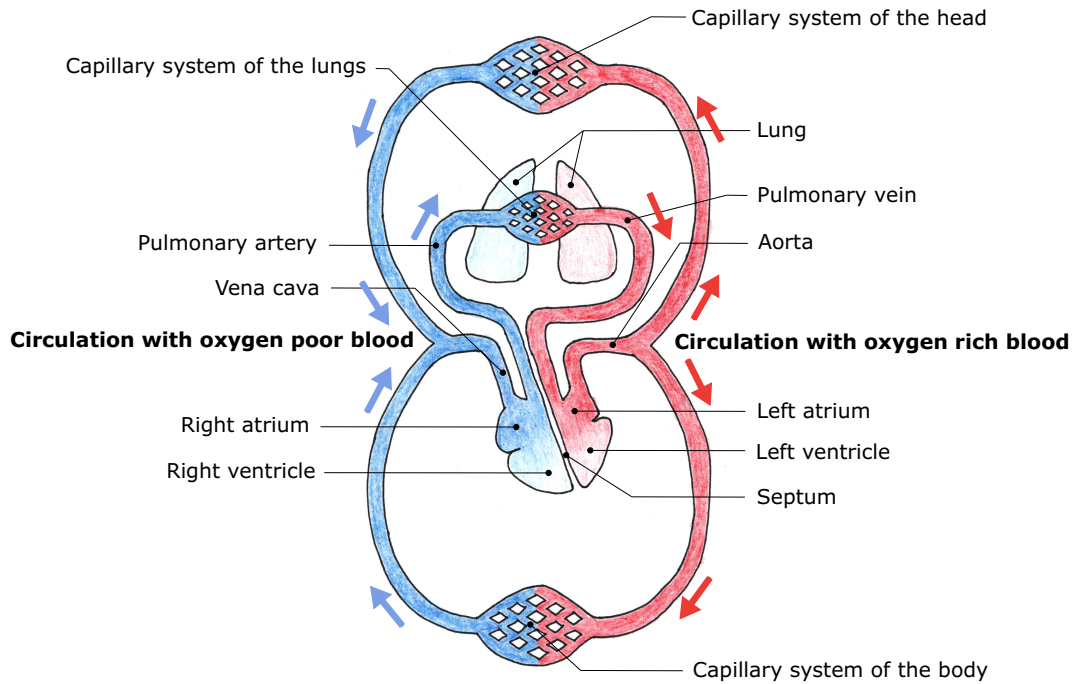
Figure 2.2: *Illustration of blood circulation in the body based on [20]*

tricular ejection the relaxation phase begins. Because the pressure in the ventricles decreased, the atrioventricular valves open to allow blood to enter from the atria into the ventricles. This ventricular filling phase is called diastole. Through the right atrium flows oxygen-poor blood, through the left atrium enters oxygen-rich blood from the pulmonary cycle. When the ventricle pressure level is above the atria pressure, the atrioventricular valves close and systole begins.

60-100 electronic impulses per minute passing through the His bundle from the atria through the septum down to the apex stimulate the heartbeat. Figure 2.3 shows an illustration of an ECG signal with indicated QRS-complex, T-wave and P-wave. The atrias systole occurs slightly earlier than the ventricles systole, and right before the R-peak of the ECG signal. The ventricles systole begins with the R-peak of the ECG signal and lasts about 400 ms [21].
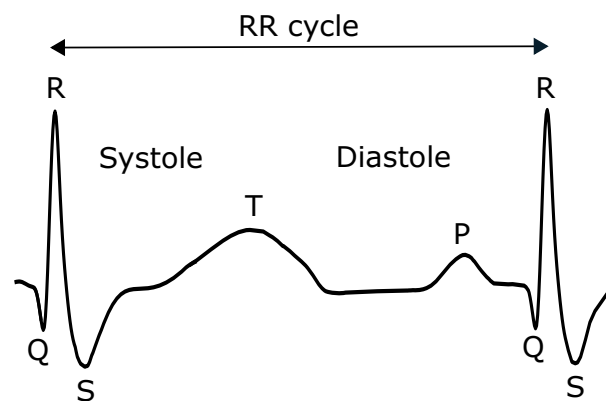
Figure 2.3: *ECG illustration with indicated systole and diastole of the ventricles*

2.2 Rapid cardiac imaging techniques

A main challenge of cardiac MRI is physiological motion. Imaging strategies have been developed that allow high-speed data acquisition, thus minimizing the effects of motion. For example, Low flip-angle gradient-echo (GRE) techniques enable very short repetition times (TR). Balanced steady-state-free-precession techniques with fully-balanced magnetic field gradients yield excellent contrast between myocardium and blood with very short scan times [22].

Multi-coil parallel imaging techniques have achieved further advancement in data acquisition speed. For cardiac imaging, the broad-use linear acquisition speed-up technique (BLAST), or k-t sensitivity encoding (SENSE), or generalized autocalibrating partially parallel acquisition (GRAPPA) are common time-saving strategies [23, 24]. Using these techniques, k-space is effectively undersampled, i.e., many k-space lines are omitted from the recording, while regions of k-space are sampled more densely. The missing k-space lines are then estimated from previously gained calibration data and/or knowledge of coil sensitivities [25, 26]. Undersampling factors correspond directly to the time saved during acquisition.

Despite these advances in imaging speed, physiological motion is still a challenge. In the following, different approaches to compensate for motion are discussed.

2.3 Cardiac motion

The heart motion can vary between heartbeats also due to the changing respiratory position in the thorax. Breathholding phases, in particular, have an influence on cardiac motion induced by heartbeat. The major components of left ventricular motion are longitudinal shortening, radial contraction, and opposite-hand rotation of the apex of the chamber relative to the base [27, 28].

Cardiac gating   Heart motion can cause image artifacts in CMR. Therefore, motion compensation strategies need to be applied. A straight forward way to minimize cardiac motion is gating. Here only k-space data of a predefined cardiac motion window and not of the entire cardiac cycle is used for image acquisition or reconstruction.

Using prospective ECG gating, the acquisition window is placed in a part of the cardiac phase where motion is minimal, i.e., in diastole. A trigger delay is predefined and valid for all heartbeats during the acquisition. The data acquisition is initiated depending on the R-peak of the ECG signal. K-space is then filled over several RR cycles.

For retrospective gating, the acquired data are resorted based on the ECG signal and assigned to cardiac phases. To record the ECG signal, electrodes are a common choice, but also other techniques, e.g., self-gating, exist, where the heart motion is retrieved from the MR data.
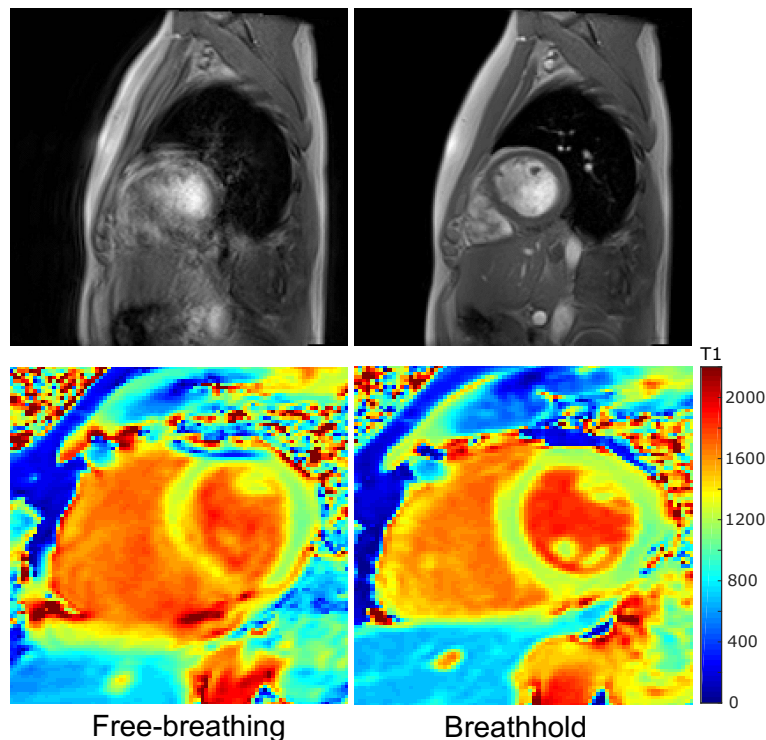
Figure 2.4: *Left: Free-breathing sagittal cine images (top) and short axis T_1 maps (bottom) with motion artifacts. Right: Breathhold data*

2.4 Respiratory motion correction approaches

Besides cardiac motion, respiratory-induced motion plays an important role in CMR. During respiration, the inflation of the lungs displaces surrounding tissue and induces cardiac motion. The most pronounced motion component is the head-feet direction [29]. Between inhalation and exhalation, the heart can be displaced about 30 mm [30].

These displacements can introduce strong motion artifacts in the reconstructed images, like ghosting, blurring, signal cancellation, or misregistration [31]. For illustration purposes, Figure 2.4 (top) shows a free-breathing cine image with impaired image quality next to a breathhold image. Exemplary T_1 maps are shown at the bottom of the figure.

In clinical routine, to reduce respiratory motion artifacts, often instructed breath-holding (10-30 s) is performed when acquiring heart images [32, 33]. To cover the whole heart or achieve a higher signal-to-noise ratio (SNR) or resolution, multiple breathholds are required [34]. This implies the need for dedicated operator involvement and high patient collaboration [35]. Despite optimal patient engagement, respiratory drift can occur even during the breathhold phase, which also promotes artifacts [5, 36]. Further strategies have been developed to correct for drift during breathhold [28]. However, other solutions are necessary for patients who cannot hold their breath, e.g., elderly, lung diseased, or children.

Respiratory gating Respiratory gating techniques are utilized that minimize respiratory motion artifacts during free-breathing acquisitions [37]. Commonly, an MR data-based navigator is used to determine the respiratory motion state of the heart. Suitable monitoring regions are the chest wall, the heart, or the liver-lung interface.

In the clinical setting, the MR-navigator, also referred to as pencil beam or liver navigator, is the tool of choice. The MR-navigator is a 2D column of magnetization covering the right hemidiaphragm, which is frequently excited before image acquisition. The dome of the right hemidiaphragm offers good conditions for clear edge detection in the profile and the resulting motion information can be used as motion surrogate [28, 38]. One shortcoming of the MR-navigator is that the acquisition of diagnostic image information has to be interrupted for the acquisition of the navigator data [6].

In a retrospective application of the gating method, a high amount of data is recorded and the subsequent image reconstruction is based only on data acquired in the predefined breathing state [6, 37, 39].

Mostly, however, the gating method is used in real time, i.e., data is only recorded if the navigator indicates the predefined breathing state. The acquisition window is commonly set at end-exhale, because this is a quiescent and reproducible phase in the respiratory cycle [40]. This means that only a fraction of the actual scan time is used for data acquisition, resulting in low scan efficiency and an unnecessary burden on patients.

The MR-navigator technique can also be combined with prospective motion correction (slice tracking), where the acquisition scheme is adapted to the breathing motion and compensates for it. For this, the navigator information is used to update the slice position before every spin excitation [7, 41–43]. More about the slice tracking method will follow in the next paragraph and the chapters 5 and 6.

Prospective motion correction A prospective correction enables the possibility for through-plane correction and requires rapid processing [44]. Information about the respiratory cycle must be available during the measurement so that respiratory gating or a slice adaption can be performed during the running sequence.

The approach of prospective slice tracking for free-breathing MRI is very intuitive. The image slice or volume position should follow the motion of the heart in real-time [42]. This is achieved by adjusting the radio frequency (RF) pulses or the magnetic gradients accordingly [45]. For rotations, the encoding gradients must be rotated. Translational motion can be corrected by adjusting the transmit and receive frequencies and -phases [46, 47]. A correction of linear expanding objects is achieved by scaling the readout gradient [48].

Different regions in the body, e.g., liver or heart, move differently due to respiration. Slice tracking can improve image quality only for areas that move like the tracked slice. If the slice tracking is, for example, applied for the moving heart, static anatomies (e.g, spine and back) will be wrongly corrected and artifacts will

be introduced. The steady-state magnetization is preserved in the moving region of interest (ROI) by slice tracking, whereas other regions may not achieve steady-state magnetization.

For more information on prospective motion correction, please refer to chapters 5 and 6, where the slice tracking method is explained in detail. The section 5.2.3, deals with the specifics of the implementation.

Retrospective motion correction   While prospective correction methods avoid the corruption of data by motion during the measurement, retrospective corrections allow to compensate for motion after the measurement.

The commonly utilized strategy for free-breathing acquisitions is retrospective gating [49, 50], which may lead to low scan efficiencies.

However, with the possibility of high computational power, retrospective motion corrections incorporate sophisticated motion models, that enable, for example, high-resolution motion registration and iterative motion correction for non-rigid motion [45]. These approaches can provide scan efficiency to almost 100% by applying motion fields to the recorded data [51, 52]. In principle, motion trajectories may be estimated intrinsically from the measured data or from a navigator. Based on the motion information the acquired data can be subdivided into small subsets each containing data of an individual motion state [49, 53]. Data is then sorted into different motion bins and images are reconstructed of each individual phase separately. To correct for respiratory motion, motion fields between the binned images are estimated and the different data is transformed to the same reference motion state.

The calculated motion fields can then either be integrated into the image reconstruction [40, 54, 55] or applied afterwards [52, 56] to minimize respiratory motion artefacts in the images. Transformation models, which consider only affine transformations can even be applied before reconstruction on the k-space data [40, 57]. From the Fourier theorem, a translational motion of the heart is corrected, by multiplying a phase factor to the k-space data. A rotation of the heart results in a rotation of the k-space. Iterative approaches can improve the reconstruction scheme [58].

A major drawback of retrospective correction is that through-plane motion for 2D images cannot be corrected after the measurement. For 2D data the retrospective correction is only effective in-plane.

Motion surrogates   Information about cardiac motion is obtained by motion surrogates. As discussed in section 2.4 on respiratory gating, the MR-navigator is well suited as a motion surrogate, but cannot be applied to all sequences.

MR-independent external surrogates provide the advantage of being available regardless of the sequence.

An established modality offering high temporal resolution signals is the respiratory belt [9]. Respiratory belts are based on air pressure systems and measure the change in circumference of the patient's thorax. Prior knowledge about the breathing behavior can improve positioning. A signal phase shift is expected when using this modality, because the strongest motion component during respiration is in HF direction [51], while the respiratory belts monitor only the displacements in anterior-posterior (AP) and right-left (RL) direction. Disadvantages of respiratory belts are that signals are prone to drifts [9], patient preparation time is high and patient comfort is affected especially for those with surgical wounds.

Furthermore, there exist respiratory cushions that are positioned below the patient. These are also based on air pressure variations but monitor less of the respiratory movement because they only cover a small area of the bodies circumference [9].

There are several other external surrogates which have been proposed such as nasal airflow sensors, optical systems and ultrasound-based approaches [35, 37, 59–62].

A promising non-contact motion tracking system, which has been little explored to date is the radar. The radar's electromagnetic waves can penetrate MRI RF coils, clothing, and a few cm of tissue to register the movement of the thorax and even the heartbeat at low amplitudes ($\approx$0.1 mm). The signal is acquired simultaneously but independent of the MR data and its frequency ranges roughly between 1.5 GHz and 9 GHz [63–65].

The aforementioned external navigator strategies bear drawbacks of requiring additional patient preparation time, not being well accepted by patients or simplistic assumptions regarding the relationship between navigator signal and cardiac motion [28].

There are other MR-based methods used for motion correction that do not affect steady-state magnetization during image acquisition. The following methods rely on the principle that moving tissue impacts the RF coil impedance, and thus causes variations in receive signal [66]. In 1988 Buikman et al. exploited the RF receive coils as respiratory and cardiac motion detectors [67] and in 2010, Graesslin et al. monitored respiratory motion by using dedicated RF pick-up coils [68]. Nevertheless, the imaging sequences must be strongly modified such that the SNR of the coils is improved and motion information can be derived from the signals, which makes it difficult to easily convert it to a large number of specific MR sequences. In 2014, Andreychenko et al. observed the respiratory motion-dependent thermal noise variance of the receiver coils, which is directly linked to the impedance of the coil [69, 70]. However, a disadvantage of this method is that the RF and gradient parts of the sequence need to be switched off for the noise sampling [71].

Other MR-intrinsic methods for motion compensation include k-space-based and image-based self-navigation [72–74]. These either extract the respiratory motion information from the MR data itself or they employ separate real-time data acquisi-

tions interleaved with the MR sequence to provide instantaneous snapshots of one or more motion dimensions. Real-time navigators have been implemented in different ways [51, 75].

A 0-dimensional navigator extracted from the MR data can serve for k-space-based motion monitoring. Here, the k-space center is frequently recorded and monitored [44, 76]. This method is especially suited for non-Cartesian sampling schemes, where the k-space center is sampled multiple times and no additional RF pulse needs to be applied to acquire navigator data [73].

A 1-dimensional signal acquired on the dome of the right hemidiaphragm also proved to be useful [77]. The navigator signal can be displayed as lines of data after reconstruction. This pencil beam navigator tracks the FH motion of the diaphragm which is directly linked to the motion of the heart with a correlation factor of 0.6 [38, 50, 78, 79].

Two-dimensional or 3-dimensional image-based navigators can be obtained from low-resolution and/or highly undersampled data acquisition [80–82]. These navigators have the advantage that motion parameters can be derived directly from the cardiac region but they require dedicated navigator scan planning [29, 83].

A solution that can be used for either Cartesian or non-Cartesian sampling schemes and does not rely on sequence inherent MR pulses is the recently introduced pilot tone [10]. The PT is an additional RF signal send into the scanner by an external emitter coil. The signal is recorded in the MR data but outside the field of view, in the oversampling region of each readout. It can, therefore, be classified as a 0-dimensional navigator. Like the noise variance- and extra pick-up coil strategies, this technology is based on the variability of the coil load depending on the composition of the surrounding tissue. The PT will be discussed in detail in the next chapter.

2.5   Common applications of MR in radiology

3D anatomical imaging   The single largest cause of death in the world is coronary artery disease (CAD) [84, 85]. One characteristic of this disease, also referred to as coronary heart disease or ischemic heart disease, is the build-up of plaque in the coronary arteries, as illustrated in Figure 2.5. This results in reduced blood flow, which can lead amongst others to myocardial infarction or sudden death [84]. Preferred diagnostic modalities for the detection of CAD are echocardiograms, CT and angiograms [78, 86, 87].

With MR angiography areas of narrowing or obstruction in a coronary artery can be observed. Because MR angiography requires high spatial resolution to capture the small coronary arteries and blocked areas, it is very time consuming and hence challenging to apply in clinical routine [88]. In addition to the time it takes to acquire all the required k-space information, scan times are prolonged due to cardiac and respiratory motion, which was discussed in sections 2.3 and 2.4.
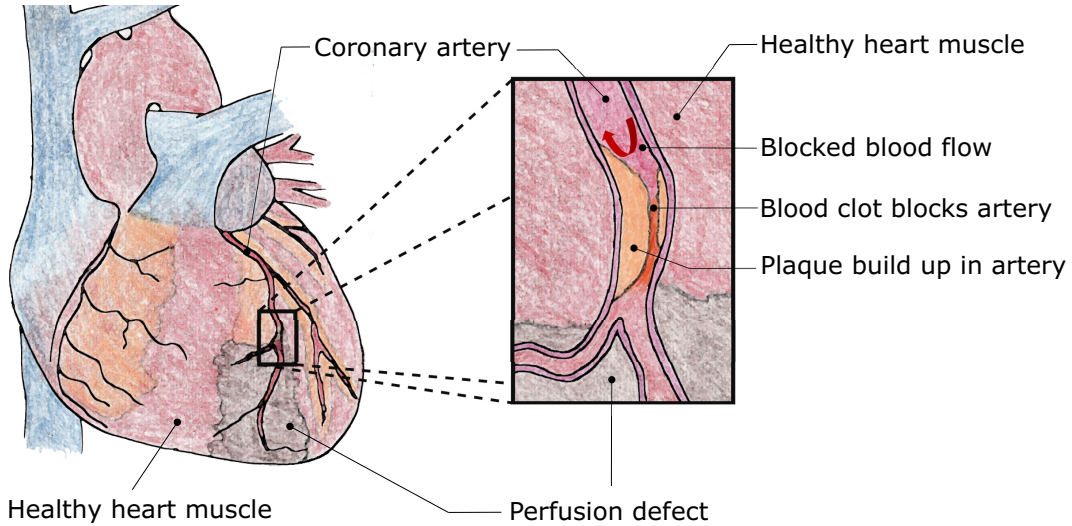
Figure 2.5: *Illustration of build-up plague in the coronary artery and blocked blood flow based on [89]*

Functional assessment   In clinical routine, cine imaging is used to visualize cardiac function, determine volume and mass and to investigate abnormal myocardial contractility [90]. With this imaging technique local defects, enlargement of the atria or abnormal tricuspid valves can be diagnosed [91, 92]. Typically, 10-30 cardiac phases are depicted for several slice positions. Cines of short axis orientation (SAX) and long axis orientation (LA) are acquired during several breathholds. For 2D cine imaging, balanced steady-state free precession (bSSFP) techniques are well suited [93]. Their contrast is proportional to the ratio T_2/T_1 leading to a high contrast between blood (high signal) and myocardium (low signal) [94], with T_1 being the longitudinal- and T_2 the transverse relaxation time. Also gradient-echo techniques are commonly used for cardiac cine imaging. These sequences avoid banding artifacts, which are often seen as a result of signal modulation due to B_0 (main magnetic field) inhomogeneity [95].

A cardiac sequence is usually ECG-triggered and continues to play out RF pulses for the complete scan period in order to maintain a steady-state magnetization.

To acquire the maximum amount of data during a scan, segmented k-space approaches are used [96], as illustrated in Figure 2.6. During several RR cycles, data of different cardiac phases are recorded until k-space for all cardiac phases has been completely scanned, which can be possible within one breathhold. Then, data is binned retrospectively to the cardiac phase using the ECG signal, and images are reconstructed for each cardiac phase specifically.

In addition to the visual evaluation of the cine images, diagnostic measures such as the ejection fraction can be calculated from the images.

For this purpose, a stack of end-diastolic and end-systolic images covering the entire left ventricle is acquired. The blood pool volumes, i.e., end-diastolic volume (EDV) and end-systolic volume (ESV), are then determined by multiplying the
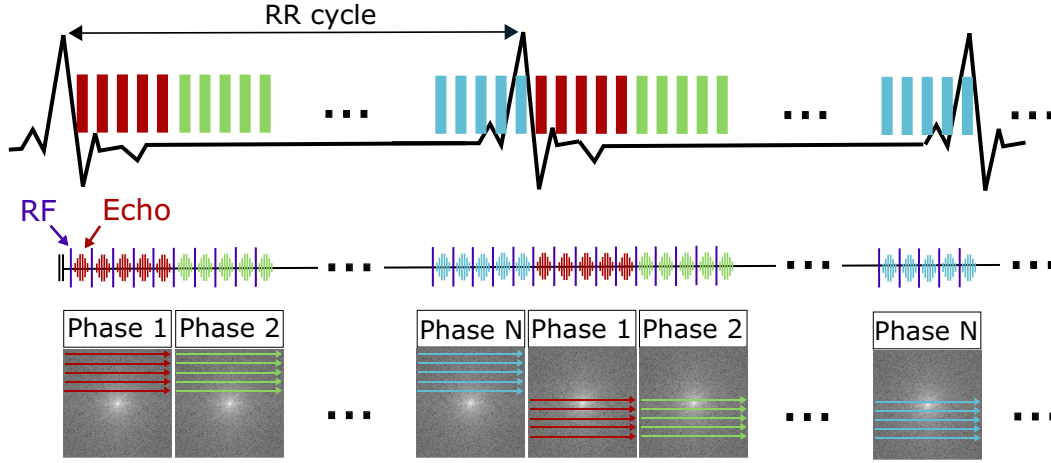
Figure 2.6: *Map of k-space demonstrates the segmented acquisition for N cardiac phases. Illustration based on [97]*

respective blood pool areas with the slice thickness and summing across all slices. The difference between EDV and ESV is the volume of blood ejected every cardiac cycle, also called stroke volume (SV) [97]:

$$SV = EDV - ESV. \tag{1}$$

The ejection fraction (EF) is then the percentage of blood ejected in each heartbeat with reference to the end-diastolic volume [98] and is calculated with

$$EF = \frac{SV}{EDV} \times 100\%. \tag{2}$$

For information about motion correction on cine imaging and calculations regarding the EF, please refer to chapter 6.

Myocardial characterization   There are several methods that are particularly useful for myocardial tissue characterization. For example, T_2 mapping is suitable for myocardial edema identification [99] and T_2^* mapping can be used for detecting myocardial iron accumulation in iron storage diseases [100]. The quantification method that will be discussed in more detail in this section is T_1 mapping. This technique is particularly suitable for the detection of fibrosis.

Fibrosis is the pathological process in which increased myocardial collagen deposition occurs as a consequence of various diseases such as hypertensive heart disease, diabetic hypertrophic cardiomyopathy and idiopathic dilated cardiomyopathy [101, 102]. Fibrosis leads to abnormalities in matrix composition and quality, and is associated with deteriorated left ventricular function, arrhythmia, and increased mortality, which are linked to heart failure and sudden cardiac death [103–105]. There are two classes of fibrosis: replacement fibrosis and diffuse interstitial fibrosis.

The reference standards for non-invasive imaging of myocardial scar and fibrosis in cardiomyopathy are Late-Gadolinium Enhancement (LGE) techniques and T_1

mapping [106–108]. Gadolinium-based contrast agents shorten the T_1 times of tissues in which they accumulate, resulting in high signal intensity in T_1 weighted images.

To detect diseased tissue, the signal of healthy and diseased regions must generate a contrast between the two tissue types. But for diffuse interstitial fibrosis, where diseased tissue can no longer be distinguished from normal healthy myocardium and no contrast can be detected, LGE imaging reaches its limits [107]. Here, the quantitative imaging method T_1 mapping can be used, also allowing comparison of tissue between different subjects or between follow-up examinations [15].

T_1 maps and T_1 weighted images rely on the T_1 relaxation time, meaning the time it takes for the longitudinal magnetization to return to the equilibrium state after excitation by an RF pulse. The longitudinal relaxation time contributes to the high degree of soft-tissue contrast in CMR and can be used for myocardial tissue quantification [109].

For a long time, only T_1 weighted images showing different voxel intensities were available to detect pathologies, such as acute myocardial infarction, chronic scar tissue or fatty infiltration in myocardial tissue. But diffuse, reactive fibrosis is characterized by an increased accumulation of collagen in the heart, which causes only very diffuse structural changes that cannot be detected with T_1 weighted images [110].

In comparison to T_1 weighted images, where a contrast is created in arbitrary units, T_1 mapping has the advantage that each voxel can be assigned a quantitative voxel value, and thus color-encoded T_1 maps can be generated. Vendors supply corresponding color maps to facilitate diagnosis.

Because T_1 depends on different tissue compositions, it is used as a biomarker for many myocardial pathological conditions such as iron overload, myocardial edema, and the presence of myocardial infarcts and scarring [110]. With T_1 mapping even diffuse fibrosis can be detected without the presence of healthy tissue [111]. T_1 values are higher for voxels containing fibrotic cells [15]. When T_1 mapping is performed before and after injection of a contrast agent, the diagnostic parameter, extracellular volume (ECV) can be determined. The ECV provides information about the relative expansion of the extracellular matrix as a result of diffuse reactive fibrosis in various cardiac diseases [110].

Also normal and fibrotic myocardium can be differentiated because T_1 times are sensitive to fibrotic changes [111].

To measure the T_1 relaxation times very accurately, several inversion recovery pulses with varying inversion times (TI) are necessary. The signal intensity SI at each TI is given by

$$SI(TI) = M_0 \left[1 - 2\exp\left(-\frac{TI}{T_1}\right) + \exp\left(-\frac{TR - TI}{T_1}\right) \right]. \tag{3}$$

But this gold-standard accurate measurement technique is very time-consuming because very long repetitions times (TR) are required to restore full longitudinal

magnetization M_0 [97]. It is, therefore, not practical in clinical routine.

A faster alternative for acquiring T_1 maps is the Look-Locker method [112]. Here, an inversion pulse is played out at the beginning of the sequence followed by a series of low flip angle α pulses. With each α pulse, the magnetization M_z is slightly flipped into the transverse direction so that a signal of $M_z \sin \alpha$ can be measured. Each application of the α pulse leads to a small loss in the total longitudinal magnetization. Therefore, instead of the longitudinal relaxation time T_1, an effective relaxation time T_1^* is obtained [113]:

$$T_1^* = \left[\frac{1}{T_1} - \frac{1}{T_R} \ln(\cos \alpha) \right]^{-1}. \tag{4}$$

With $T_R \ll T_1^*$, the equilibrium magnetization M_0 is not reached anymore, instead the effective magnetization M_0^* is determined with

$$M_0^* \approx M_0 \frac{T_1^*}{T_1}. \tag{5}$$

As M_z relaxes from $-M_0$ to M_0^*, the low flip angle pulses generate an image series that show this relaxation process [97]:

$$M_z(t) = M_0^* - (M_0 + M_0^*) \exp\left(-\frac{t}{T_1^*}\right). \tag{6}$$

The adapted Look-Locker method is the MOdified Look-Locker Imaging (MOLLI) sequence [114, 115] which is suitable for cardiac imaging within one breathhold. Figure 2.7A illustrates the original 3(3)3(3)5 scheme of the MOLLI. This breathhold scan is ECG-triggered, such that it captures data in a predefined cardiac phase, and acquired during 17 heartbeats. It starts with an inversion pulse, followed by 3 α pulses and a recovery period. This part is then repeated and after the second recovery period the third inversion pulse is played out, followed by 5 α pulses. In Figure 2.7B data is sorted according to their inversion recovery times (TI), and a T_1 model is fitted to the data. The model calculation is described by [114]. The acquired images are sorted with respect to their accumulative time from inversion (t) given by

$$t = TI + (n-1)RR, \tag{7}$$

where RR and n are the heartbeat interval and image number, respectively. Knowing the signal intensity SI, a voxelwise three-parameter fitting algorithm [116, 117] is then applied to estimate A, B and T_1^* with

$$SI = A - B \exp\left(\frac{-t}{T_1^*}\right). \tag{8}$$

T_1 can then be calculated voxel-wise with the estimated parameters using
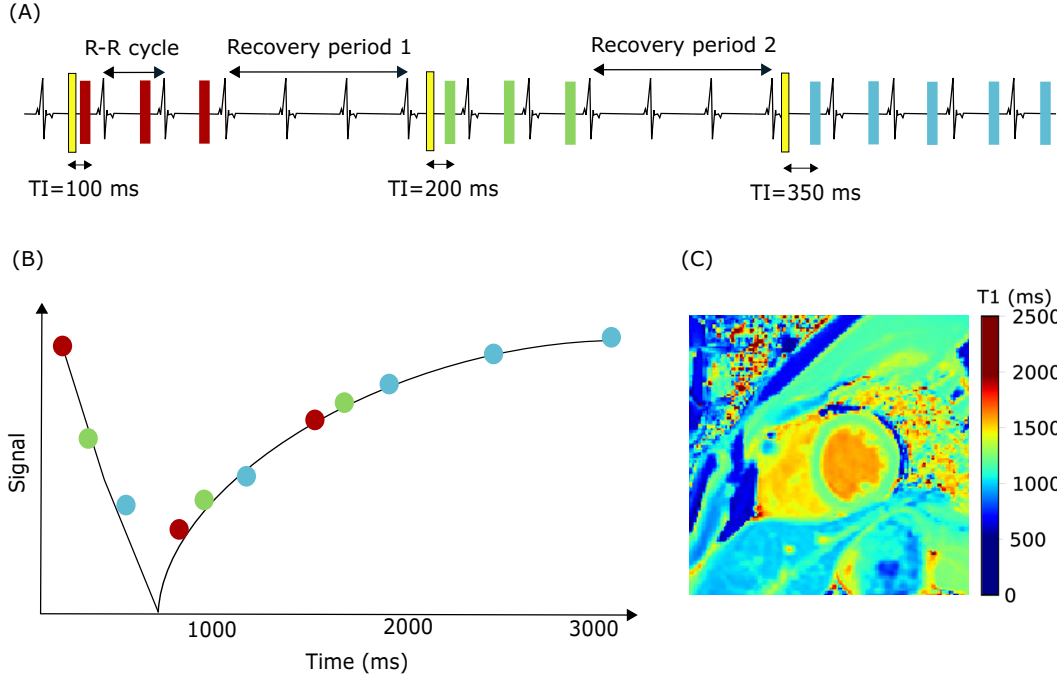
Figure 2.7: *(A) 3(3)3(3)5 scheme with Modified Look-Locker Imaging (MOLLI) overlayed on an ECG signal. The yellow bars indicate the inversion pulses, and the red, green, and blue bars are bSSFP images with α excitation pulses. (B) Images are used for the fitting of a magnitude inversion recovery model to estimate T_1. (C) a T_1 map. Illustration based on [97], p. 329*

$$T_1 = T_1^* \left[\frac{B}{A} - 1 \right]. \tag{9}$$

Figure 2.7C shows a calculated T_1 map of a heart in SAX. Besides the 3(3)3(3)5 MOLLI, there are other MOLLI scanning schemes and methods that are suitable for shorter breathhold durations, such as shortened MOLLI (ShMolli) [118]. Again other T_1 mapping methods rely on variable flip angles [119] or saturation pulses [120].

3 | Pilot tone

3.1 Introduction

The proof-of concept showing that the use of the PT could enable patient motion monitoring in the future was first published and patented in 2015 [10, 121]. Speier et al. proved on three different MR scanners that a coherent signal emitted by an external source and received in parallel with the MR signal exhibits respiratory motion patterns. The technology is based on the principle of inductive coupling between the PT emitter coil and the MR scanner's receive coils [122]. The underlying moving tissue causes coil load variations which result in small variations in the receive signals. Predominantly the respiratory motion is visible in the PT signal, but the heartbeat can also be extracted from the signal.

There have been several developments in the field of respiratory and cardiac motion detection based on the PT signal [123–125]. In particular, it was shown that the PT is independent of k-space sampling, that the PT is available with a high temporal resolution, and that the PT can map respiratory motion information of the heart [11]. It was further shown that respiratory motion could be characterized for two dimensions with the PT [11].

Further research activities focused on using the PT as a substitute for an electrocardiogram to perform cardiac triggering [123, 125]. For this approach, the cardiac signal component is separated from the respiratory signal by an independent component analysis, and an extended Kalman filter is applied to the signal to obtain a real-time noise reduced PT signal [126]. Based on *in vivo* cine images it has been shown that the PT is capable of cardiac triggering [127]. Furthermore, the PT can be used to quantify head motion [128]. In a model experiment on a volunteer, it was shown that guided "yes" and "no" motions with the head, could be discriminated with the PT.

The PT has also been used to detect respiratory motion during simultaneous PET/MR examinations and to correct retrospectively coronal diffusion-weighted images of a volunteer in 2019 [124].

Very recently, in 2020, it was demonstrated, that retrospective respiratory motion correction using the PT is feasible for abdominal magnetic resonance fingerprinting by [129].

The PT is currently an active field of research with constant advancements [122, 130]. So far it has been used for a wide range of different applications as a qualitative motion surrogate.

However, the modulation of the scale-free PT signal depending on motion is not yet sufficient if the PT ought to be used for motion correction. It must also be pos-

sible to determine a quantitative surrogate from the acquired PT signal describing
the motion of the heart with direction and on a scale.

In this chapter the feasibility of the PT to encode motion is demonstrated. The
individual goals are, to examine the PT as a motion surrogate and find its optimal
parameter settings. The parameters to be considered here are the amplitude with
which the PT is operated and the frequency. For this a test bed with a motion
phantom was build. The PT generation and acquisition is demonstrated and the
effect of the PT signal strength and frequency (i.e., location in the MR image) on the
accuracy of the PT signal is evaluated. Frequently occurring artifacts are analyzed.
Furthermore, steps are undertaken to minimize any negative impact of the PT on
the image data.

3.2 Methods

3.2.1 Phantom setup

The phantom setup is displayed in Figure 3.1. A stepper motor controlled by an
Arduino system is placed outside the scanner room (Fig. 3.1B). A rotating wheel is
attached to the stepper motor, which pulls a string. Inside the scanner room, this
string moves a wheel and via a connecting rod, a small cart is pushed back and forth.
A wooden table (Fig. 3.1C) supports the receiver coil so that the phantom can move
freely underneath. The cart performs a translational sinusoidal-like movement along
the bore direction of the scanner with an adjustable motion amplitude and velocity,
imitating translational breathing motion along the head-feet (HF) direction (Fig.
3.1A). Different agarose phantoms are used throughout this work. These are put
onto the cart and held in place with a belt.

3.2.2 Pilot tone generation

The PT is a coherent, continuous RF signal generated by an independent RF source
and transmitted into the bore of the MR scanner by an external antenna. It is
produced with a prototype set-up similar to previous applications for respiratory
gating and cardiac triggering [10]. A commercial RF synthesizer (Hewlett Packard,
ESG 1000A) is connected to a non-resonant surface coil. The power of the PT signal
is in the same order of magnitude as the received MR signal and it is about a factor
of 10^{-8} smaller than the standard RF power used for MR data acquisition.

The single loop coil, depicted in Figure 3.2A, with a loop diameter of $\approx$3 cm
was used partly in chapter 5 and was attached to the bore of the scanner. In all
other chapters the PT signal was generated with the coil depicted in Figure 3.2B
with $\approx$11 cm diameter. This coil was attached to a wooden holder that was placed
20 cm away from the head end of the bore. The head end of the scanner refers to
the scan setting head-first supine.
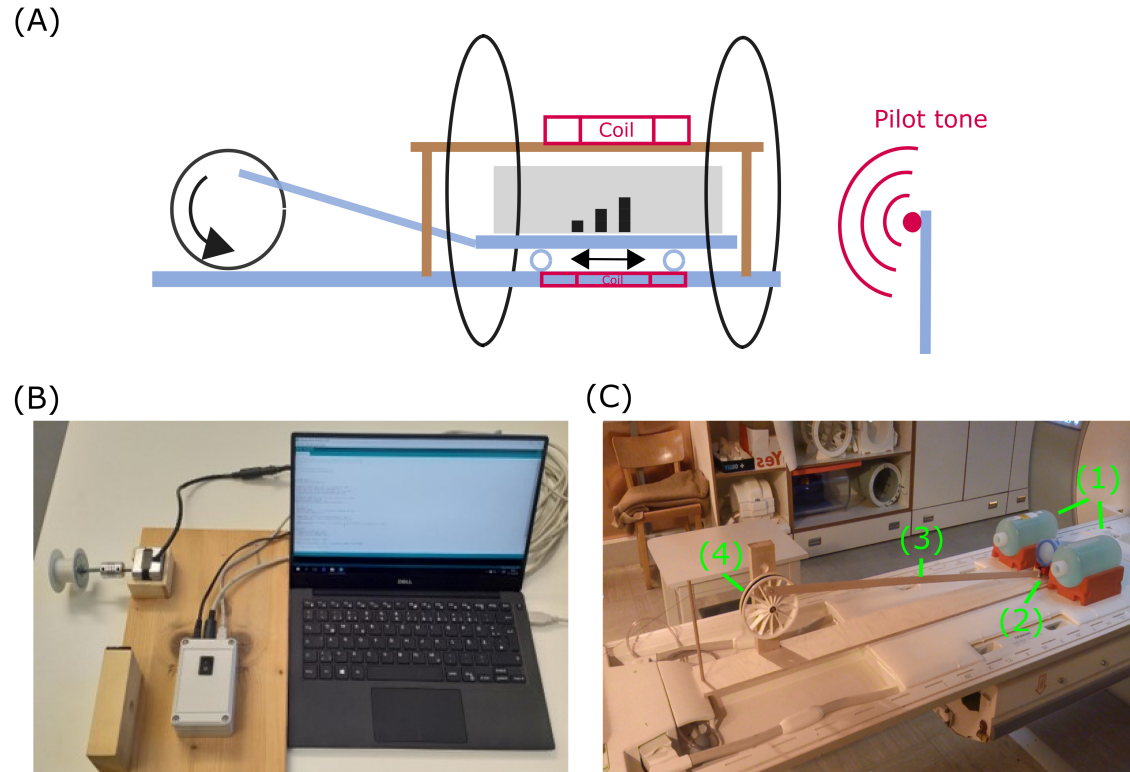
Figure 3.1: *Phantom setup. (A) One receiver coil is placed onto a fixed table above the phantom and one is integrated into the patient table. (B) The rotating wheel is attached to a string going outside of the scanner room, pulled by a controlled step motor. (C) The phantom is attached to a cart that performs translational motion along the bore direction of the scanner. (1) phantom bottles (2) moving phantom on cart (3) connecting rod (4) wheel. Parts of this figure were published in J1.*
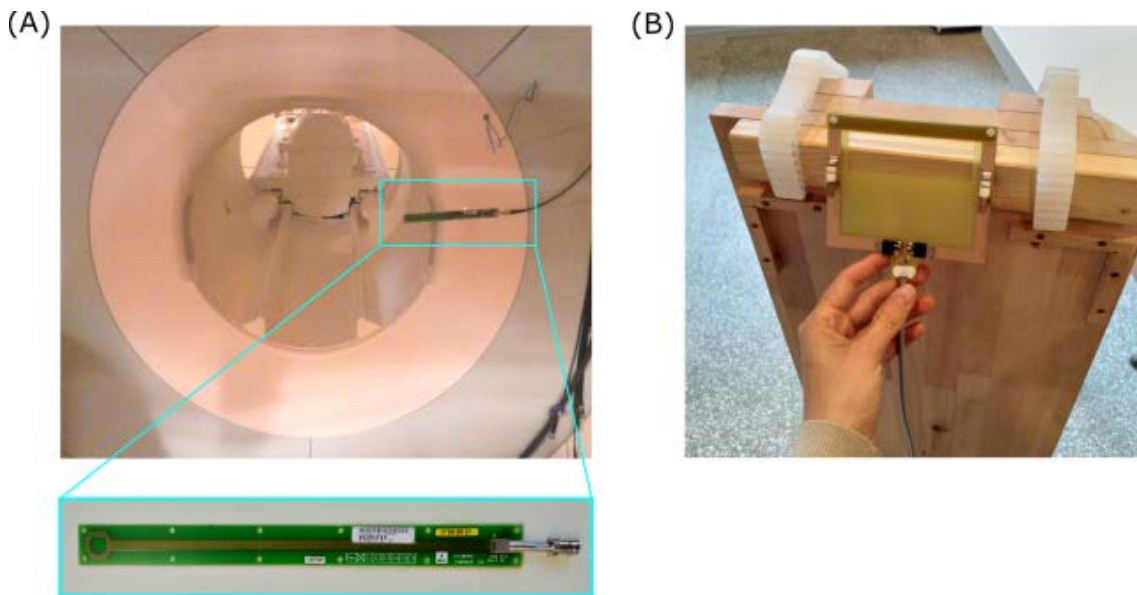
Figure 3.2: *Two different PT transmitting coils used during this thesis. One is attached directly to the bore of the scanner while the other one was placed on a wooden holder at head end of the scanner.*

The receive coil elements are sensitive to loading changes. Physiological motion [67], like breathing or the heartbeat, impacts the loading of the receive coils and the coupling between transmitter and receiver. The underlying principle is based on the different wave impedances due to different loading conditions of the receiver coils [68, 131]. The changes in local coil loading lead to changes of the received PT signal. The amplitude of the PT signal can be associated with the motion, hence, be used as a motion surrogate.

3.2.3 Pilot tone acquisition

The frequency of the PT is set close to the Larmor frequency and is picked up by the receive coil arrays that are usually placed anterior and posterior of the subject. Figure 3.3 illustrates the placement of the receiver coils for an *in vivo* scan. Each coil element records the PT signal with a different intensity, see Figure 3.4. In this scan coil 17 shows best correlation with the respiratory motion.

During an MR scan, the PT is usually acquired together with the image data. A hybrid k-space was created by 1-dim Fourier transform of the acquired k-space data along the frequency encoding direction (i.e., readout) only. In hybrid k-space all frequencies can be distinguished and signals of a single frequency can be extracted [70]. The emitted PT frequency defines the spatial position of the received PT in hybrid k-space. Figure 3.5 shows an example of hybrid k-space and the extracted PT for a moving phantom.

The PT is obtained simultaneously with each readout. Therefore, the sampling rate of the PT is one sample per TR interval which is in the region of a few milliseconds for fast gradient echo sequences.
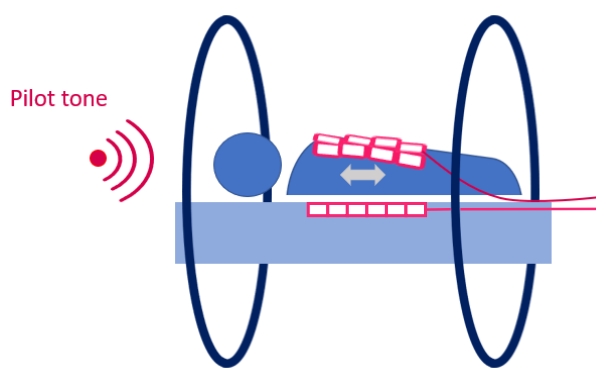
Figure 3.3: *Receiver coil setup. An anterior and posterior receiver coil array is used. Each single coil within the receiver array is surrounded by different tissue compositions and has a different distance to the PT emitter. This figure was published in J1.*
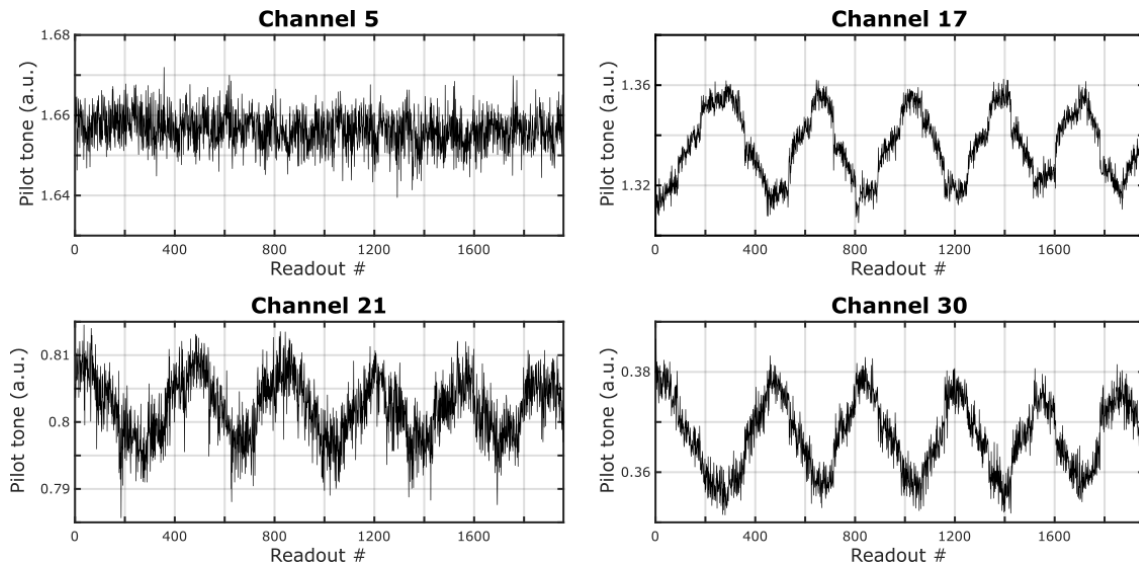
Figure 3.4: *PT obtained with four different receiver channels. Channel 17 shows highest agreement with the registered motion.*
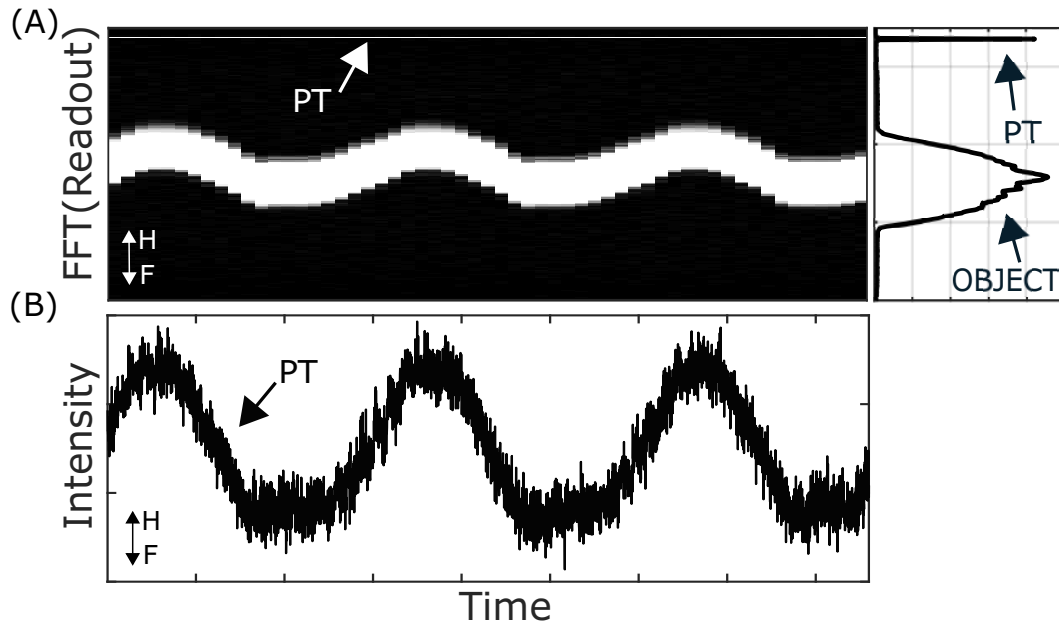
Figure 3.5: *(A) Hybrid k-space (ky=0) (i.e., k-space after Fourier transform in readout direction) of a moving phantom. In the two-fold oversampled region the PT appears as a straight line. (B) Raw PT showing variation in intensity. This figure was published in J1.*

3.2.4 Pilot tone calculation

Speier et al. have presented a method of modeling the PT first and then subtracting the modeled signal from the data to reduce the potential influence of the PT on the image [10]. This method is described and applied next.

The MRI system performs adjustment procedures to adjust for B_0 drifts prior to each scan and, therefore, the location of the PT signal in the readout can vary between different scans even for a constant PT frequency. The location of the PT can be estimated from the acquired data [132]. The readout position corresponding to the PT frequency is obtained from the hybrid k-space data by finding the highest absolute value in the oversampling region. The detected position is used to create a complex reference signal of the form:

$$A \cdot exp(i2\pi ft), \tag{10}$$

which is then scaled to match the data by multiplying the complex conjugate with the k-space data. The complex scaling factor A of the signal model is logged as the PT [10].

In order to ensure a minimum impairment of the final image by the PT, the model is subtracted from the acquired k-space data. In Figure 3.6 the measured signal, the PT model and the residual signal after subtraction are shown as profiles for one readout. Figures 3.7 and 3.8 illustrate the PT subtraction from the k-space and image data for a Cartesian and radial trajectory, respectively.

3.3 Adjustable PT parameters

Controllable parameters of the PT are the power with which it is operated and the frequency. If the power is set too high, i.e., the PT magnitude is too strong, image data may be obscured. However, if the power of the PT is set too low, the algorithm cannot extract the PT in the oversampling region because it is impaired by noise. At the signal generator the power is set in the unit dBm. The conversion between dBm and Watt is: $P(W) = 10^{\frac{P(dBm)-30}{10}}$. The frequency of the PT must be set optimally, such that the data of the object and PT do not superimpose, which would result in impaired image quality and a wrongly estimated PT signal model. In order to be able to use the PT for motion correction, both parameters, amplitude and frequency, must be optimized.
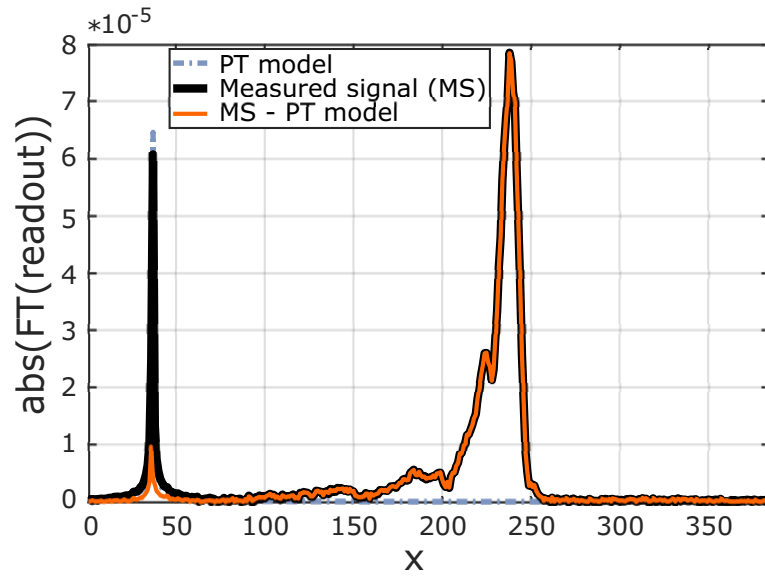
Figure 3.6: *PT subtraction for one readout*
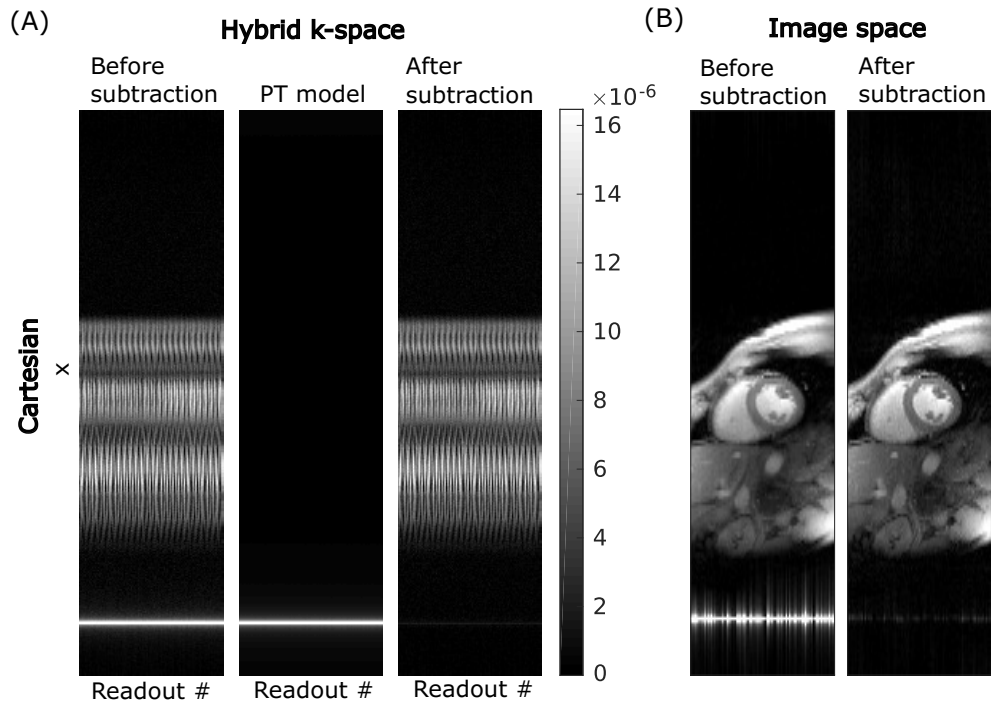
Figure 3.7: *(A) Hybrid k-space, i.e., k-space after Fourier transform in readout direction with the PT appearing as a straight line in the two-fold oversampled region obtained with a Cartesian GRE cine sequence. Only the readouts for ky=0 are shown for better visualisation. (B) Resulting image reconstructed for one cardiac phase with the oversampling region before and after PT subtraction*

(A)

Hybrid k-space

(B)

Image space
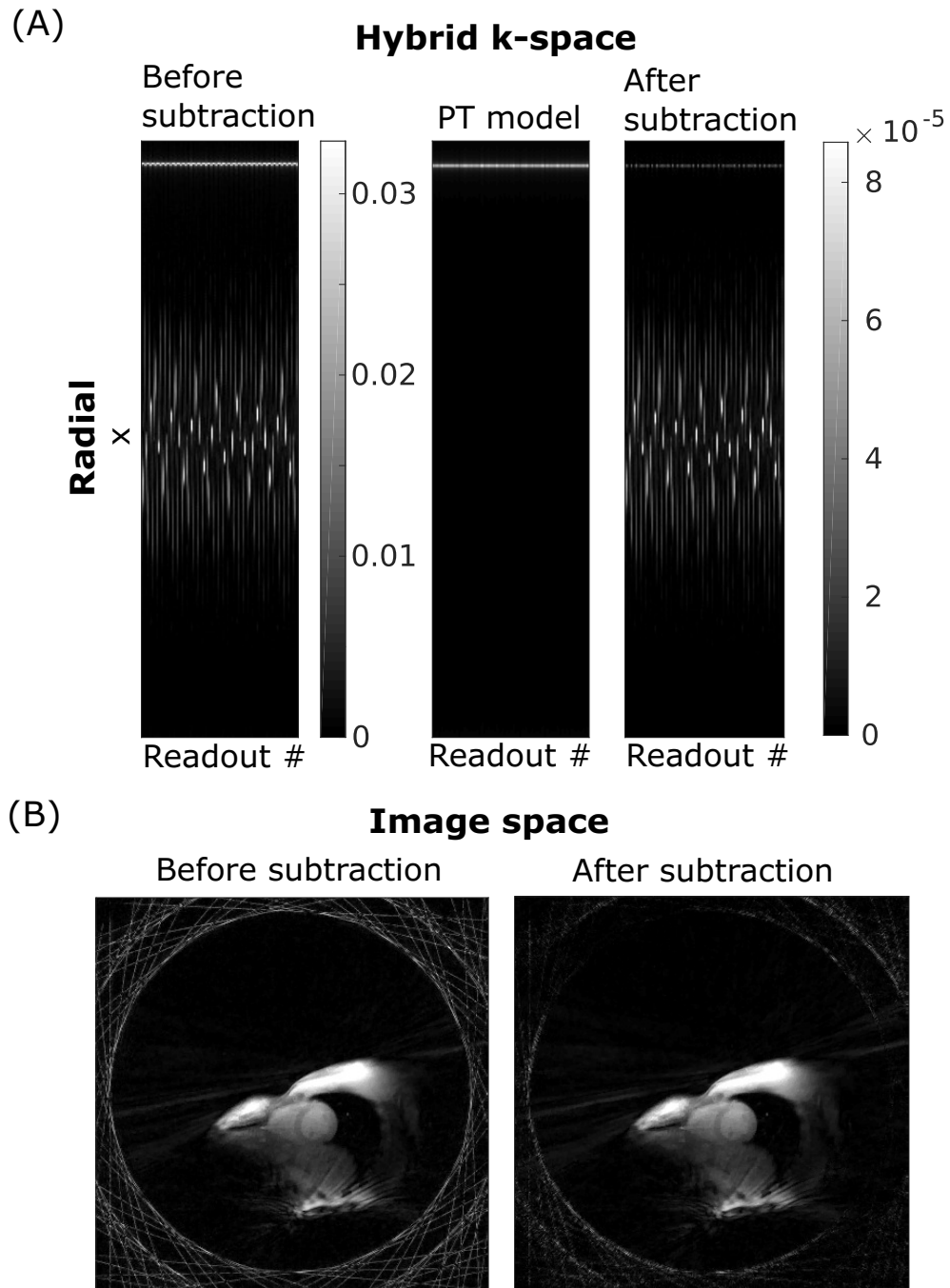
Figure 3.8: *(A) Hybrid k-space obtained with a golden-angle radial GRE sequence (B) Reconstructed image before and after PT subtraction*

3.4 Experiments

Experiments were performed with a Siemens 3T scanner (MAGNETOM Verio; Siemens Healthcare, Erlangen, Germany) on a moving 2-L agarose phantom, containing a hollowed egg-shaped region inside. Data analysis and image visualization were carried out using MATLAB 2017a (The MathWorks, Natick, MA).

3.4.1 Data acquisition

Dynamic data were acquired over 60 seconds using an in-house modified gradient-echo sequence in sagittal orientation with field of view (FOV) = $320{\times}320$ mm^2, voxel size = $1.7{\times}1.7{\times}8$ mm^3, echo time (TE) = 3.2, TR = 5.7 ms, pixel bandwidth = 449 Hz/pixel, flip angle = 12, Cartesian trajectory, and two-fold parallel imaging acceleration with 24 reference lines.

Quality assessment To determine how well the PT describes the phantom motion, it was compared to the motion estimated from a dynamic sequence. The reference motion information was determined by image registration from the reconstructed images. For this, a region of interest was set manually in the first image, and motion amplitudes in HF direction of the moving phantom were registered for the image series. A coefficient of determination, R^2, of the reference motion and the PT was calculated by fitting a linear model between PT and motion signal. R^2 denotes the proportion of the variability in the data sets, where a value of 1 indicates that the model perfectly accounts for the data. The PT was median filtered in steps of 100 data points with a sliding window. The step size was chosen to be larger than the number of phase encoding points used to capture a dynamic image (in this work). This ensures greater temporal stability throughout the measurement.

3.4.2 Optimization of PT parameters

Amplitude To prevent receiver coil saturation, the amplitude of the PT should be selected, such that the received signal intensity is of the same order of magnitude as the signal of the object. In Figures 3.6, 3.7 and 3.8, which were displayed in section 3.2.4, it could be seen, that after subtraction of the PT, there is still residual signal in hybrid k-space, which could interfere with the signals of the object. To minimize this effect, the PT amplitude should be as low as possible, but still high enough to accurately determine the motion and not be affected by noise. In order to determine the optimal signal strength, an evaluation of different PT signal strengths was carried out. Twelve different PT amplitudes ranging from -55 dBm to 0 dBm were set for 60 seconds during a phantom measurement.

Frequency In the next step, it was assessed whether the position of the PT in hybrid k-space has an influence on the accuracy of the motion model. It was assumed,

that the further out in the oversampling range, the smaller the effect of the PT on the object data. The PT was varied between a frequency range of 123.250 MHz ± 82kHz with 123.250 MHz being the center frequency of of the scanner. The edges of the FOV were captured with 123.164 MHz and 123.336 MHz.

Assessment of external influences   During the measurements, vibrations lead to small changes of distance and orientation between the PT transmitter and the receive coil array. To assess the effect of these changes, experiments were conducted with controlled disturbances of the PT transmit-receive system. A string was attached to the receive coil array and pulled from outside the scanner room during the measurement so that its position changed by <1 cm. The same procedure was performed for the PT transmit coil, causing its position to change by <1 cm.

3.5 Results

3.5.1 PT amplitude

The obtained PT signals with different amplitudes are displayed in Figure 3.9. Figure 3.9A shows the reconstructed images of five measurements. Usually, the oversampling region is removed during reconstruction, but this operation was omitted for illustration purposes. The signals in Figures 3.9B and 3.9C are realigned to be in phase for better comparison.

For evaluation, the median filtered PT signals were correlated with the motion found by image registration, as described in section 3.4.1. The last 20 data points of the measurement conducted with an emitted PT amplitude of -15 dBm were neglected due to an erroneous abrupt signal offset. Figure 3.10 shows the calculated R^2 for the twelve tested amplitudes. For an amplitude higher than -30 dBm, the signal quality indicated by R^2 does not improve further, but image quality decreases. The gray shaded area marks the values that were subsequently used in the course of this work.

3.5.2 PT frequency

Figure 3.11 shows the PT for eleven different frequencies. The FOV covered a frequency range of 123.250 MHz ±86 kHz with a pixel bandwith of 449 Hz/pixel. The frequency values in the Figures 3.11, 3.12 and 3.13 are given with respect to the center frequency of 123.250 MHz. In 3.11A an overlay of eleven hybrid k-spaces, i.e., after Fourier transform along readout direction, is shown. The position of the PT in the image varies according to the frequency. A signal overlap of the PT and the object data can be seen in Figure 3.11B for the frequencies close to the center of the FOV.

(A)

(B)

(C)
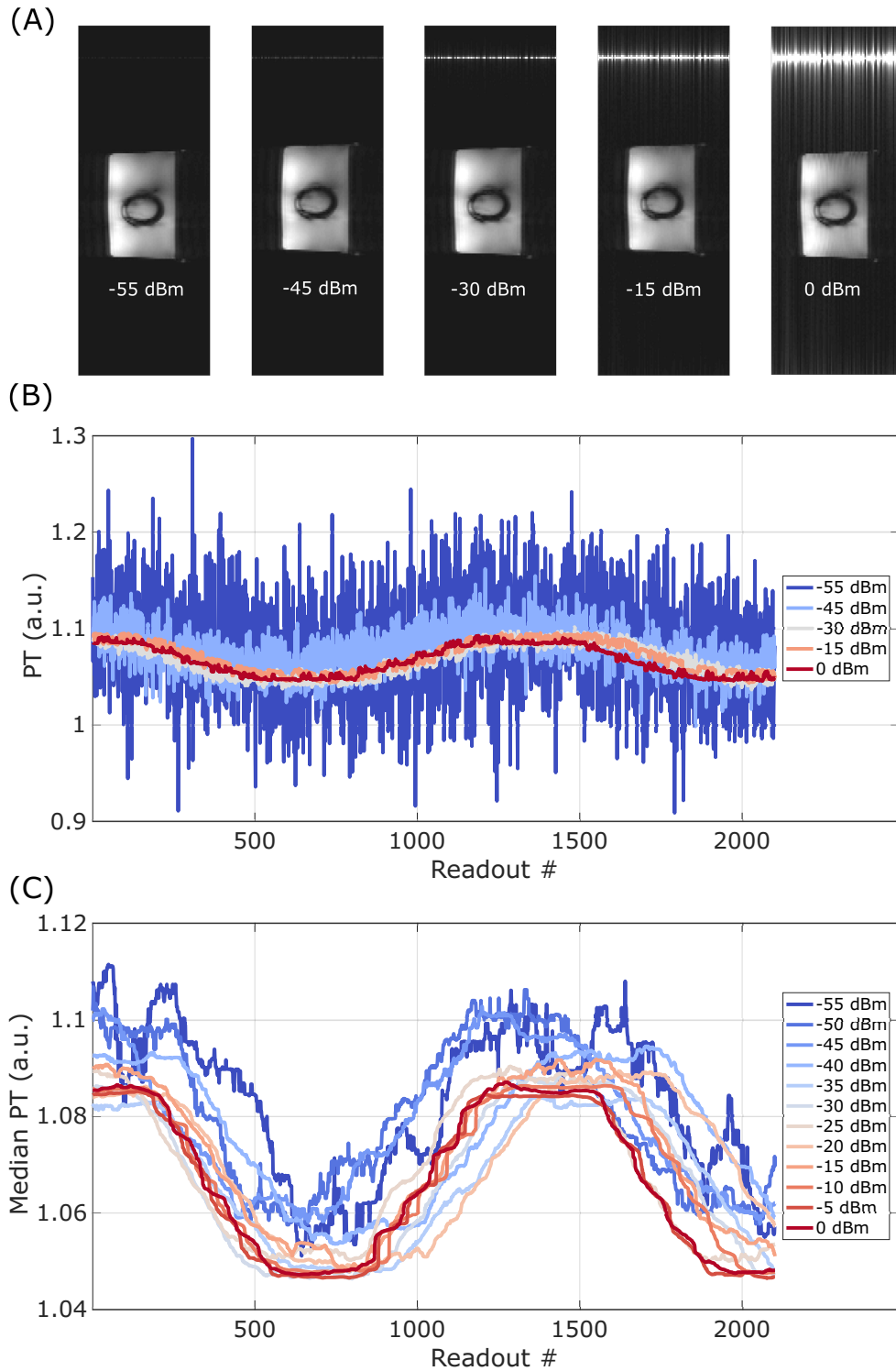
Figure 3.9: *(A) Reconstructed images showing the phantom and the the oversampling region with the PT (B) Raw PT for five different amplitudes (C) Median filtered PT of a moving phantom for twelve different signal amplitudes*
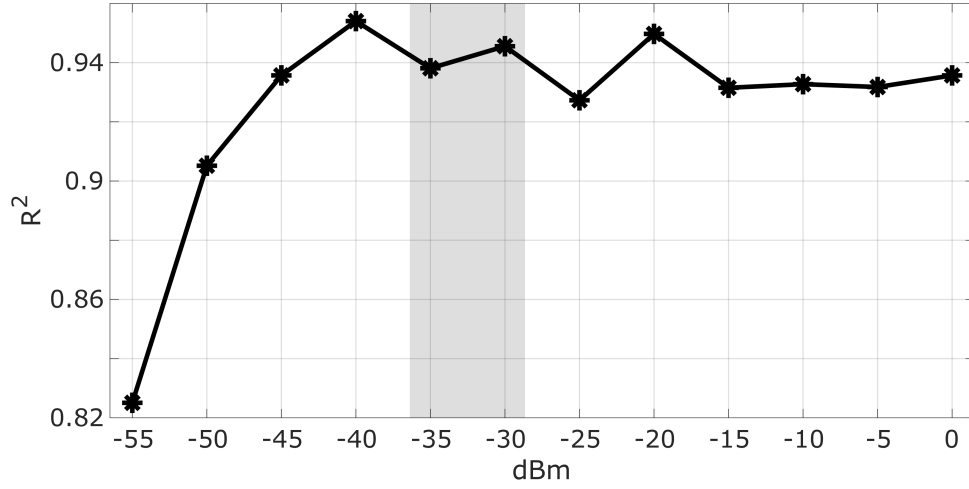
Figure 3.10: *Coefficients of determination R^2 for PT with different amplitudes and registered motion*
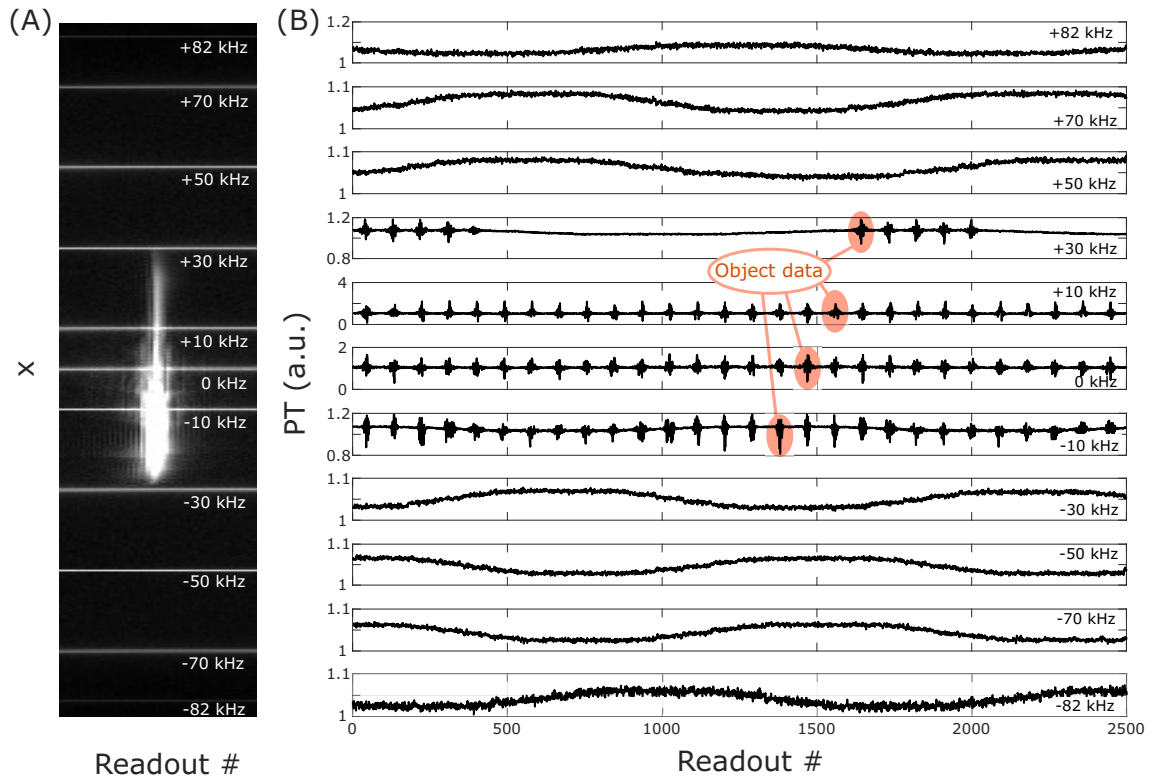
Figure 3.11: *(A) Overlay of 11 images of 77 readout lines of hybrid k-space (ky=0) (i.e., k-space after Fourier transform in readout direction) with different PT frequencies. The given values indicate the difference to the center frequency. (B) Corresponding PT signals of 2500 readouts indicating a signal overlap with the object data at the center close frequencies*
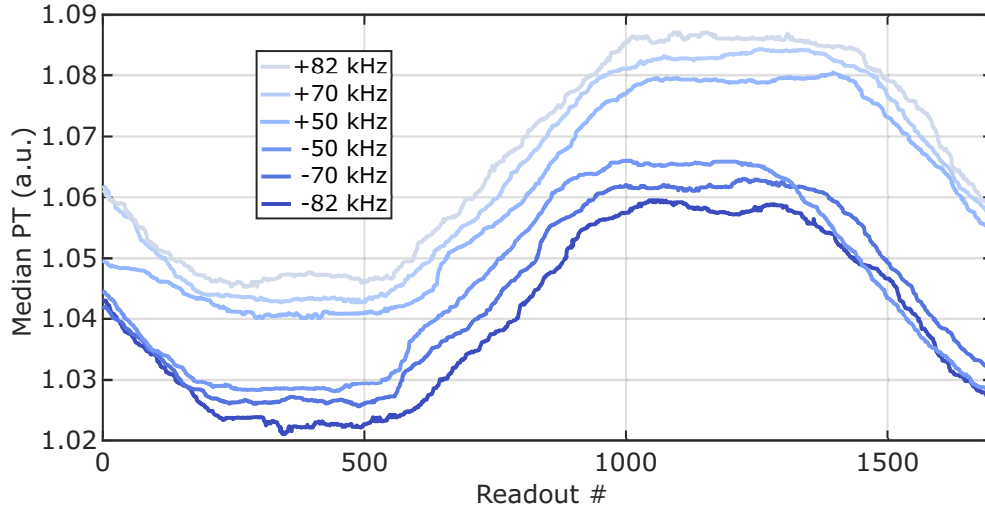
Figure 3.12: *Median filtered PT of a moving phantom for 6 different PT frequencies. The values are given with respect to the center frequency.*
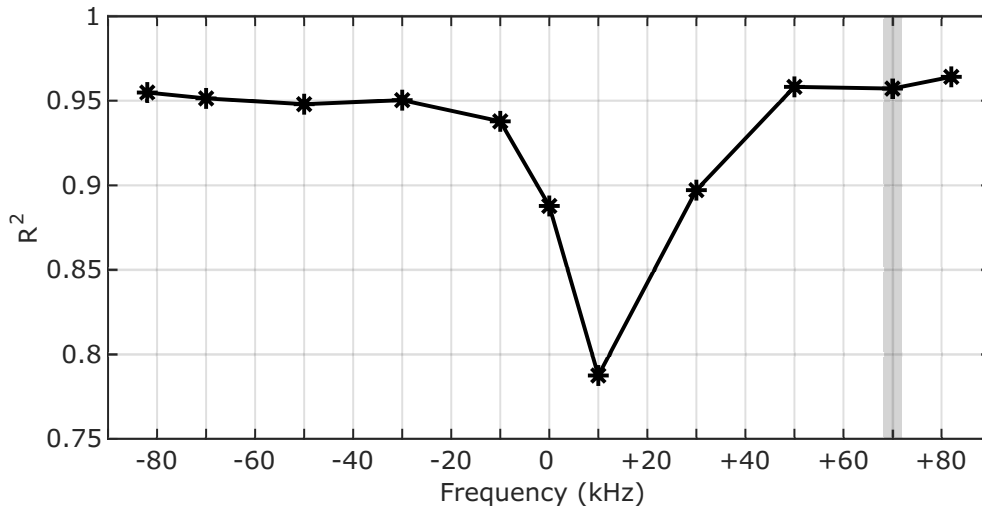
Figure 3.13: *Coefficients of determination R^2 for PT and registered motion for different frequency offsets with regard to the center frequency of 123.250 MHz*

The median filtered PT for six different frequencies is shown in Figure 3.12. The phases of the signals were aligned for better visualization. The PT variation due to motion is independent of the frequency, but there is a background offset at different frequencies.

Again the PT and the registered motion were correlated and the resulting R^2 of the motion models are shown in Figure 3.13. The correlations were best for frequency offsets away from the center frequency, that did not superimpose with the object signals. The grey shaded area marks the frequency (center frequency+70 kHz) used for further experiments with similar scan parameters (FOV, pixel size,

bandwidth). The PT was placed in the oversampling region in head end of the MR scanner because less influence of body movement which is not involved in respiration is suspected there.

3.5.3 Artifact analysis

Figure 3.14 shows the normalized unfiltered PT signals for three phantom- and one *in vivo* measurements. The first experiment was performed on a moving phantom without disturbances and the PT signal appears smooth throughout the measurement. The next two scans were actively disturbed from outside the scanner room, as described in section 3.4.2. First, the emitter coil was pulled twice via a connected string during the measurement leading to irregular spikes in the receive signal starting at readout number ≈2900. Between the disturbances, the signal maps the phantom motion and shows no spike-like artifacts. Next, the receive coil array was manipulated at the beginning of the measurement, so that artifacts are visible during the first ≈2000 readouts. The *in vivo* measurement (bottom signal in Figure 3.14) shows unintentionally caused irregular artifacts over the entire time period. These could be caused either by unwanted movement of the receiver coil arrays or the emitter coil. These cannot be distinguished from each other in terms of the received signal.

Optimizing steps for the *in vivo* measurements were to fix the receiver coil very carefully to the subject and place the PT emitter coil holder on vibration-absorbing material. Nevertheless, these vibrational disturbances could not be eliminated completely with this setup.

One approach to minimize the influence of these artifacts is the use of signal filters. As discussed by Bührer et al. in [44], for real-time applications fast filters should be used, which are causal and introduce only small delays. Bandpass filters such as a Butterworth filter could be a suitable option. In order to extract the respiratory motion signal reliably with such filters, very low frequencies must be included. However, very low frequencies also lead to a delay of the filter. To minimize the delay, high frequencies must additionally be included in the passband [44]. For this particular application, this would mean that the coherent artifacts would be considered in this filter and could distort the signal.

Due to the irregularly occurring artifacts, peak detection filters should also be avoided. For the extraction of cardiorespiratory signals from non-contact sensor data, often an adaptive Kalman filter is used [68, 125, 133]. This filter takes the probability distributions of possible errors around each signal estimate into account and previous estimates are combined with new measurement data for each time step in an optimal way. Nevertheless, this filter assumes that noise, that contaminates the respiratory signal, is Gaussian distributed [134, 135]. For an undisturbed signal, as shown in Figure 3.14(top) this filter could be an optimal choice due to its prospective behavior. For the signals that reveal vibrational disturbances, a filter must be chosen
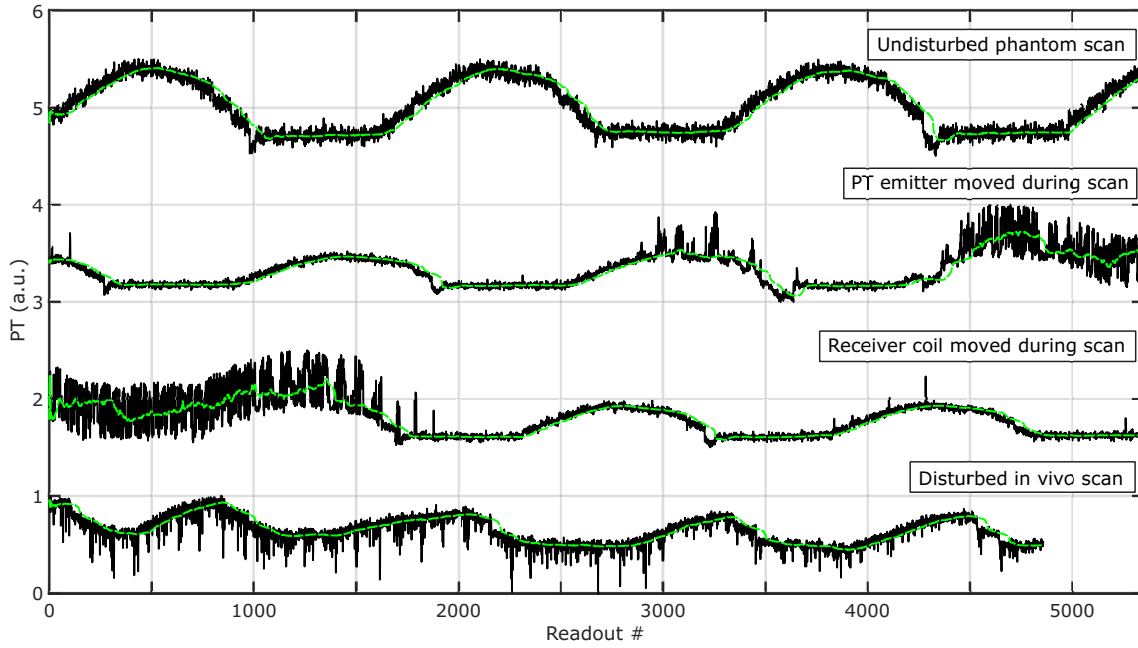
Figure 3.14: *Normalized unfiltered PT (black) and sliding window median filtered PT (green). Top to bottom: undisturbed phantom scan, phantom scan with intentionally caused disturbance on the emitter, phantom scan with intentionally caused disturbance on the receiver, in vivo scan with unwanted disturbances*

that does not take any coherence as well as artefact signal strength into account.

A sliding window median filter, see Fig. 3.14(green), with a step size of 100, minimized the effects of this specific error, because neither the intensity of the spikes nor the amount of occurrence distort the filter strongly.

3.6 Discussion

Phantom measurements have shown that high PT amplitudes suffer less from noise than low amplitudes (Fig. 3.9). However, if the PT amplitude was higher than the object signal, it affected the image quality, as illustrated in Figure 3.9A. To ensure best image quality, the PT amplitude was set to approximately the same signal magnitude as the object to be imaged. Analysis of the correlation between registered motion and PT amplitude showed high correlation values when setting the amplitude around -30 dBm (=1 μW). For further measurements during this thesis an amplitude of -30±5 dBm was chosen. The lower end of this range was used for subjects who generate a low receive signal amplitude due to their physique. The used power for the PT generation is 8 orders of magnitude smaller than the average power of MR coils, which are limited according to the standard MR safety guidelines of around 100 W (2 W/kg body weight) [136].

The position of the PT in the oversampling region did not affect its quality, as long as it did not overlap with the imaged object. The higher the frequency difference between PT and object data within the FOV, the smaller the possibility of a signal

superimposition. The PT signal quality appeared the same in both oversampling regions. For future measurements the PT frequency was set to the head end (superior side) of the FOV with a frequency offset of 70 kHz.

The PT was sensitive to small changes in the transmitter-receiver distance. In principle, every receive channel was suitable for receiving the PT. Combining the information from all receiver coils using a principal component analysis (PCA) could be less sensitive to these influences and could lead to a more robust PT. However, due to the strong and often coherent signal disturbances in the receive channels, a PCA could yield results, that emphasize the artifacts. For all future *in vivo* measurements, the PT signal was inspected at the beginning of the scan time. If strong irregular artifacts appeared, as shown in the previous section 3.5.3, the emitter or receiver coil position were optimized. This procedure was undertaken until the signal was almost free of spike-like artifacts. The R^2 of the scan gave then further information about the quality of the signal.

The applied median filter had a width of 100 readouts and reduced noise in the signal. However, within the first 100 readouts the filtered PT may give inaccurate results, because the filter is based on insufficient data. Another drawback of the median filter is the introduced delay. The sliding window filter always used the last 100 data points to determine a value. This means that a change in the raw signal was not immediately reflected in the filtered signal, but with a delay. Assuming a TR of 5.7 ms and a step size of 100 readouts, a delay of ≈ 0.6 s could be introduced between respiratory heart motion and PT signal. For adult subjects with a normal breathing rate, this delay is negligible. For infants with a breathing period of ≈ 1.2 s, this filter would need to be adapted.

The heartbeat also leads to a modulation of the PT [125]. Nevertheless, this contribution is much smaller than the contribution due to respiratory motion and is further attenuated by the applied median filter. Modulations induced by the heartbeat are neglected during this thesis.

3.7 Conclusion

In this chapter, the behavior of the PT at different settings was tested, and the best parameters for a stable PT that maps phantom motion were determined.

The next chapter presents the use of the PT as a quantitative motion surrogate. For this purpose, the signal is calibrated to the respiratory motion. Furthermore, its temporal stability is investigated and the results are compared with other motion surrogates.

4 | Calibration and temporal stability

4.1 Introduction

Parts of this chapter have been published in J1 and C1.

Commonly breathholding is the method of choice for 2D cardiac MRI to prevent respiratory motion artifacts. Even though the breathholding technique has also been proposed for high-resolution 3D acquisition of the whole heart [137], more often the respiratory gating method is applied [28, 33, 37, 39, 76]. Depending on the breathing pattern of the subject, the scan efficiency, i.e., the ratio between data used for the final image reconstruction and the rejected data, can be very low. To improve the scan efficiency, a variety of motion correction methods has been proposed that correct either prospectively or retrospectively [40, 49, 52, 54]. Nevertheless, these approaches often require dedicated data acquisition and cannot be combined with arbitrary scans.

Additionally, the main challenge remains through-plane motion. The algorithms cannot correct for tissue moving in or out of the image slice, which is especially a problem for 2D imaging and 3D imaging of a thin slab.

Accurate motion surrogates are MR-based navigators, as discussed in section 2.4. They are well suited for many applications, but not for continuous acquisitions, where the magnetization should not be disturbed by the RF pulses played out to acquire the navigator data.

Besides the MR-based navigators, external MR-independent surrogates can monitor the respiratory motion. For example respiratory belts offer a very high temporal resolution, are not coupled to the MR measurement and yield a qualitative signal [138, 139]. But in order to use the signal for motion correction, a prescan must be performed, that calibrates the signal to the respiratory heart motion via motion models [9]. Disadvantages of the use of respiratory belts are the unreliability of the signal due to sub optimal positioning, signal drifts and difficult synchronization with the MR data [9, 45].

The PT can overcome these challenges [10]. Similar to the signal obtained with the respiratory belt, the PT signal is a qualitative motion signal with high temporal resolution, which may be used for continuous scans.

In this chapter the qualitative PT signal is converted for the first time into a quantitative signal that can be used for motion correction. A calibration scan is developed, that correlates the PT signal to the translational (rigid) heart motion, and subject-specific motion models are estimated.

In a next step, the temporal stability of the PT with the motion model is examined

on a phantom and *in vivo*. Further, the performance of the PT is compared to a standard MR-navigator and a respiratory belt. For this purpose the surrogates are also tested for their stability.

4.2 Methods

This section describes how heart motion and surrogate signals can be calibrated and how the temporal stability is evaluated.

4.2.1 Calibration

To gain quantitative motion information from the qualitative surrogates the signals must be calibrated to the motion of the heart [33]. Figure 4.1 shows how image data and surrogate data are combined to estimate motion models. In this thesis the calibration scan consists of 2D images (sagittal and/or coronal), and is carried out prior to the motion-corrected MR scans. Simultaneously with the 2D images, the surrogate signals are acquired. The motion estimated from the images and the surrogate data are used to form motion models.
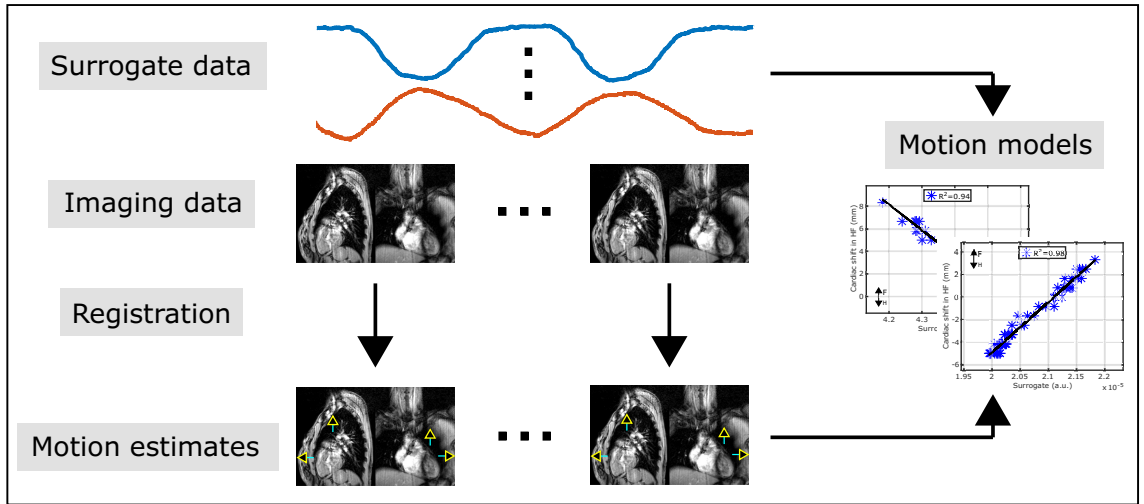
Figure 4.1: *Respiratory motion model formation. Surrogate data are acquired at the same time as MR images depicting the heart in different respiratory positions. Motion is determined from the image data by image registration, and the motion model approximates the relationship between the surrogate data and motion. Illustration based on [33]*

4.2.2 Motion model formation

Linear motion models are derived to calibrate the surrogate signals to the heart motion. Only the translational component of the heart motion is taken into consideration. Image registration with a 2D normalized cross-correlation function is used to determine the motion of the heart in HF (ΔHF_{reg}), anterior-posterior (ΔAP_{reg})

and right-left (ΔRL_{reg}) directions [49]. Three linear motion models are then derived
between ΔHF_{reg}, ΔAP_{reg}, ΔRL_{reg} and the surrogate signal (SU):

$$\Delta HF_{reg} = a \times SU + b \tag{11}$$

$$\Delta AP_{reg} = m \times SU + n \tag{12}$$

$$\Delta RL_{reg} = u \times SU + v \tag{13}$$
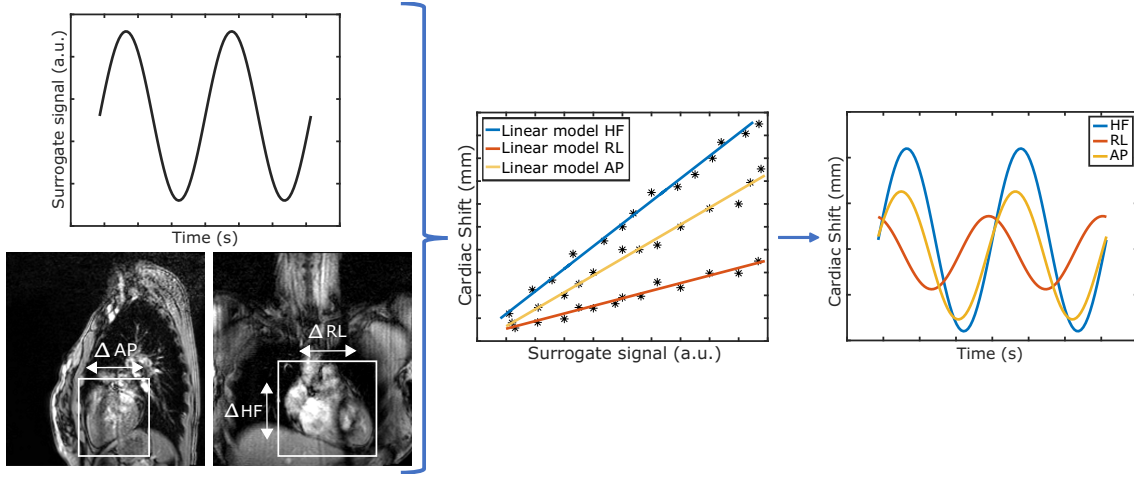
Figure 4.2: *Respiratory motion estimation. 3D respiratory translational motion in-*
formation is extracted from the respiratory-resolved images. Registered motion and the
surrogate signals are fitted by a linear regression curve. For following scans, the signals
give quantitative information about the motion state of the heart and can be used as
motion surrogates.

A PT signal is obtained with each coil element of the receiver array. For each coil
a motion model is formed. The coil which yields the motion model with the highest
coefficient of determination, R^2, for ΔHF_{reg} is selected for motion correction.

As discussed in section 3.6 a coil combination by means of PCA is not used,
because certain artifacts in the PT signal were coherent between different coils and
hence would be emphasized by a PCA. Leaving the coil signals uncombined ensured
that the coil without artifacts is selected as it most likely yields the highest R^2.

4.3   Experiments

All experiments were performed at 3T (MAGNETOM Verio, Siemens Healthcare,
Germany). The assessment of the temporal stability of the PT was performed on
a phantom and 10 healthy subjects (6 male, 4 female, age 37±13 years, weight
72±15kg). The comparison with other motion surrogates was performed on 3 sub-
jects (2 female, 1 male, age 30±2 years). The local ethics board approved the *in vivo*
experiments and written informed consent was given by all subjects. Data analysis

and image visualization were carried out using MATLAB 2017a (The MathWorks, Natick, MA).

4.3.1 Calibration scan

Sixty cardiac, ECG-triggered, dynamic sagittal and coronal 2D images were acquired for each cardiac cycle during the calibration scan as depicted in Figure 4.3. An inhouse-modified FLASH sequence was used with TE=1.4 ms, TR=2.4 ms, FOV=300x300 mm^2, FA = 20° and voxel size=1.56x1.56x8 mm^3. Data of the PT, the respiratory belts and MR-navigator were acquired together with the MR data. For synchronization of the respiratory belt data, the subjects were asked to hold their breath at the beginning and end of the scan. Only data where free-breathing was performed was then used for the formation of the motion models.
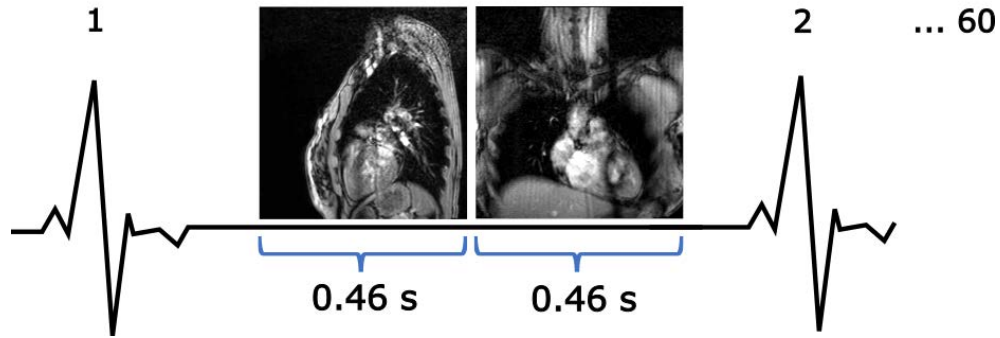
Figure 4.3: *For 60 cardiac cycles two images (sagittal, coronal) are acquired to determine the respiratory cardiac motion in three directions.*

4.3.2 Registration of motion

The cardiac motion is estimated from dynamic images. For each cardiac cycle, a coronal and sagittal 2D image with an acquisition window of 0.46 s per image were acquired to capture the 3D motion of the heart. A region of interest around the heart was chosen manually for coronal and sagittal orientation. A 2D normalized cross-correlation function was applied to the coronal image series and yielded translational motion information for the HF and RL direction. Sagittal images were used for the AP direction. Thus, respiratory motion parameters were registered for three dimensions with a temporal resolution of one value per cardiac cycle ($\approx$1 s).

4.3.3 Other motion surrogates

The PT signal was compared to two other motion surrogates: respiratory belt and MR-navigator.

Respiratory belts   Two respiratory belts, and an associated data acquisition and analysis system (MP160WS) with AcqKnowledge software (BIOPAC Systems Inc.) were used. The two belts were fixed to the subjects around the chest and abdomen to capture abdominal and thoracic breathing, as shown in Figure 4.4 (left). The change in circumference of the body during the breathing cycle was measured with an internal air pressure system providing a temporal resolution of 0.5 ms. The air pressure cables are connected to pressure to volt transducers which again were connected to an amplifier. The apparatus is shown in Figure 4.4 (right). The signals were recorded in mV and stored for further analysis. Respiratory data acquisition with the belts was started before each scan session. Temporal synchronization of the respiratory belt data with the MR data was done manually using breathhold phases as a guide. Figure 4.5 shows exemplary data of a calibration scan. Only the blue shaded area is used for calibration. At the beginning and end of a single
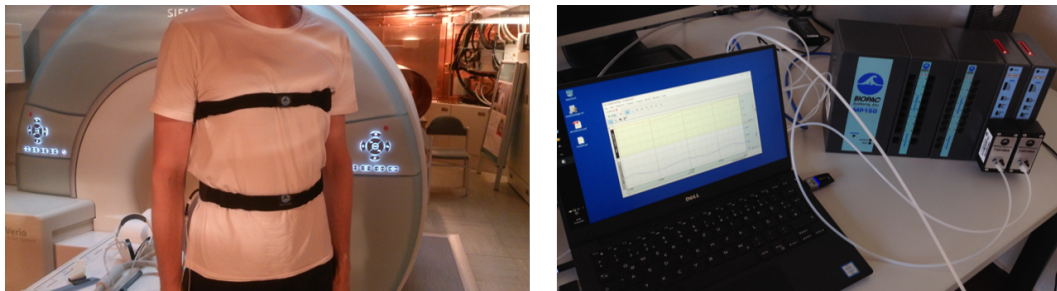
Figure 4.4: *Respiratory belt system, consisting of two belts (left) and an air pressure to volt transducer (right image, right side).*
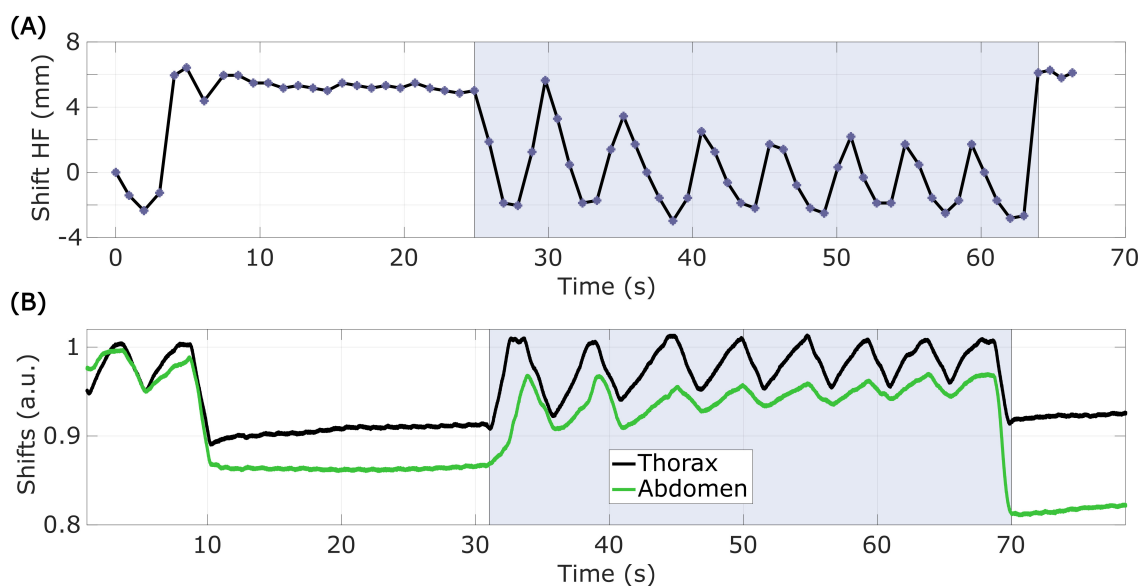
Figure 4.5: *(A) Registered HF motion of the heart obtained from 2D coronal images. (B) Continuously acquired data from two respiratory belts. The breathhold phases are clearly visible and are used for the synchronization of the respiratory belt data with the MR data.*

scan the subjects were asked to perform a breathhold and then proceed with normal breathing. These breathhold phases were identified in the respiratory belt data as well as in the MR data by analyzing the shift ΔHF_{reg} gained from the image registration. From the signal curve in Figure 4.5A, it can be seen that the heart also moves slightly during the breathhold phase (drift), which is a known occurrence shown by Xue et al. [5]. The respiratory belt that was fixed around the thorax also shows this behavior. Only data of one belt, i.e., the one which showed higher motion amplitudes during free breathing, was selected as navigator.

MR-navigator   MR-navigator data were obtained retrospectively from the calibration scan by tracking the HF motion of the dome of the right hemidiaphragm with a temporal resolution of one shift value per image. For this purpose, a rectangular region was manually selected in the reconstructed MR images with coronal orientation. The transition from the diaphragm to the lung (Fig. 4.6 (red box)) was covered and the first image served as a reference motion state. A 1D cross-correlation function was then applied to all data to show the motion of the diaphragm in the HF direction. Every image yielded one data point of the MR-navigator, as depicted in Figure 4.6 (right). The motion of the diaphragm related closely to the motion of the heart.
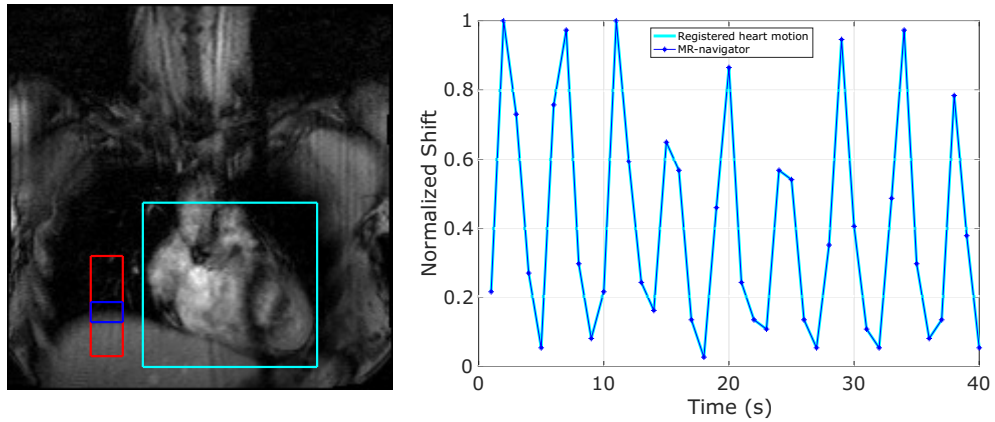
Figure 4.6: *Left: Coronal image with indicated ROI around the heart (cyan) and ROI for the MR-navigator (red). Right: Exemplary temporal evolution of the motion in HF direction for the heart and the MR-navigator. Both normalized curves overlap.*

4.3.4 Temporal stability of PT

The temporal stability was tested for the PT on a phantom and *in vivo* and also compared to other surrogates. The scan parameters for the scans performed only with the PT, and the scans performed with all three motion surrogates are summarized in Table 1. The parameters of the two scans differ because they are derived from calibration scans for different purposes. To evaluate the temporal stability of

the PT, the dynamic scan was performed for 513 RR cycles. The first 60 acquisitions of the measurement were used for calibration. Then by utilizing the motion models and the PT, the motion was predicted for all 513 RR cycles retrospectively. The motion models were not updated after initial calibration. For analysis and visualization, the values were averaged over ten RR cycles. The mean absolute error (MAE) is calculated by subtracting the predicted shift from the registered shift:

$$MAE = |\Delta HF_{pred} - \Delta HF_{reg}|. \tag{14}$$

For the *in vivo* data, the same approach was also used with $|\Delta AP_{pred} - \Delta AP_{reg}|$. The MAE depends on the temporal stability of the surrogate, the motion amplitude and the R^2 of the calibration.

Long-term measurement   Because typical clinical MRI protocols last up to one hour, the temporal stability of the PT was also examined by performing a long-term phantom scan with 6×513 repetitions.

Phantom   A 1.2-L agarose phantom containing cubic structures inside with side lengths of 0.7 cm was used. The motion phantom performed a translational sinusoidal-like movement along the HF direction of the scanner with an amplitude of ≈ 3.2 cm and a frequency of 6 repetitions per minute (0.1 Hz). The phantom was used to measure the temporal stability of the PT with the motion model.

In vivo   The temporal stability was assessed in ten healthy subjects, who were asked to perform normal continuous breathing. Additionally, one subject was asked to breathe irregularly to show different breathing patterns that were not included in the calibration. The sequence was ECG-triggered, and every sagittal dynamic image was acquired in an acquisition window of 507 ms in end-diastole.

4.3.5 Temporal stability of three surrogates

The analysis of the temporal stability of the PT, respiratory belt and the MR-navigator with their respective motion models was carried out according to Eqn. 14 based on data from the same recording, as specified in Table 1. The duration of the used scan was 350 RR cycles and two breathhold phases were included in the beginning and the end of the scan for synchronization of the data. The predicted heart shifts along HF from the three motion surrogates were then compared to the registered heart motion by examining the MAE.

Temporal stability scan	PT only (for phantom and *in vivo* study)	MR-nav, Resp. belt, PT (for comparison of surrogates)
Measurements	513	350
Triggering	ECG-triggered*	ECG-triggered*
Sequence	GRE	GRE
Orientation	2D sagittal	2D sagittal, coronal
TE/TR	3.2/5.7 ms	1.4/2.4 ms
Flip angle	12°	20°
FOV	320×320 mm^2	300×300 mm^2
Voxel size	1.7×1.7×8 mm^3	1.6×1.6×8 mm^3

Table 1: *Sequence parameter for test series on the temporal stability. *For phantom measurements an ECG signal was simulated with 1 Hz.*

4.4 Results

4.4.1 Evaluation of temporal stability of PT

Phantom   Due to the phantom setup, only motion along HF was present, and hence the analysis was limited to that direction. Figure 4.7A shows the shift found by image registration (ΔHF_{reg}) compared to the predicted shift (ΔHF_{pred}) estimated from the model and the PT. The linear regression correlation coefficient for the first 60 s was 0.95. The amplitude of the registered shift was 31.7 mm and for the predicted shift 31.7±3.7 mm. Figure 4.7B shows the evolution of the MAE. The average MAE over the complete measurement was 2.5±0.7 mm. Here it is important to note that the motion amplitude of the phantom was much larger than what would be expected *in vivo* and hence MAE is also much larger than for in-vivo applications.

In a second experiment the PT was recorded for 51.3 min during 6 scans with 513 repetitions. The total time period of the experiment was 52.75 min including small pauses to restart the sequence. The motion phantom did not move for the last ≈6 min. Figure 4.8A shows the raw PT signal acquired with one channel. The first 60 s were used to calibrate the registered shift and the raw PT, resulting in an R^2 of 0.99. Figure 4.8B displays the MAE of the PT correlated with the registered phantom shift in HF direction in steps of 10 acquisitions for the 6 scans. The mean peak-to-peak amplitude was 27.5 mm and the mean of the MAE was 1.2±0.9 mm.

In vivo   The respiratory heart motion for regular breathing was evaluated for 10 subjects in HF and AP direction from sagittal images, and the according MAE are shown in Figure 4.9. The mean R^2 of the registered and predicted shift for the first 60 RR cycles was 0.94±0.04 in HF and 0.67±0.19 in AP direction. The measurement duration of 513 RR cycles varied between 6.5 min and 11.1 min. The average peak-to-peak difference along HF of all subjects was 5.7±3.0 mm with a maximum heart
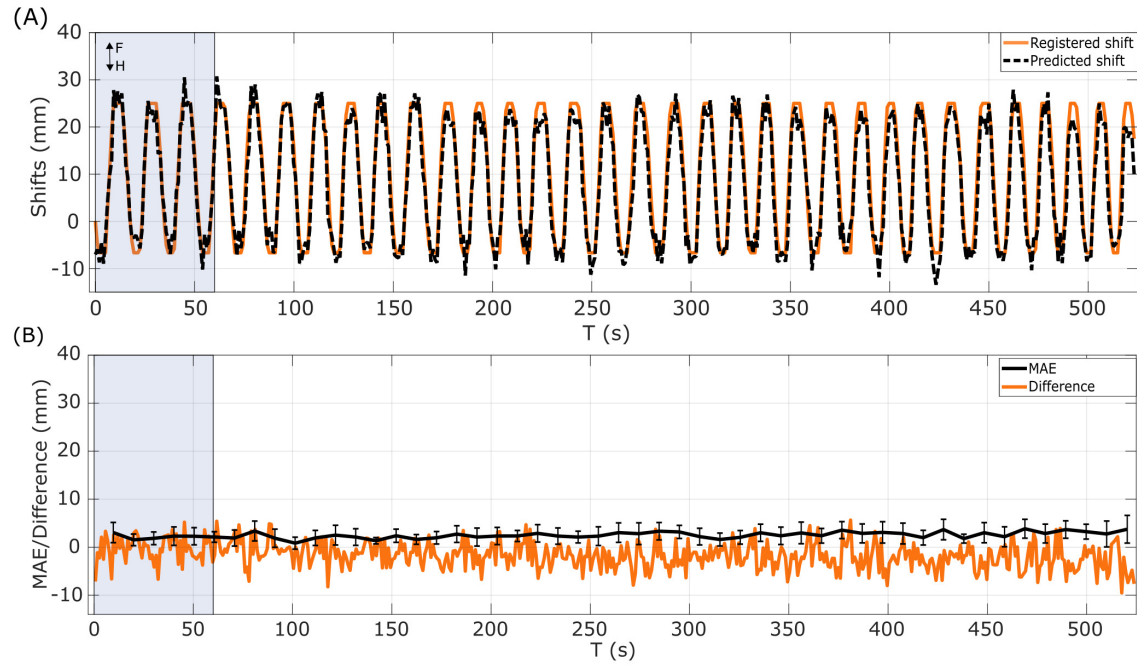
Figure 4.7: *(A) Registered phantom shift and the predicted shift for a moving phantom over 513 s. (B) Temporal stability of the motion model and difference between predicted and registered shift. The first 60 s were used to calibrate the pilot tone to the phantom motion (blue area). The motion was then predicted and compared to the registered motion. The mean absolute errors were averaged over ten images (i.e., cardiac cycles), and the corresponding standard deviations are displayed. This figure was published in J1.*

displacement of 28.3 mm. The average of the MAE along HF was 1.4±0.5 mm. For AP, the average peak-to-peak difference was 1.8±0.5 mm for all measurements with a maximum heart shift of 6.7 mm. The average MAE along AP was 0.5±0.1 mm.

Figure 4.10A shows the respiration curve in the HF direction of a subject who was asked to breathe irregularly for 6.9 min. An approximately 10-second breathhold after end-exhalation was also included in the calibration phase. The MAE of the predicted shift (ΔHF_{pred}) compared to the registered shift (ΔHF_{reg}) was <1 voxel for almost the entire measurement. Only very deep breathing led to an increase of the MAE because the deep breathing was not part of the calibration, as shown in Figure 4.10B (arrows). After the deep-breathing phase, the error decreases again.

(A)

(B)
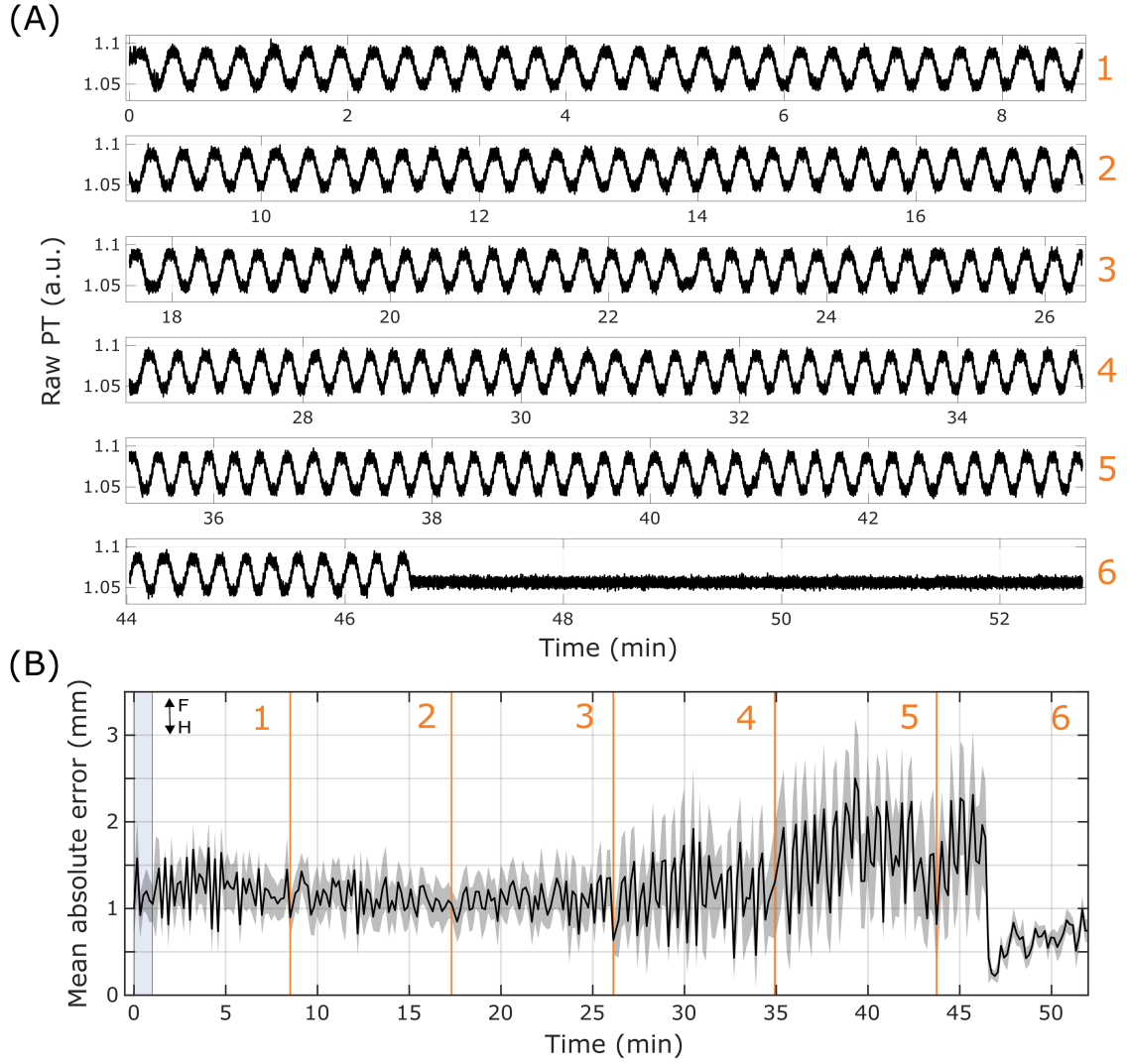
Figure 4.8: *(A) Unfiltered PT received at a single channel for a moving phantom over a total time period of 52.75 min including short pauses between the scans. 6 scans with each 513 repetitions were acquired, corresponding to a data acquisition time of 51.3 min. The phantom was not moving the last ≈6 min. (B) MAE for the PT and the registered motion in steps of 10 acquisitions. The grey shaded area represents the standard deviation.*
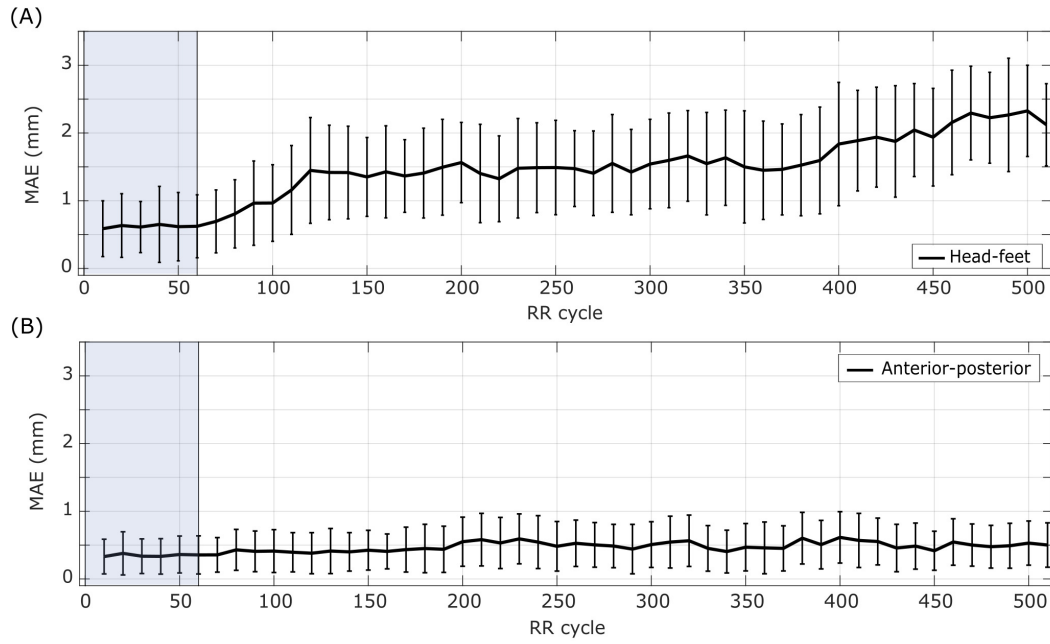
Figure 4.9: *Comparison of the registered cardiac shift with the predicted shift. The first 60 RR cycles were used to calibrate the pilot tone to the respiratory heart motion. The heart motion was then predicted and compared to the registered heart motion. The mean absolute errors averaged in steps of 10 RR cycles, and over 10 subjects are displayed for respiratory induced heart motion in HF (A) and AP (B). This figure was published in J1.*
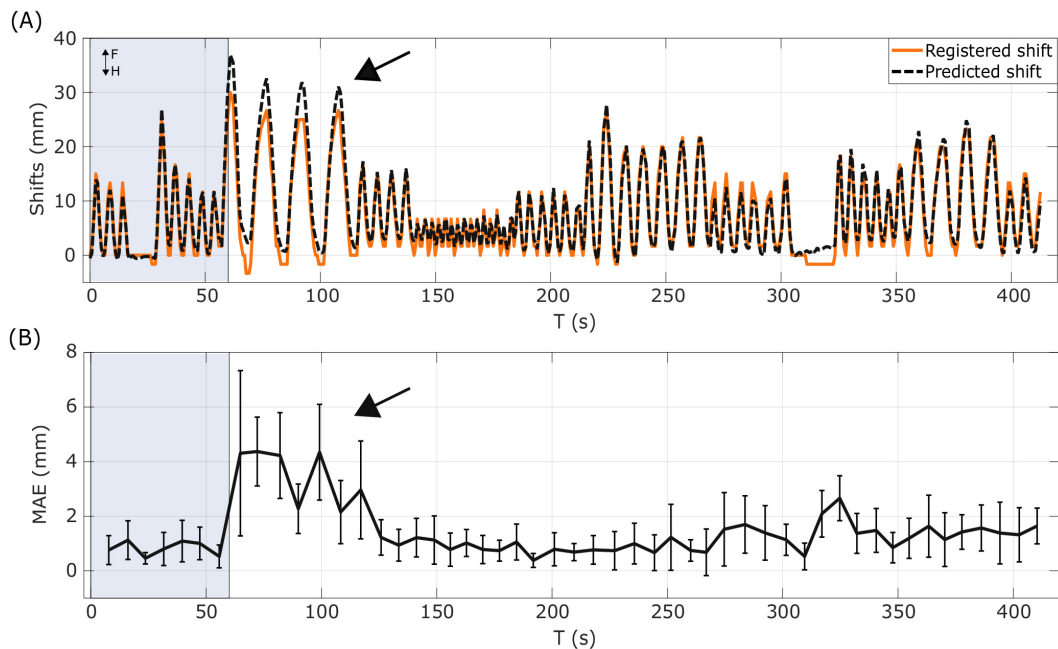
Figure 4.10: *(A) Registered cardiac shift and predicted shift of a subject with irregular breathing for 513 RR cycles. (B) Temporal stability of the motion model. The first 60 RR cycles were used to calibrate the pilot tone to the respiratory-induced heart motion. The heart motion was then predicted and compared to the registered heart motion. The mean absolute errors in steps of 10 RR cycles are displayed. This figure was published in J1.*
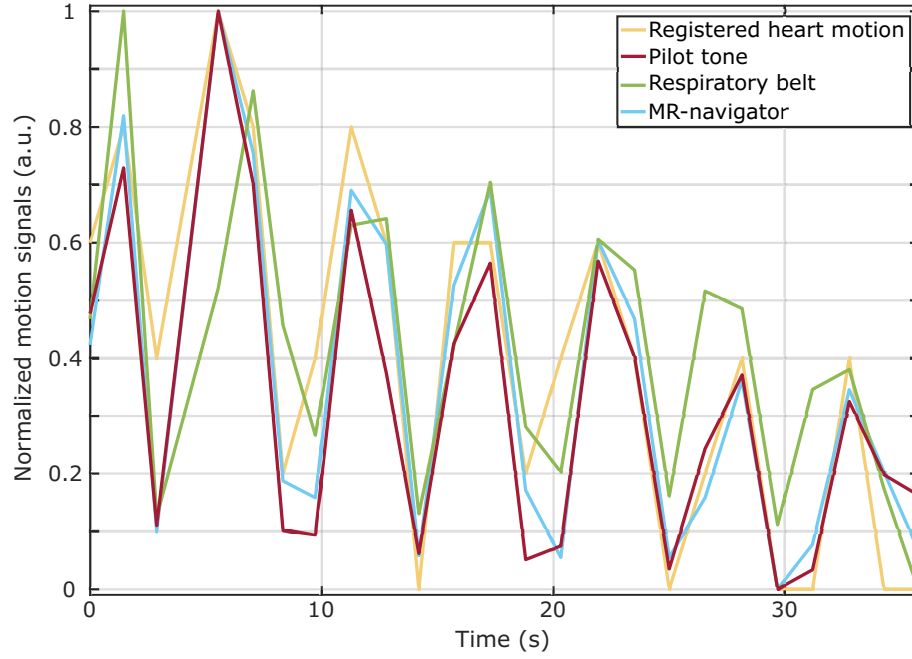
Figure 4.11: *Overlay of the surrogate signals (pilot tone, respiratory belt and MR-navigator) and the registered HF heart motion from the calibration scan. A modified version of this figure was published in C1.*

4.4.2 Comparison of three motion surrogates

Calibration scan   Figure 4.11 shows an overlay of the different surrogate signals obtained during a calibration scan compared to the estimated HF heart motion. The surrogate signals are normalized and only the data which was used for calibration is shown.

Very good agreement between all surrogate signals can be seen. The linear relationship with a factor of 0.6 between the MR-navigator signal and the registered heart motion, which was found by Wang et al. [50], could be verified. Signal curves are not smooth because only one value per dynamic image is displayed, which corresponds to the temporal resolution of the registered heart motion and MR-navigator, i.e., one value per cardiac cycle. The beginning and end of the calibration scan included breathhold phases, which were used for temporal synchronization of the respiratory belt data. In total only 26 data points were used for deriving the motion models. The regression curves are displayed in Figure 4.12 for the MR-navigator, PT, and respiratory belt with the respective correlation coefficients R^2=0.95, R^2=0.79, R^2=0.75.

Temporal stability   The MAE of the surrogate signals of the motion correction scan are displayed in Figure 4.13. The first 60 s after the breathhold phase of the respective data were used for calibration. The MAE of the following 130 s is shown in steps of 10 s for one subject for HF direction. The MR-navigator shows the best temporal stability, followed by the PT and the respiratory belt.
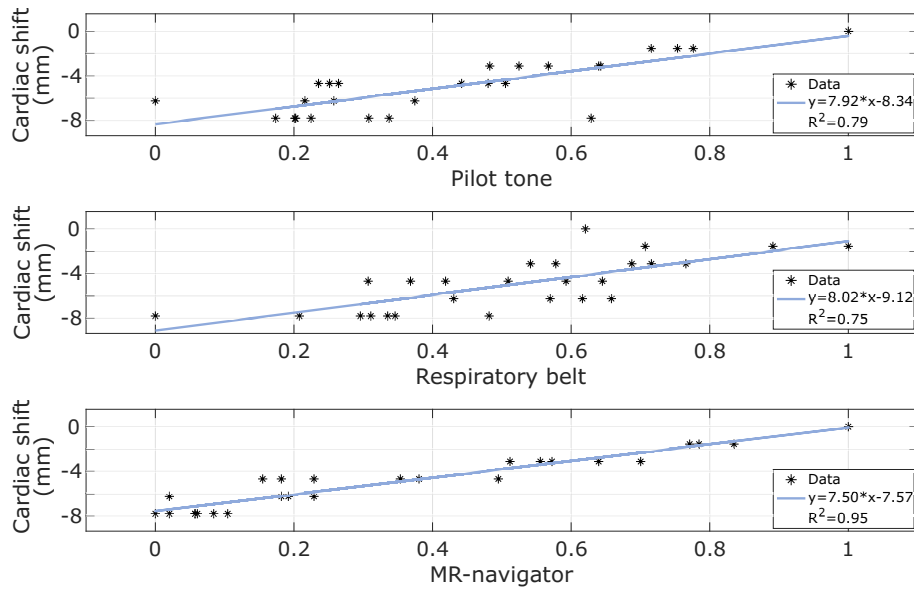
Figure 4.12: *Regression curves for the three surrogate signals and HF motion. The best correlation was found for the MR-navigator but also the pilot tone and the respiratory belt describe the estimated motion well. This figure was published in C1.*
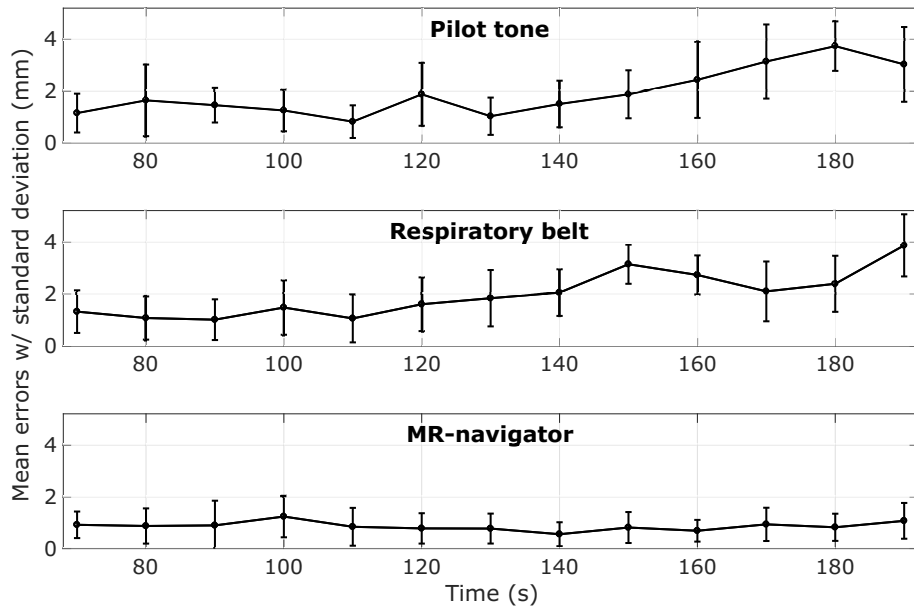
Figure 4.13: *Temporal stability of the surrogate for HF motion after calibration phase. The first 60 s after the breathhold phase (not shown) were used to calibrate the surrogate signals to the respiratory heart motion. Using the motion model, the heart motion for the next 130 s was then predicted in steps of 10 s and compared to the registered heart motion. The mean average errors and standard deviations are displayed. This figure was published in C1.*

4.5 Discussion

By analyzing the temporal stability of the PT and the motion models on 10 healthy subjects, it was found that there is a slight increase of the MAE by approximately 1.6 mm in the HF direction over a period of 513 RR cycles, corresponding to 6% of the maximum motion amplitude and in the order of image resolution. Despite this small increase, the temporal stability of this approach was still very good. Also, errors occurred for motion not captured during the calibration phase (see deep-breathing in Fig. 4.10B).

A phantom long-term scan of $\approx$53 min showed that after calibration the PT with the motion model was stable with an average MAE between the predicted and the registered phantom motion of 1.2$\pm$0.9 mm.

A comparison between three different surrogate signals was presented. For this purpose, PT-, respiratory belt- and MR-navigator data were recorded simultaneously. Linear motion models were derived from the calibration scan yielding the highest R^2 for the MR-navigator (R^2=0.95), followed by the PT (R^2=0.79) and the respiratory belt (R^2=0.75). Using the motion models, the surrogates were examined for their temporal stability. As expected, the MR-navigator showed the best temporal stability, but PT and respiratory belt also showed good temporal behavior. The MR-navigator was obtained from the same images as the registered cardiac motion and was, therefore, not susceptible to external sources of error.

In the presented temporal stability figures an increase in MAE between predicted shift and true motion over time is visible (drift). Because the drift also occurs in phantom measurements after $\approx$25 min and the motion does not change over time, a heating of the system, leading to a change in coil loads and PT intensity, could be the reason for this drift behavior. Also, each time a sequence is started, the center frequency of the scanner is readjusted automatically, so that the position of the PT might be slightly shifted and an intensity offset is introduced to the PT. This would reduce the accuracy of the motion models and result in an increased MAE. In the *in vivo* measurements, a change in the motion pattern of the subject could also be the cause of this effect. The drift behavior appears stronger for motion in HF than in AP. The underlying linear motion models assume that the relationship between the PT and the motion does not change with time. However, with long scan times, the breathing behavior of the subject can change significantly, e.g. because body relaxation occurs [140–142].

A solution to correct the drift behavior would be adaptive motion models [135]. Here, a recalibration of the motion model is performed by analyzing the recorded MR data and the surrogate throughout the MR exam. A recalibration during the data acquisition is only feasible if the acquired data allows a real-time image registration [143]. If a threshold is set beforehand, which specifies the accepted estimation errors, the adaptive correction can be implemented in an auto-adaptive way [144]. However, for continuous imaging techniques, such as cine imaging, the recalibration step must

be performed separately and a threshold cannot be preset. In this case, recalibration is always at the expense of total scan time.

4.6 Conclusion

In this chapter, the qualitative PT signal was for the first time converted into a quantitative signal by using motion models obtained from a calibration scan. Furthermore, the temporal stability of the PT was tested and compared with two other motion surrogates, the respiratory belt and the MR-navigator. In the next chapter, the three surrogates are used for retrospective motion correction. A new prospective correction approach based on the PT is also presented.

5 | Respiratory motion correction

5.1 Introduction

Parts of this chapter have been published in C1 and C2.

This chapter aims to demonstrate retrospective and prospective respiratory motion correction based on the PT.

A retrospective respiratory motion correction of free-breathing cardiac 3D data is performed with the MR-navigator, the respiratory belt and the PT.

In a next step, a new framework for prospective motion correction is developed and the implementation steps are presented. The PT is then used to demonstrate the feasibility of a prospective motion correction for 2D cardiac imaging in transverse orientation.

In an additional study on existing data of a cohort of healthy subjects, the dominant motion components during respiration are assessed. The dominant motion directions will be preferentially considered during calibration in the following chapters.

5.2 Methods

This section describes how the retrospective motion correction is performed on 3D data using a respiratory belt, an MR-navigator and the PT as motion surrogates. Further, the prospective motion correction method and the signal processing pipeline implemented for calibration and motion correction are explained.

5.2.1 Retrospective motion correction with three surrogates

Figure 5.1 gives an overview of the retrospective motion correction approach. With the calibration scan, the respiratory motion of the heart is registered and linked to the surrogate signals (PT, resp. belts, MR-navigator) via motion models. Simultaneously with the MR scan, the surrogate signals are acquired and subsequently used together with the respective motion models to retrospectively estimate translational motion.

Motion correction was performed offline with MATLAB before image reconstruction for every readout by applying a phase shift φ to the k-space data K_{uncorr}, that corresponds to the heart shift $\Delta(x, y, z)(t)$. The motion-corrected k-space K_{corr} can be calculated using equations 15 and 16. $N_{x,y,z}$ is the total number of phase encoding points along the k-space dimensions k_x, k_y and k_z. For every readout, a phase shift can then be calculated independently for the k-pace dimensions k_x, k_y and k_z using:
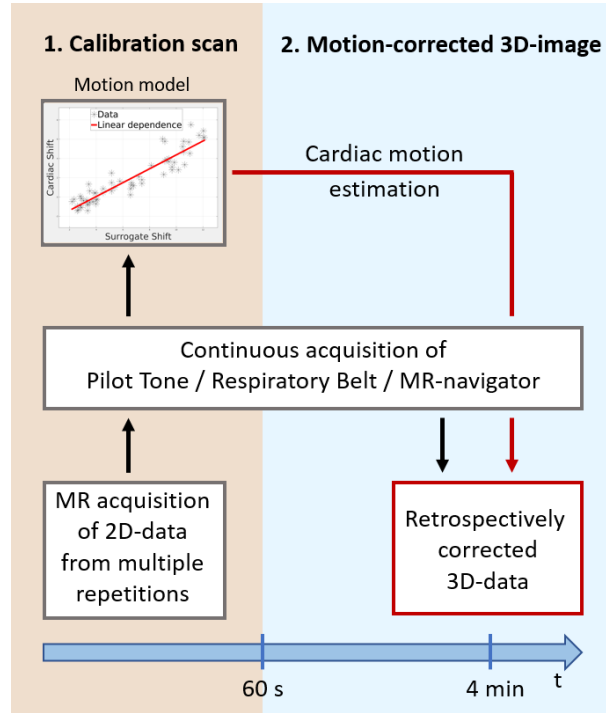
Figure 5.1: *Overview of the PT-based retrospective motion correction approach. First, 2D respiratory motion-resolved MR images and the surrogate data are obtained for about 60 s to calibrate the surrogate signals to the respiratory motion of the heart and derive a motion model. The data of subsequent 3D scans can then be motion corrected using the motion model and the respective surrogate data. This figure was published in C1.*

$$\varphi(k_j(t)) = k_j(t) \cdot \frac{2\pi}{N_j} \cdot \Delta j(t) \tag{15}$$

with $j = x, y, z$.

The corrected k-space is then calculated with:

$$K_{corr}(k_j, t) = K_{uncorr}(k_j(t)) \cdot e^{i\varphi(k_j(t))}. \tag{16}$$

5.2.2 Prospective motion correction with PT

Figure 5.2 shows the prospective motion correction framework. During a calibration scan, the PT is calibrated with the motion in the HF direction. In the next scan, the PT signal is used to predict and apply the cardiac motion online by adjusting the slice position.

For the transverse slice orientation, only through-plane motion along HF (HF_{pred}) is predicted in this chapter. The RF pulse frequency is adapted by redefining the slice position vector in the running sequence to $\left(0, 0, \Delta HF_{pred}\right)$ for every readout. This
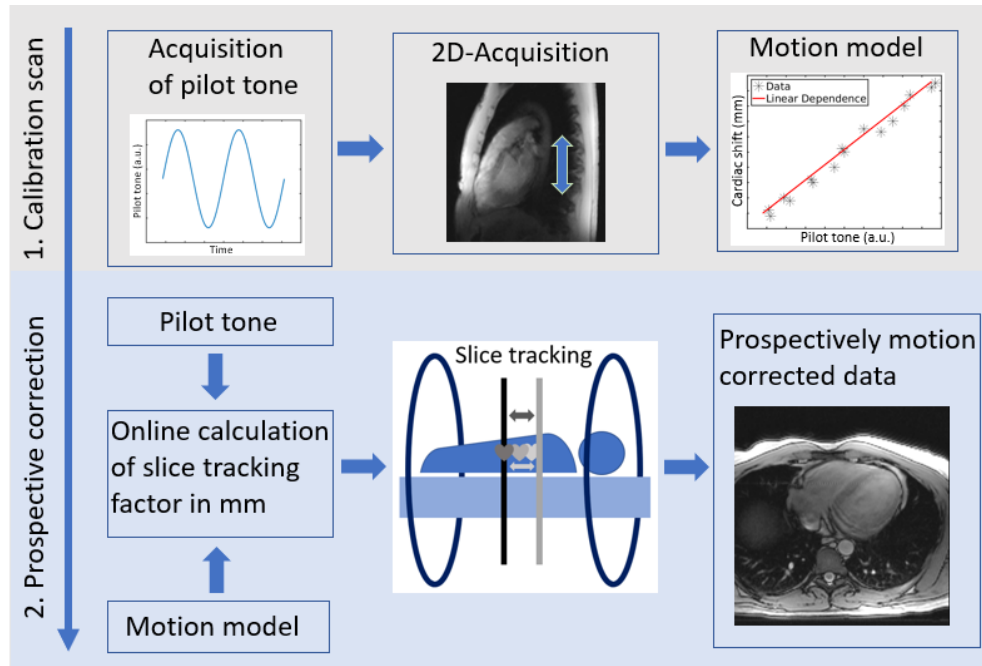
Figure 5.2: *Overview of the prospective motion correction method. First, simultaneous acquisition of MR data and PT data is carried out for about 1 min to calibrate the PT signal to the respiratory motion of the heart and derive a motion model. The data of subsequent 2D scans can then be motion corrected prospectively during acquisition using the motion model and the PT data and adapting the location of the excited slice. A modified version of this figure was published in C2.*

ensures that the excited layer follows the motion of the heart (i.e., slice tracking).

5.2.3 Online Signal Processing

The online signal processing is applied only for the prospective correction. Model formation and signal extraction are implemented in the scanner software (syngo.MR B17) written in C++ by adapting the data processing chain, as illustrated in Figure 5.3.

There are two main processing pipelines. The first pipeline performs the calibration steps. Here, the PT signal is extracted from the acquired raw data, the respiratory motion is estimated from motion-resolved images, and the motion models are build.

The second processing pipeline is the motion-correction pipeline, where corrections are applied during the scan. For this purpose, real-time processing must be implemented. This means that the PT is extracted for each readout and converted to a shift value via the motion model. The shift is then applied during the running sequence. The individual steps are now described in more detail.
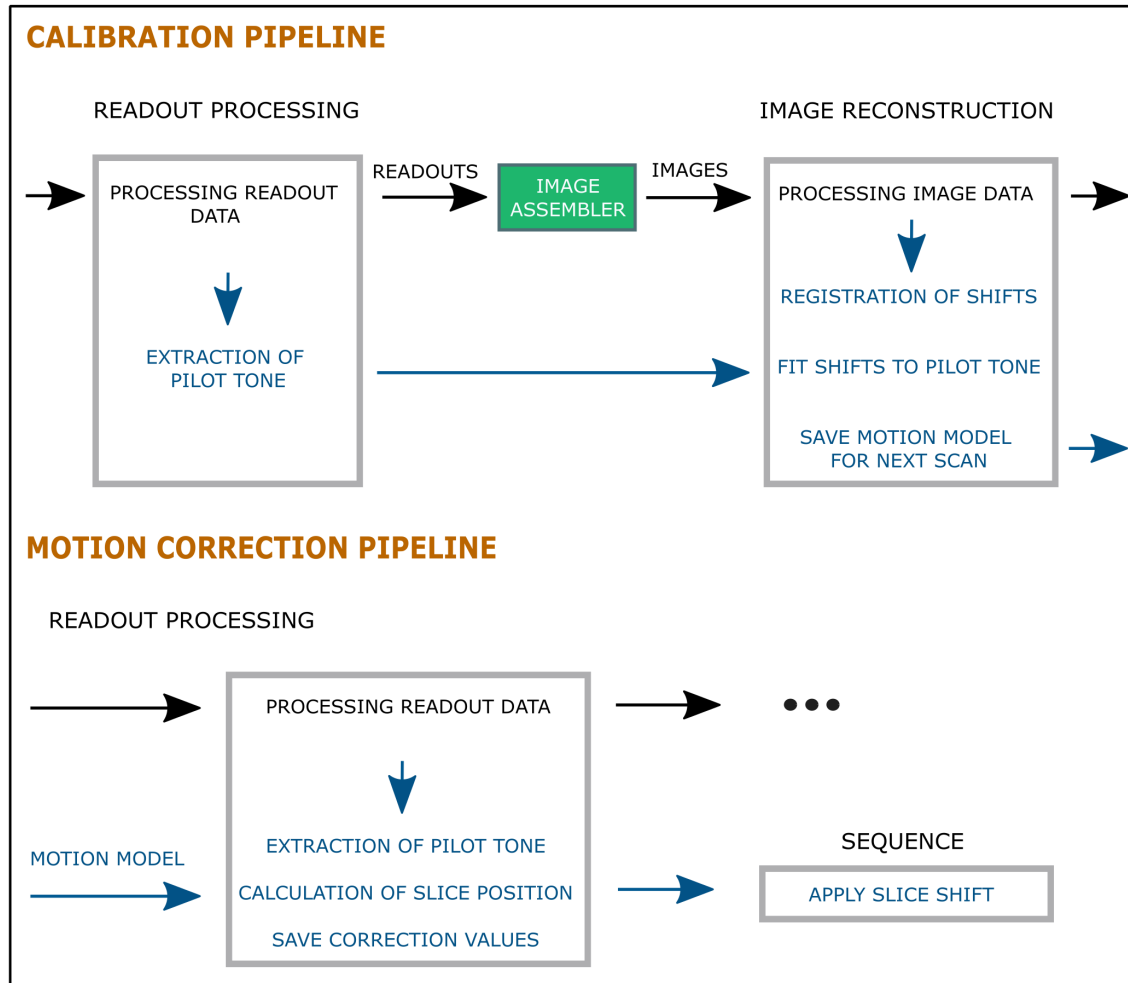
Figure 5.3: *Scheme of the reconstruction pipeline for the prospective motion correction. The PT is extracted readout-by-readout from the acquired data. Together with the image data, a linear motion model is derived online. The model parameters are used for the following scans. The calculated shift is then sent to the sequence, and the slice position is adapted during the scan.*

Calibration pipeline   To derive motion models, all data of the calibration scan covering the respiratory cycles must be assembled. As a first step, the readout position corresponding to the PT frequency is detected by finding the highest absolute signal value in the oversampling region in all acquired data. The readout position is saved for later scans, where the PT will be extracted only at that position. The reference signal is subtracted from the data, which was earlier described in section 3.2.4.

The ROI for the correlation is defined manually by selecting a rectangular region around the heart utilizing the shimming box before the start of the sequence. Taking all reconstructed images into account, the translational motion of the ROI is registered using a normalized 2D cross-correlation function, with the first image as a reference. The PT received with each coil is fitted with a linear model to the estimated heart shifts, and the corresponding R^2 is calculated.

Figure 5.4A shows an exemplary cardiac shift in HF direction obtained from

(A) Obtained respiratory induced heart motion in HF direction
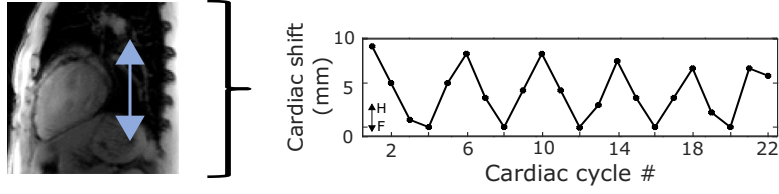
(B) Extracted pilot tone from 3 coils (out of 32)
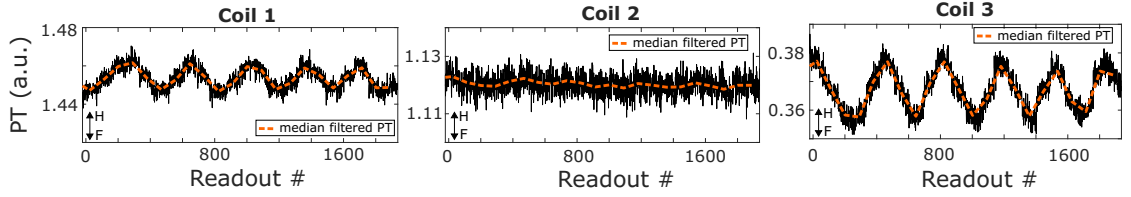
(C) Derived motion models from 3 coils (out of 32) for HF direction
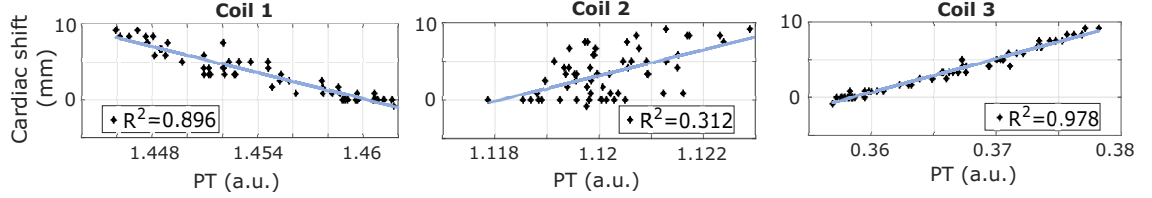
Figure 5.4: *(A) Obtained respiratory induced cardiac shift in HF direction of a calibration scan. (B) PT signal acquired during a calibration scan for 3 out of 32 coils. For illustration purposes, only a fraction of the complete signal is shown. (C) Derived motion models for 3 out of 32 coils for HF motion. The coil leading to the highest linear regression coefficient is used for the following slice tracking measurements. In this example, coil 3. This figure was published in J1.*

sagittal images of a calibration scan. The PT and the resulting motion models are shown in Figure 5.4B and C for different coils.

The motion model parameters determined for the coil with the highest R^2 in HF direction are stored in a text file. The model parameters, the coil number, as well as the slice orientation are stored for the following scans on the host computer of the scanner.

Motion-correction pipeline At the beginning of the motion-corrected scan, prior to the data acquisition, the model parameters are loaded. During the running sequence, the heart shift is predicted for every readout from the extracted PT and the motion model. Through-plane motion correction is then applied prospectively during the measurement by adapting the frequency of the RF pulse. This ensures that the slice position follows the respiratory motion of the heart for each TR.

Slice tracking with the PT must be performed along the orthogonal of the imaging plane. Otherwise the frequency position of the PT in k-space would change and the PT could no longer be extracted. The PT signal is subtracted readout-by-readout

from the k-space data, before passing the data on for further processing.

The rigid motion correction is designed for the selected ROI. Tissue that lies outside the ROI and moves differently is not corrected or wrongly corrected with this approach.

5.3   Experiments

The following experiments were performed at 3T (MAGNETOM Verio, Siemens Healthcare, Germany). The retrospective motion correction was performed on 3 subjects (2 female, 1 male, age 30±2 years) and the prospective motion correction was tested on four subjects (2 female, age 45±19 years). The local ethics board approved the *in vivo* experiments and written informed consent was given by all subjects. Data analysis and image visualization were carried out using MATLAB 2017a (The MathWorks, Natick, MA).

Calibration scan for retrospective motion correction   The calibration scan parameter for the 3D motion correction were previously presented in section 4.3.1. Respiratory belt data, MR-navigator data and the PT were acquired simultaneously with the MR data. For the calibration, two image orientations (sagittal and coronal) were acquired per cardiac cycle.

Calibration scan for prospective correction   In this chapter, the prospective motion correction scan with the PT is performed in transverse orientation. Therefore, it is sufficient that only the translational HF motion of the heart is captured with the calibration scan. The calibration scan for the prospective correction consisted of 60 cardiac, ECG-triggered, sagittal, dynamic images. An inhouse-modified bSSFP sequence was used with TE=1.5 ms, TR=3.2 ms, FOV=300x300 mm^2, FA = 30° and voxel size=1.6x1.6x5 mm^3.

5.3.1   Motion correction

The sequence parameter of the retrospective and prospective motion correction scans, which are performed after the calibration scans, are shown in Table 2.

Retrospective motion correction   The 3D data was obtained during free-breathing simultaneously with the motion surrogates. The shifts in HF, AP and RL were retrospectively determined using the three surrogates. Image registration was carried out and the shifts were applied to the data based on equations 15 and 16 for retrospective motion corrections in k-space. The results can be compared well, since the surrogates were recorded simultaneously.

Motion correction scan	Retrospective	Prospective
Measurements	1	20
Surrogates	PT, Resp. belts, MR-nav	PT
Triggering	ECG-triggered	ECG-triggered*
Sequence	inhouse-modified FLASH	inhouse-modified bSSFP
Orientation	3D	2D transverse
TE/TR	4.1/7.3 ms	1.5/3.2 ms
Flip angle	20°	30°
FOV	300×244×32 mm^3	300×300 mm^2
Voxel size	1.6×1.6×2 mm^3	1.6×1.6×5 mm^3

Table 2: *Scan parameters for 3D (retrospective) and 2D (prospective) motion corrected scans. *For phantom measurements an ECG signal was simulated with 1 Hz.*

Prospective motion correction A dynamic MR acquisition consisting of 20 dynamic images with the same scan parameters as used for the calibration scan, but in transverse orientation, was carried out during free-breathing, with and without motion correction in HF direction.

5.3.2 Estimation of respiratory motion amplitudes

The amplitudes of respiratory motion in HF, AP, and RL direction during different breathing patterns were analyzed using an existing data set to determine the dominant motion directions which should be considered during calibration.

To gain knowledge about the magnitude of respiratory motion, a dataset provided by King's College, London, UK, was analyzed. These data are only used for this specific analysis, since they were recorded without navigator signals. The dataset contains cardiac data from 23 subjects. Dynamic respiratory resolved cardiac-triggered images of the heart were present, acquired with a FOV=350×350×80 mm^3 and voxel size= 2.43×2.43×4 mm^3. The sagittal orientation shows images of size 35×35 cm, while the coronal orientation shows only a smaller area of 8×35 cm, see Figure 5.5. The blue line displayed in the figure serves as a guide to visualize the different motion states. The MR scans were carried out for 120 s and different breathing patterns, as in [135]. During the first 40 s, the subjects were asked to breathe normally, then fast for 40 s, and then carry out deep breathing for the remaining 40 s. Three subjects only performed normal and deep breathing for a total of 80 s. The ROI for motion registration was chosen manually for each subject, covering the heart in sagittal-, and the left ventricle in coronal direction. Using the open-source registration algorithm package "NiftyReg" [145], provided by UCL, UK translation, rotation and scaling motion components (affine motion) were determined.

In order to improve the accuracy of the motion estimation, the translational motion data for the three registered motion directions HF, AP and RL was spline interpolated along the time dimension giving 10 values/RR cycle instead of 1 value/RR
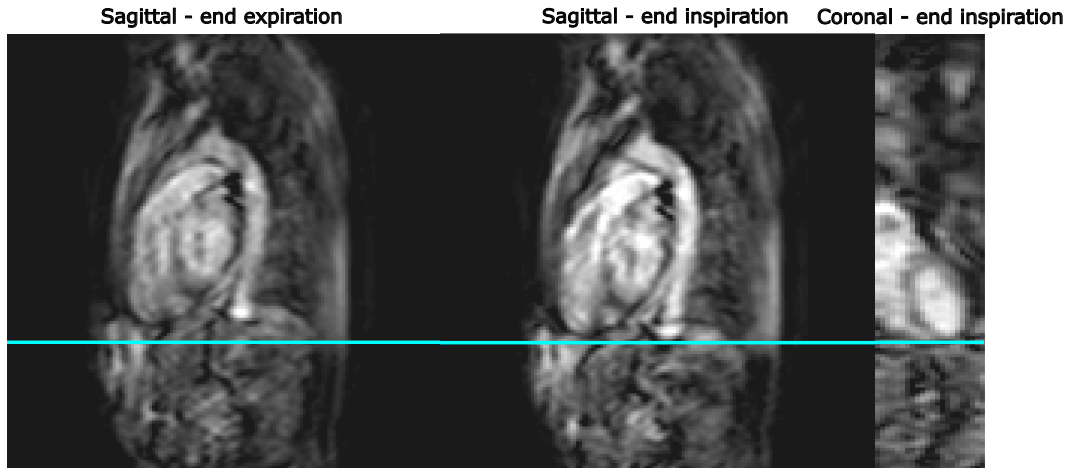
Figure 5.5: *Images from data provided by King's College London. The line serves as orientation for the breathing states.*

cycle. The maximum motion amplitude was found for each respiratory cycle using MATLAB's internal "findpeak" function. The maximum motion amplitude was then averaged for each breathing type over all subjects, yielding the mean translational motion in HF, AP, and RL. The rotations and scaling of the ROI were determined analogously.

5.4 Results

5.4.1 Retrospective motion correction

In Figure 5.6 reformatted images showing the coronary arteries for the different motion surrogates are displayed. The visualization was carried out with the tool Soap-Bubble [146]. Motion correction using the MR-navigator and PT improved visibility of the coronary arteries. The motion correction using the respiratory belt did not lead to an improvement in image quality.
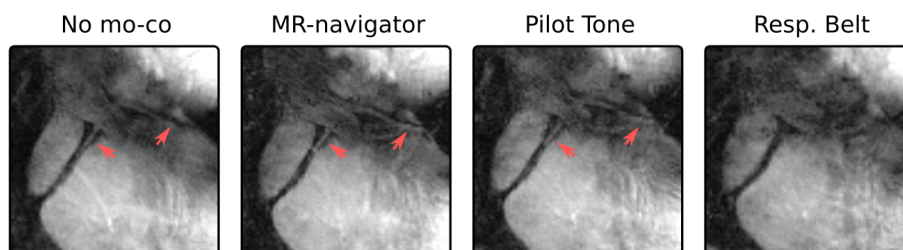
Figure 5.6: *Reformatted images for the different motion surrogates. The MR-navigator leads to the best depiction of the coronary arteries but also the PT improves the visibility of the coronary arteries. This figure was published in C1.*

5.4.2 Prospective motion correction

Figure 5.7 shows a comparison of dynamic 2D measurements without motion correction (A) and with the slice tracking method (B). Six respiratory motion states are displayed. The respective heart shifts derived from the PT signal are also shown as blue dashed lines. The PT indicates a heart position shift up to 16 mm in HF direction. The shift curves are not continuous because the PT is acquired together with the ECG-triggered MR data, and they are not smooth because a sliding window median filter was applied to the PT. Through-plane motion in the heart region can be seen in the uncorrected images (yellow arrows) and is reduced after motion correction. The red arrows point at anatomy around the vertebrae that is not in motion during respiration. Therefore, this motionless anatomy appears unchanged in the uncorrected images, while it changes with slice tracking.

5.4.3 Range of respiratory motion magnitude

Respiratory translation curves for HF, AP, and RL direction obtained with image registration for a subject are displayed in Figure 5.8. The first 40 s show normal breathing, followed by fast breathing and deep breathing phases.

The obtained results of the motion analysis for all subjects are summarized in Table 3. The dominant breathing component for all breathing types was HF translation. For normal and fast breathing patterns, mean motion amplitudes along HF and AP lay above the voxel resolution of this dataset. The translational motion was least pronounced in RL direction and lay below the voxel resolution. For deep breathing, all mean motion amplitudes exceeded the voxel resolution.

All values for normal breathing are in accordance with the literature values [28, 50, 147].

The maximum rotation of 3°, as indicated in the table for deep breathing around AP, would result in a displacement of $\approx$0.3 cm at the outermost point of the heart, when assuming a heart radius of 6 cm. Scaling by 2% would result in an enlargement of the ROI by $\approx$0.24 cm. Nevertheless, the obtained scaling and rotation values refer to the entire heart. For a 2D slice of the heart these values would be much smaller.
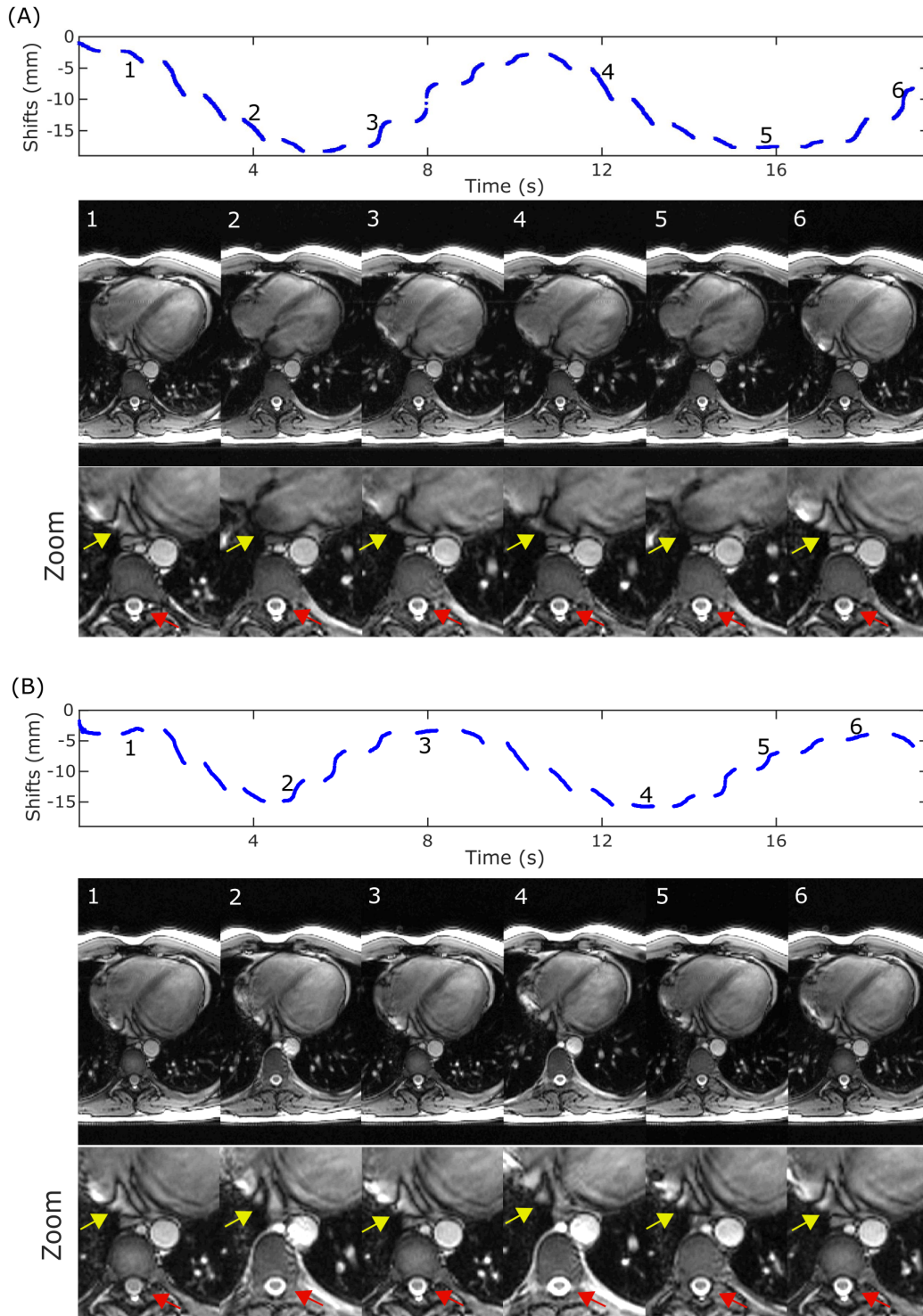
Figure 5.7: *Two-dimensional dynamic scans with 20 repetitions (A) without slice tracking and (B) with slice tracking. The heart motion (Shift) was derived from the PT signal for both scans. MR images from six different respiratory motion states are depicted. Position curves are not smooth because the PT signal was median filtered. The through-plane motion of the heart was minimized with the slice tracking method. (A) Respiratory heart motion through the image plane can be seen (yellow arrows). The applied slice shift in (B) can be seen clearly as a change of the anatomy around the vertebra (red arrows). Parts of this figure were published in C2.*
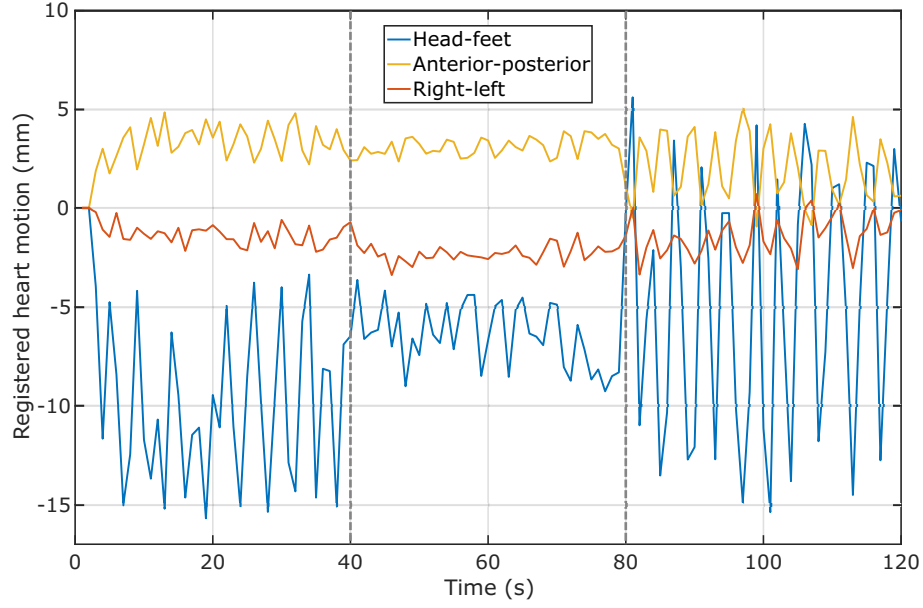
Figure 5.8: *Instructed breathing pattern of a volunteer. The first 40 s show normal breathing, followed by a 40 s fast breathing phase and a deep breathing phase.*

	Normal	Fast*	Deep
Head-feet translation (mm)	8.53±2.55	4.18±2.75	15.75±5.49
Anterior-posterior translation (mm)	2.07±0.97	1.14±0.51	5.37±4.08
Right-left translation (mm)	1.52±0.92	1.16±0.60	2.24±1.16
Head-feet rotation (°)†	1.55±0.89	1.50±0.92	2.54±1.64
Anterior-posterior rotation (°)†	1.91±1.04	1.71±0.76	2.94±1.84
Right-left rotation (°)†	1.60±1.21	1.86±0.86	2.31±1.99
Head-feet scaling factor	0.98±0.02	0.99±0.03	1.00±0.03
Anterior-posterior scaling factor	1.01±0.02	1.01±0.03	1.00±0.02
Right-left scaling factor	1.02±0.05	1.02±0.06	1.02±0.05

Table 3: *Translation, rotation and scaling factors of the heart motion due to respiratory motion averaged over 23 volunteers for normal, fast and deep breathing. *Values for fast breathing refer to only 20 subjects of the cohort. † angle is around the given axis (head-feet, anterior-posterior, right-left)*

5.5 Discussion

This chapter demonstrated the feasibility of using the PT as a motion surrogate for retrospective and prospective respiratory motion corrections.

The retrospective 3D motion correction using the MR-navigator and PT improved visibility of the coronary arteries. Unsuccessful motion correction using the respiratory belt may be due to inaccurate temporal synchronization. The identification

of breathholding phases in the respiratory belt (0.5 ms resolution) and MR data (1 image/RR cycle) could have led to inaccurate alignment between surrogate signal and MR raw data.

Prospective through-plane motion correction using the PT reduced respiratory motion artifacts in the dynamic 2D images with transverse orientation. So far, only the dominant HF motion information was utilized to demonstrate the feasibility of this new approach. Further improvement in image quality can be expected by utilizing also the AP motion information, which will be discussed in the next chapter.

Analysis of affine respiratory motion in a cohort of 23 subjects showed that the most prominent direction of translational motion during normal breathing was HF with 8.53±2.55 mm, followed by AP with 2.07±0.97 mm and RL with 1.52±0.92 mm. RL motion remains on average below one voxel size for normal breathing, while HF and AP motions exceed the voxel size.

Affine motion models are advantageous to linear motion models, due to the higher accuracy for motion mapping [56]. However, using the existing data set of 23 subjects, it was shown that rotation and scaling values are very small, thus approximating the respiratory motion by only taking translational motion into account is a suitable approach.

For retrospective corrections, the calibration scan consisted of sagittal and coronal images, which allowed to estimate all three motion directions. The motion correction was then applied to the data retrospectively without time constraints. But for prospective motion correction, the time between calibration and subsequent scan should be kept as short as possible to minimize errors that could be introduced by an unsuited motion model and also in favour of the overall scanning time. The time needed for model formation depends on the amount of data to be processed. Contributing factors are the number of images, coils and voxels. Therefore, for prospective motion correction, the number of images in the calibration scan can be reduced by only acquiring images of one orientation. Based on the data presented in Table 3, the sagittal orientation is most convenient because it captures the prominent motion directions HF and AP. Consequently, in the following chapters only images from sagittal orientation will be used for calibration. For the set parameters with 60 images acquired for calibration, the model formation step takes ≈5 min.

5.6   Conclusion

The feasibility of using the MR-navigator and the PT for motion correction with high temporal resolution was demonstrated. The advantage of the PT over the MR-navigator is its versatility. It can be used even for continuous sequences where MR-navigator data cannot be acquired because it would disrupt the magnetization needed for the imaging scan. In the next chapter, such a continuous scan is used. A prospective motion correction with the PT for cardiac cine scans will be performed and examined.

6 | Pilot tone–based motion correction (PT-MOCO) for prospective respiratory compensated cardiac cine MRI

6.1 Introduction

Parts of this chapter have been published in J1 and C2.

Cardiac cine MRI is a commonly used tool to assess cardiac function in clinical practice. The excellent soft-tissue contrast allows for the evaluation of cardiac function, and calculation of diagnostic parameters such as ejection fraction [86]. One major challenge for cine MRI is to minimize artefacts due to respiratory motion, which can corrupt image quality and thus diagnostic accuracy [33]. The preferred imaging strategy is to avoid respiratory motion by using a breathhold, in which often only a single 2D cine slice can be acquired [28].

As already discussed in section 2.4, for a full cardiac examination, breathholding has to be repeated multiple times to ensure the ventricle is well covered with multiple 2D slices [148]. Real-time imaging has been proposed to allow for cine imaging without breathholding but often requires dedicated sequences and advanced reconstruction schemes and limits the achievable temporal and/or spatial resolution [149, 150]. In addition, respiratory motion artifacts might still be present.

Another method to minimize image artifacts is respiratory gating based on the MR-navigator [37, 58, 76]. This technique can be used for retrospective and prospective motion correction (slice tracking) [7, 41–43]. Commonly, to avoid disturbing the magnetization in the heart region, the navigator monitors the position of the liver rather than the heart itself, but for this the acquisition of diagnostic image data has to be interrupted, which is not a problem for cardiac triggered sequences but for continuous sequences. For more details on the MR-navigator, please refer to section 2.4. Retrospective motion correction for 2D cine MRI has also been proposed [58]. Nevertheless, this approach can only correct for in-plane motion and cannot recover artifacts caused by through-plane motion also requiring additional gating.

In this chapter, a respiratory motion correction approach that uses the PT [10, 121] to perform prospective slice tracking for cine MRI and various slice orientations is presented. Due to the angulation of the slice, additional in-plane shifts are introduced, which are corrected retrospectively. This technique allows for continuous data acquisition and effective use of scan time, yielding cine images without the need for breathholding. A feasibility study of the method was conducted in a
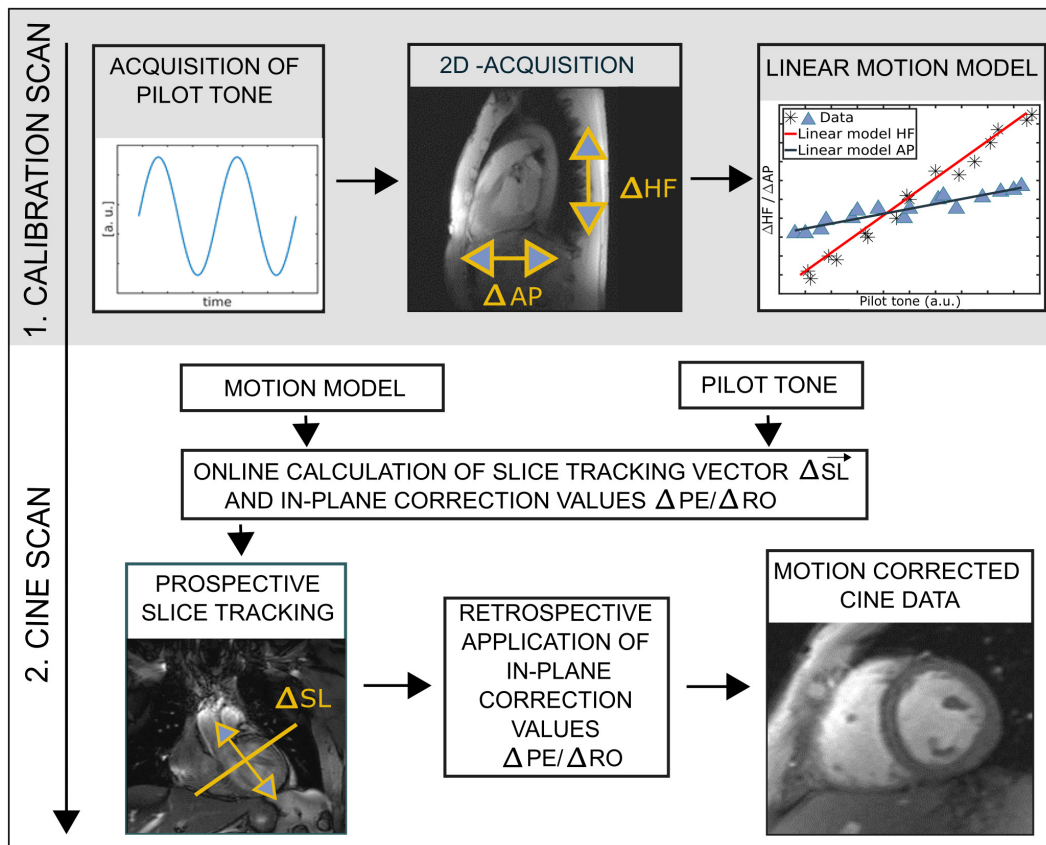
Figure 6.1: *Overview of the two-step method. First, simultaneous acquisition of MR data and PT data is carried out to calibrate the PT to the respiratory motion of the heart and derive a linear motion model. Then, the data of subsequent scans can be motion corrected prospectively during acquisition using the motion model and the PT by adapting the location of the excited slice. Additional phase shifts for in-plane motion correction, derived from the PT and the motion model, are applied retrospectively to k-space data. This figure was published in J1.*

motion phantom and 10 healthy subjects.

6.2 Methods

An overview of the method is given in Figure 6.1. In a calibration phase, 2D images of the moving heart are simultaneously acquired with the PT. A motion model linking the intensity changes of PT to the motion of the heart is derived. In the previous chapter 5, the shift in HF direction was applied to dynamic transverse images and only through-plane motion was corrected. Since diagnostic cine images show different orientations of the heart, the imaging plane must be angulated, which introduces in-plane shifts. Therefore, in this chapter through-plane and in-plane motion are corrected in the correction phase. Through-plane motion is compensated for by performing nearly real-time prospective slice tracking during the running MR cine sequence. The slice tracking also ensures that a steady-state magnetization can be achieved in the ROI. In-plane motion is corrected retrospectively by applying

the corresponding phase shifts to k-space data before image reconstruction. The approach was compared to the breathhold technique as a ground truth. For more details about the application of retrospective correction values or about the model formation, please refer to section 5.2.1 and Figure 5.4, respectively.

6.2.1 Prospective through-plane correction

First, a calibration of the PT and the heart motion is performed with the calibration scan. The second step is the motion correction during the cine scan. Using the model parameters and the PT, the respiratory motion of the heart $(\Delta HF_{pred}, \Delta AP_{pred})$ is predicted for every readout. This motion is separated into through-plane and in-plane components, as illustrated in Figure 6.2. Through-plane motion correction is then applied prospectively during measurements by adapting the frequency of the RF pulse to ensure that the excited slice follows the motion of the heart. The change in slice position $\Delta \overrightarrow{SL}$, which is applied during data acquisition, can be described as the orthogonal projection of the predicted shifts ΔHF_{pred} and ΔAP_{pred} onto the slice normal $(\overrightarrow{SN})$ of the scan orientation:

$$\Delta \overrightarrow{SL} = P_{\overrightarrow{SN}}(\overrightarrow{M}), \tag{17}$$

where $\overrightarrow{M}$ is the motion vector $\left(0, \Delta AP_{pred}, \Delta HF_{pred}\right)$.

$\Delta \overrightarrow{SL}$ is then used during the scan by adapting the RF pulse accordingly. This ensures that the excitation follows the respiratory motion of the heart for each TR.

6.2.2 Retrospective in-plane correction

In-plane motion is corrected for by adapting the phase of the acquired k-space data prior to image reconstruction, as previously described in section 5.2.1. The phase correction is applied by multiplication of the correction values

$$\Delta PE = P_{\overrightarrow{PE}}(\overrightarrow{M}) \tag{18}$$

and

$$\Delta RO = P_{\overrightarrow{RO}}(\overrightarrow{M}) \tag{19}$$

with the k-space data, where $\overrightarrow{PE}$ and $\overrightarrow{RO}$ are the slice orientation vectors of the readout and phase-encoding direction.
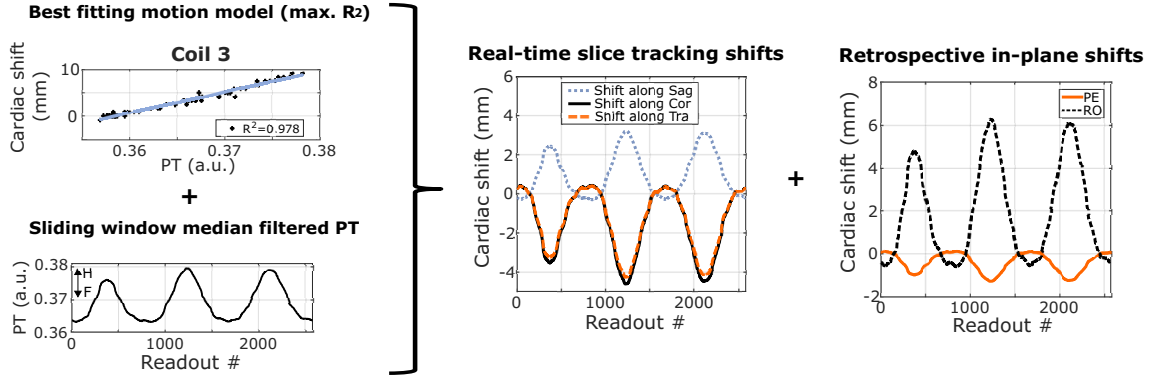
Figure 6.2: *Using the motion model and the PT, the predicted slice tracking shift is calculated, and the slice position is adapted during the sequence. In-plane shifts are applied retrospectively to the k-space data before image reconstruction. This figure was published in J1.*

6.3 Experiments

All experiments were carried out on a Siemens 3T scanner (MAGNETOM Verio, Siemens Healthcare, Erlangen, Germany). The local ethics board approved the *in vivo* experiments, which were performed on 10 subjects (6 male, 4 female, age 39±16 years, weight 71±17 kg). The parts of image reconstruction and evaluation required for the application of the prospective correction were implemented on the scanner, customizing the reconstruction chain (software syngo.MR B17). Application of correction values to k-space data and the image visualization were carried out using MATLAB 2017a (The MathWorks, Natick, MA, USA). The PT was generated as described in chapter 3.2.2 and the PT transmitting coil as shown in Figure 3.2B was used. For the phantom experiments, calibration scans (sagittal) and the dynamic scans (sagittal and transverse), i.e., scans with one image per RR cycle, were performed with the same scanning parameters as for the *in vivo* scans. Cine imaging was not tested on the phantom.

6.3.1 Calibration scan

For calibration, sagittal 2D ECG-triggered dynamic data was acquired over 60 cardiac cycles and 13.5±5.4 respiratory cycles with FOV=(320×320) mm^2, voxel size=1.7×1.7×8 mm^3, TE/TR=3.22/5.7 ms, pixel bandwidth=449 Hz/pixel and FA=12° during free-breathing using an inhouse-modified GRE sequence and two-fold parallel imaging acceleration with 24 reference lines. Each single dynamic image was acquired in an acquisition window of 507 ms in end-diastole.

6.3.2 Dynamic scan

To assess the performance of the method, dynamic measurements with the same parameters as for the calibration scan were acquired. 20 images were captured, with motion correction and without motion correction.

6.3.3 Cine scan

For the 2D cine scans, the slice orientation was changed to SAX. Depending on the subject's heart rate, 28-30 cardiac phases were captured within 15-25 s using the same FOV, voxel size, FA, and TE as for the calibration scan and a TR of 5.9 ms. During the free-breathing scans, 1-7.5 breathing cycles were completed. Data was acquired with retrospective ECG gating and two-fold parallel imaging acceleration with 24 reference lines. A full stack of 10 SAX images and additional LA, 4CHV, and transverse cine scans were acquired in one subject. For evaluating the performance of this approach, the cine scans were acquired during free-breathing, with and without slice tracking, and for reference purposes during breathhold. Cine images were reconstructed using SENSE [151] without temporal or spatial filtering of the data.

6.3.4 Analysis

To assess how well the geometry of the anatomy is preserved with the pilot tone-based motion correction (PT-MOCO), information on cardiac function was obtained from the cine images. For this analysis, the left ventricular blood pool area was measured for systole and diastole in the cine images obtained with the motion correction approach, and compared against the reference breathhold method using a Mann-Whitney-Wilcoxon test, where $p<0.05$ was considered significant. The areas of the blood pools were segmented by manual selection.

Further analyses were carried out regarding the contrast-to-noise ratio (CNR) between the myocardium and the blood pool. For comparison, images from diastole without motion correction, with PT-MOCO, and a breathhold scan were used. To determine the CNR regarding the motion artifacts, areas of the septum and the blood pool were selected manually. In addition, the sharpness of the endocardium along the septum was also determined similar to previous work for coronary arteries and abdominal imaging [152–154]. The highest sharpness value is 1, describing the edge of a Heaviside step function.

The images were reviewed and evaluated by two independent observers with more than five years experience in cardiac MRI in a randomized, blinded reading session to assess cine image quality. For this purpose, the overall image quality was evaluated on a scale of 0 to 3 for each slice. The following scale was used for blinded reading: 0 - images with poor and non-diagnostic quality due to motion-induced blurring, 1 - image quality impaired by motion which may lead to misdiagnosis, 2 - good image quality, motion artifacts hard to recognize, and 3 - excellent image quality, no motion artifacts observed [155].

6.4 Results

6.4.1 Phantom

Motion correction for dynamic images   Dynamic images of the moving phantom, with and without slice tracking, are shown in Figure 6.3 for the different scan orientations, sagittal and transverse. To visualize the motion of the structures during the entire measurement, all 20 images were summed up. Without motion correction, the image content changes during data acquisition due to the motion of the phantom, see Figure 6.3 (top row). With motion correction, the acquired slice follows the motion of the phantom, leading to the same image content during measurement. Motion correction improves the depiction of the same underlying structure compared to the uncorrected scan, leading to reduced blurring in the summed images.
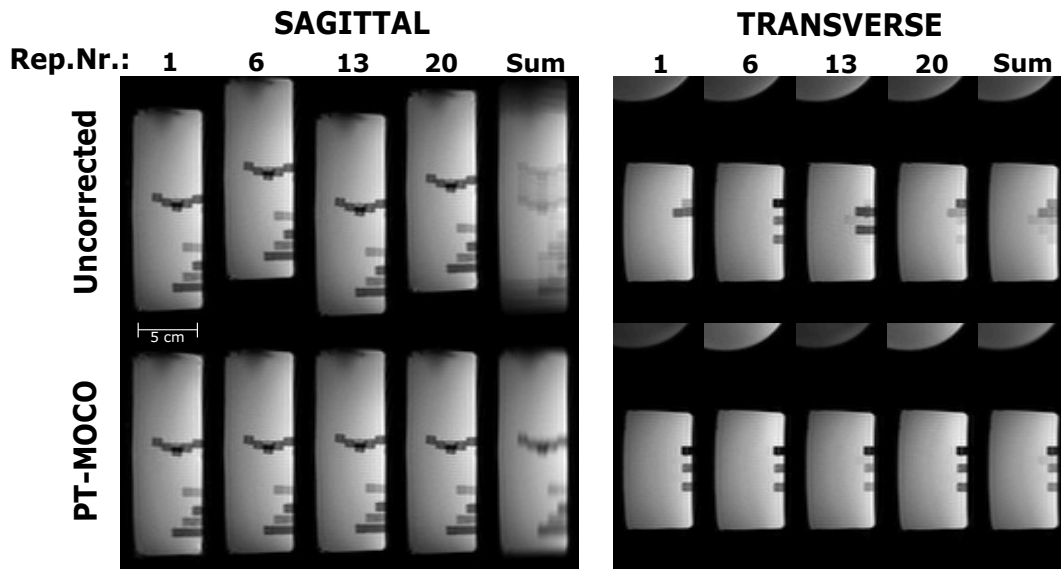

Figure 6.3: *Two-dimensional dynamic scans with 20 repetitions with and without the motion correction PT-MOCO of a moving phantom. MR images from four different motion states are depicted, as well as the sum of all 20 images for sagittal and for transverse orientation. The phantom motion was minimized with this motion correction technique. The motion direction was HF, and, therefore, in the sagittal images, the phantom moves in-plane, and for the transverse images, there is only through-plane motion. This figure was published in J1.*

6.4.2 In vivo

Motion estimation succeeded for all subjects. Figure 6.4 shows the cardiac shift as a function of the PT for all 10 volunteers distinguishing also between inspiration and expiration and head-feet (Fig. 6.4A) and anterior-posterior motion (Fig. 6.4B). The linear models fit well for the majority of volunteers with no visible hysteresis effect. For volunteers 2 and 7 there is a small difference for inspiration and expiration but the difference is between 1 and 2 mm.

(A)

(B)
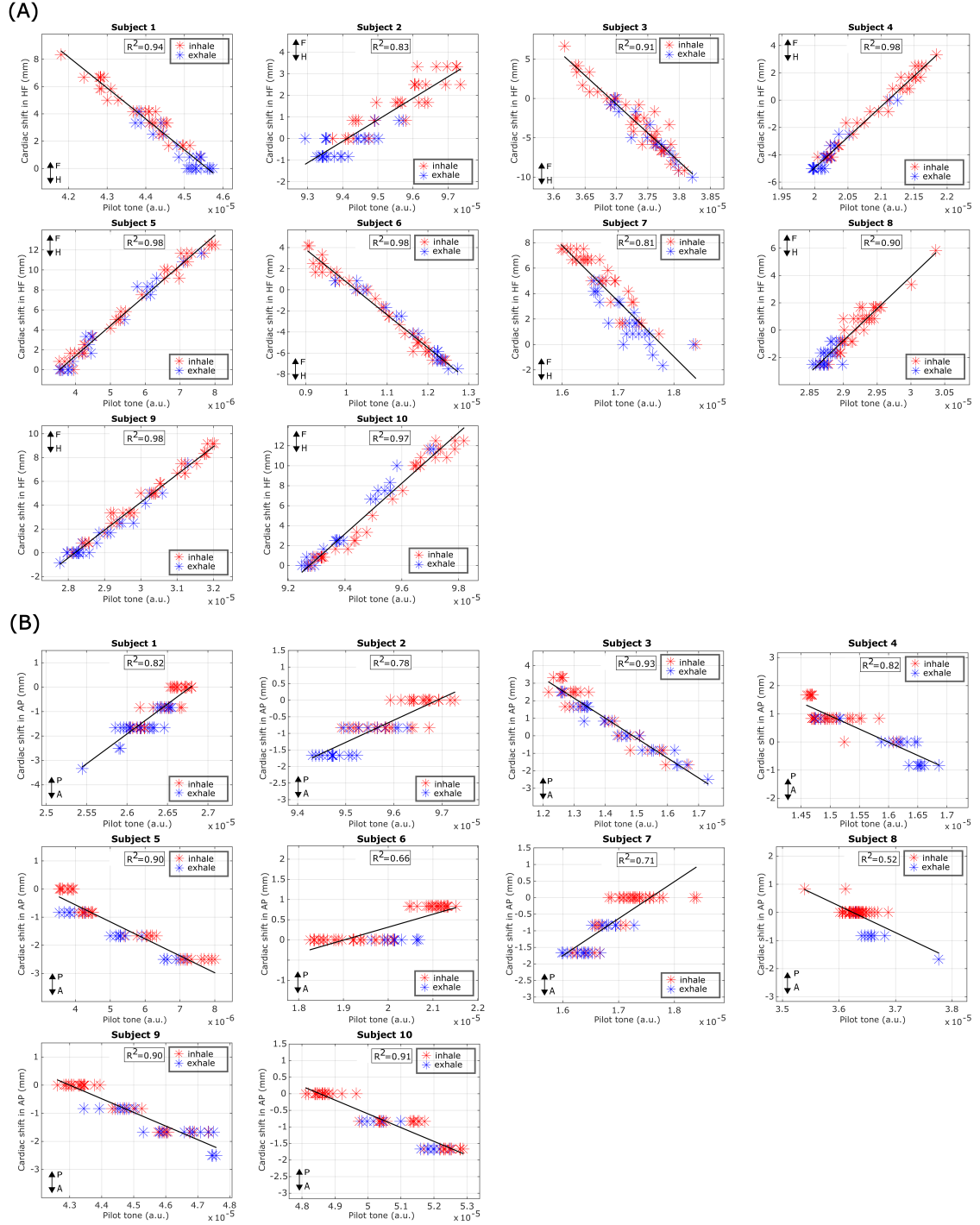
Figure 6.4: *Calibration data for 10 subjects. The data from 60 dynamic acquisitions were fitted with linear regression curves and used for the motion models. (A) motion models for head-feet direction and (B) motion models for anterior-posterior direction. Parts of this figure were published in J1.*
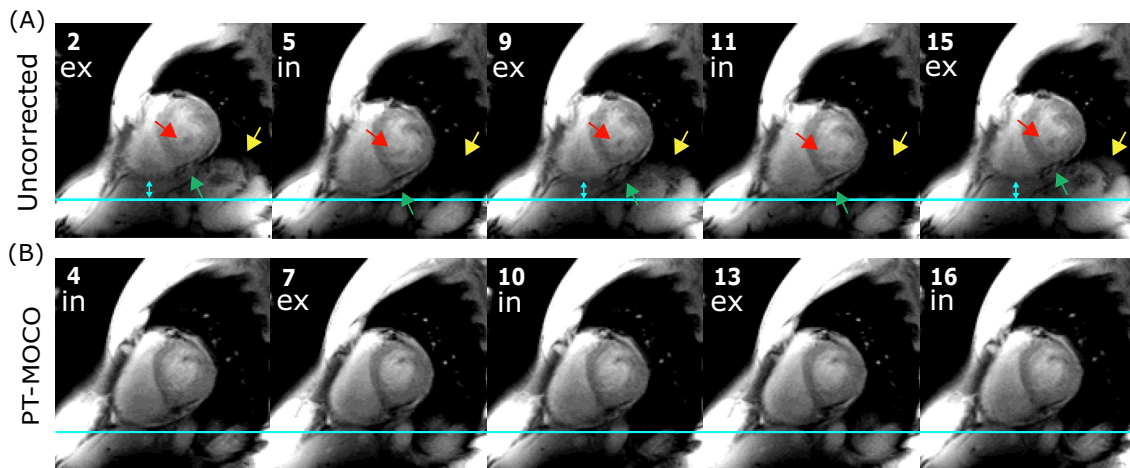
Figure 6.5: *Free-breathing, 2D dynamic scans with 20 repetitions (A) without and (B) with PT-MOCO. MR images from five different respiratory motion states are depicted with numbers indicating the repetition number. The images were chosen to alternatingly show end-inspiration (in) and end-expiration (ex). (A) Changes in the anatomy due to respiratory through-plane motion are indicated with arrows. The horizontal blue line gives a reference for in-plane motion. The motion of the heart (through-plane and in-plane) was minimized with the slice tracking method, as can be seen by comparing the regions where the arrows point at and the heart position with reference to the blue line in (A) and (B). This figure was published in J1.*

Motion correction for dynamic images   Dynamic MR images, acquired in $\approx$17 s with the ECG triggering, without motion correction, and PT-MOCO, are depicted in Figure 6.5. Images were selected from the image stream, such that the depicted motion alternates between end-inhalation and end-expiration, identified based on the PT. Anatomical features such as the papillary muscles (red arrows), the pericardium (green arrows), and the liver (yellow arrows) change during the measurement as the tissue moves through the slice. In-plane displacement of the left ventricle can also be clearly seen (blue arrows) and was up to 11 mm. PT-MOCO accurately corrects for these motion displacements.

Motion correction for cine imaging   In Figure 6.6 the scale-free PT and the motion shifts calculated with the motion model along the slice direction (Fig. 6.6B) and in-plane (Fig. 6.6C) are shown. PT-MOCO resulted in improved cine image quality for all subjects relative to the uncorrected images.

The isolated effects of the in-plane and through-plane correction on the full FOV are shown in Figure 6.7. Without motion correction, strong artifacts can be seen in the heart region. After through-plane correction was applied, motion artifacts appear stronger and more globally throughout the body and FOV. After through-plane and in-plane correction, artifacts in the heart region are minimized.

(A)

(B)

(C)
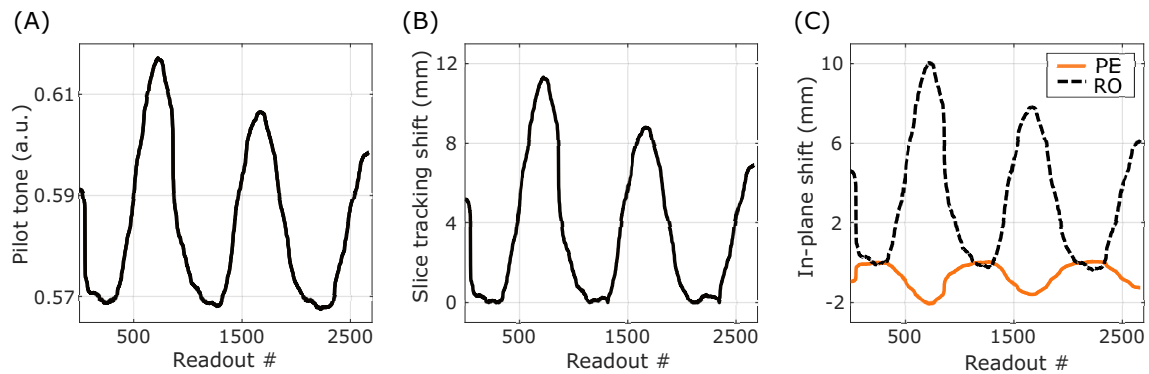
Figure 6.6: *(A) Median filtered PT acquired for each phase-encoding line (i.e., each TR). Using the motion model from the calibration, correction values for the real-time through-plane correction (B) and the retrospective in-plane correction (along readout (RO) and phase encoding (PE)) (C) can be calculated from the PT. This figure was published in J1.*
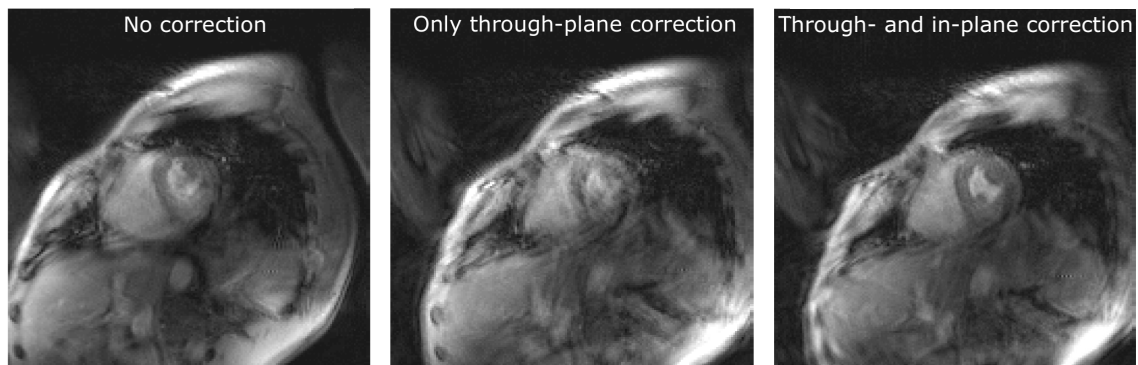
Figure 6.7: *Full FOV without motion correction, after through-plane correction and with through-plane and in-plane correction*
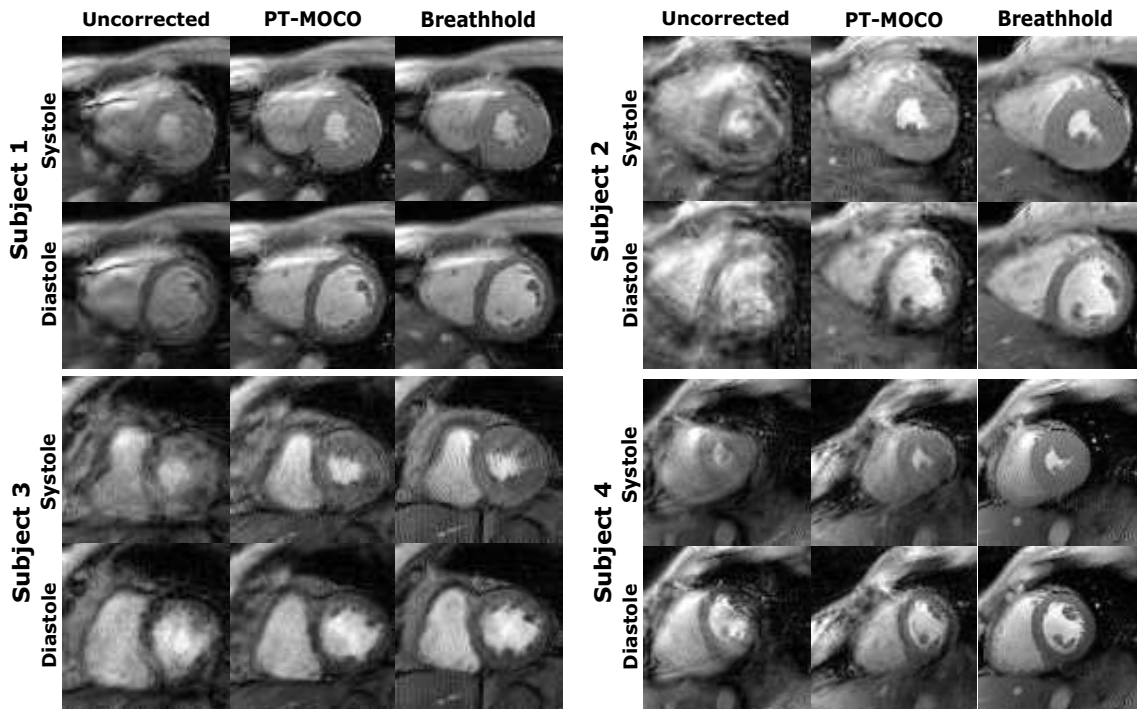
Figure 6.8: *Comparison of cine MRI acquired during free-breathing without (uncorrected) and with PT-MOCO. A standard breathhold cine scan is also shown for reference. For each subject, end-systolic and mid-diastolic phases are shown. It is important to note that each method is acquired in a separate scan, leading to small differences in the visualized anatomy. This figure was published in J1.*
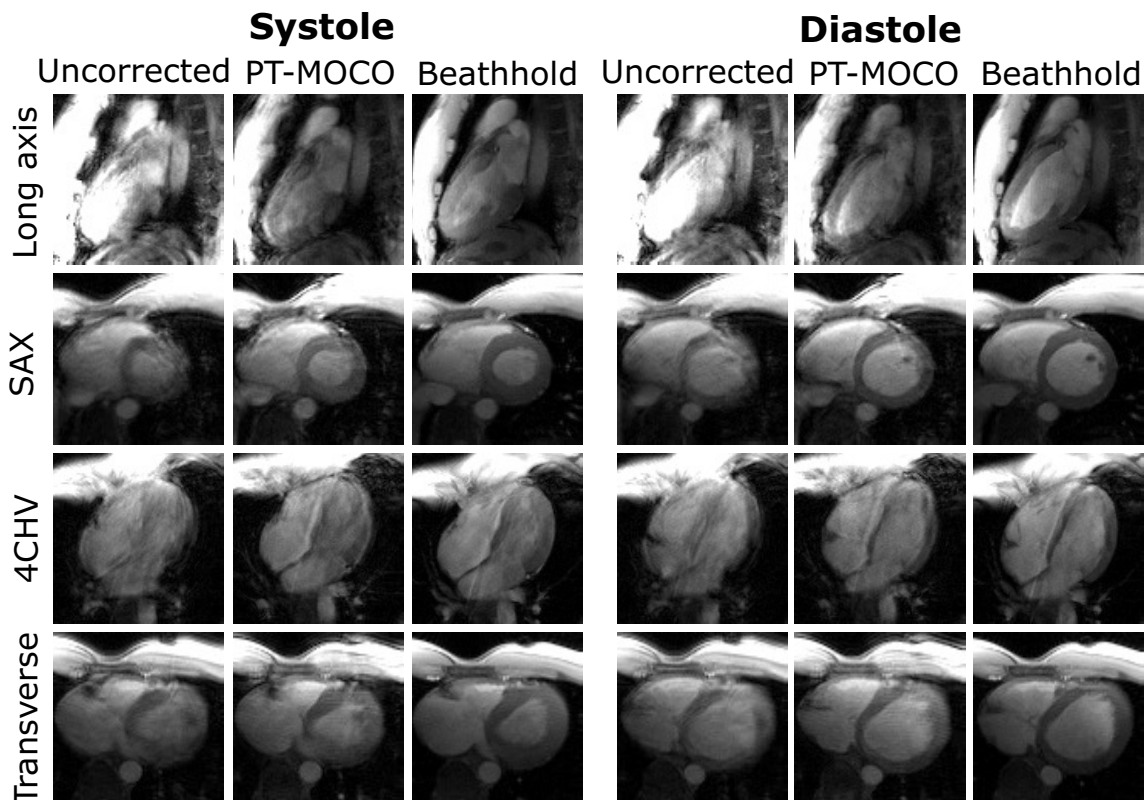
Figure 6.9: *Images of end-systole and mid-diastole for 4 different orientations in one healthy subject. For comparison, the standard breathhold cine scan is also shown. This figure was published in J1.*
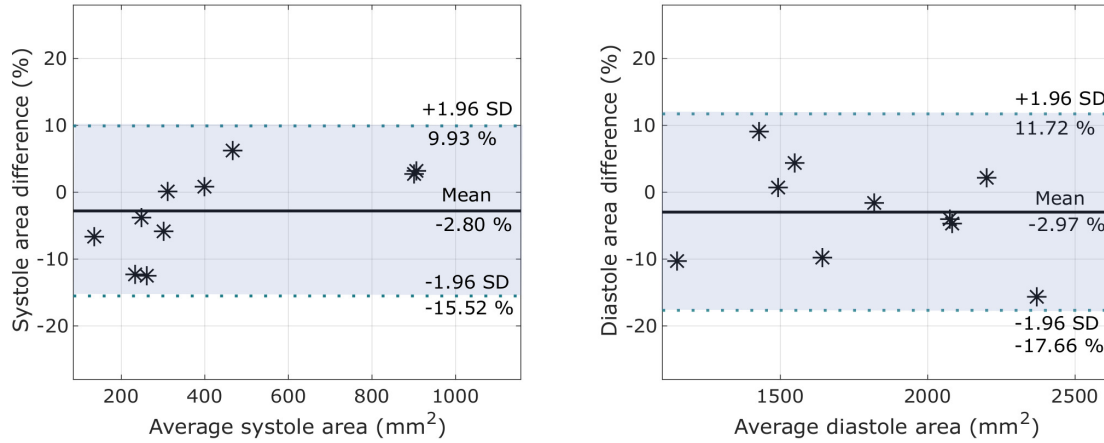
Figure 6.10: *Bland-Altman plots comparing the difference of the left ventricular blood pool area between the motion-corrected data and the breathhold data for systole and diastole. Black and dashed blue lines show mean and ±1.96 SD limits of agreement of the difference.*

Figure 6.8 shows end-systole and mid-diastole of four subjects acquired during free-breathing without correction and with correction using PT-MOCO. For comparison, data were also obtained during a single breathhold. End-systole and mid-diastole for 4 different orientations in one healthy subject are shown in Figure 6.9. Again for comparison, the standard breathhold data is also shown.

Information on cardiac function obtained from cine images with PT-MOCO was compared with the breathhold technique as a gold standard, as seen in Figure 6.10. The left ventricular blood pool areas were determined by manual selection for all volunteers for systole and diastole. The mean differences between the reference method and the approach were <3%, with standard deviations (SD) of 12.7% and 14.7% for systole and diastole, respectively. The differences between the two methods were not significant (systole: p=0.91, diastole: p=0.97).

The CNR with regards to motion artifacts for the uncorrected diastolic images was found to be 7.6±2.7, for PT-MOCO 12.8±4.0, and for the breathhold data 13.8±4.9. Significant improvements of CNR by 75±47% (p≤0.01) were found between the uncorrected data and PT-MOCO and by 88±60% (p≤0.01) between the uncorrected data and the breathhold data. The difference of PT-MOCO compared to the breathhold was not significant (p=0.9).

The sharpness of the endocardium was 0.13±0.04 for the uncorrected images, 0.16±0.03 for PT-MOCO images, and 0.19±0.03 for breathhold images. The sharpness improved significantly by 30±27% (p=0.04) between the uncorrected data and PT-MOCO. For the uncorrected data compared to breathhold data, the sharpness improved significantly by 58±45% (p≤0.01), whereas for the breathhold data compared to PT-MOCO data, differences were not significant with -16±12% (p=0.054).

The image score for the uncorrected data was 0.3±0.6, which was increased to 1.4±0.7 using PT-MOCO (p≤0.01). The difference of PT-MOCO compared to the
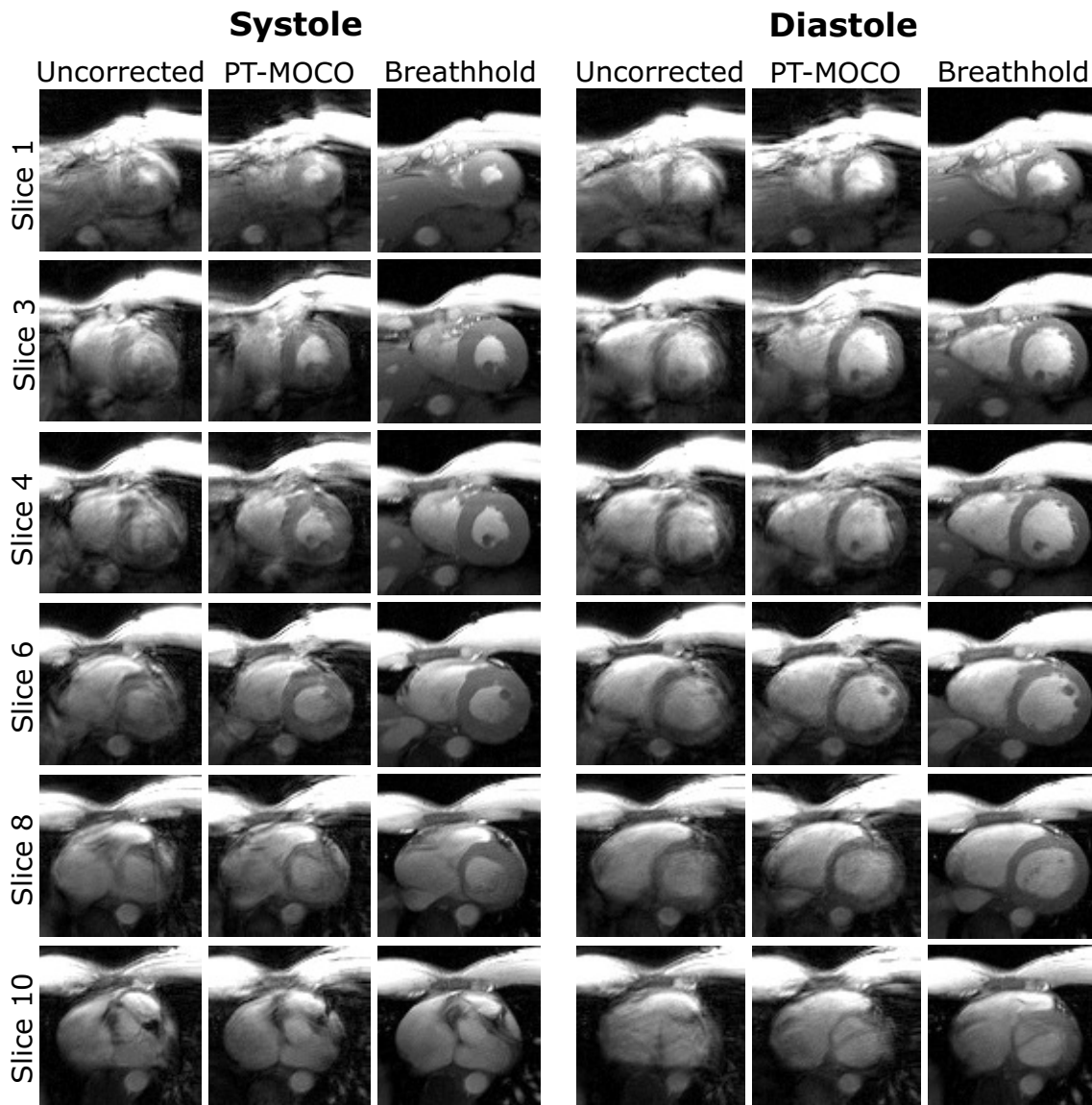
Figure 6.11: *SAX cine MRI in one healthy subject. 10 slices (6 displayed) covering the complete left ventricle were recorded. PT-MOCO leads to a reduction of respiratory motion artifacts. This figure was published in J1.*

breathhold cines, with an image score of 2.6±0.6, was also significant (p≤0.01).

6 slices (out of 10) of a SAX stack covering the left ventricle of a healthy subject are displayed in Figure 6.11. It is important to note that the three scans, uncorrected, with PT-MOCO and breathhold, were acquired as separate scans and hence can be at slightly different scan positions.

6.5 Discussion

This chapter demonstrates the feasibility of PT-based prospective motion correction for free-breathing cardiac cine MRI. The prospective motion correction approach, which was demonstrated in section 5.4.2 on 2D dynamic images, was for the first

time used here for cine imaging. In the previous section, the prospective correction approach was only shown for HF motion on images with transverse orientation. In this chapter, cine images were acquired mainly in SAX, but also in LA, 4CV and transverse orientation. The change of orientation resulted in in-plane shifts, which were corrected in a retrospective step, as described in section 6.2.2.

It was shown on a phantom and 10 healthy subjects that this approach led to accurate motion correction and respiratory motion artifacts could be reduced.

So far, during calibration, a single coil was selected based on the linear regression correlation coefficient R^2. Bulk patient motion during the scan (i.e., shifts of the entire body) could lead to a displacement of the receiver coils and amplitude changes of the PT, which result in errors in the motion prediction. The PT appeared very sensitive to a change in distance of the receiver coils and transmitter coil. Analysis of this behavior was carried out in section 3.5.3. Combining the PT signal from multiple receiver coils could improve the slice tracking approach. Another option to overcome this problem could be to integrate the PT coil into the MR receive coil array.

In this chapter, only translational motion along HF and AP direction was corrected. Although the respiratory motion of the heart is most prominent along these directions, as shown in section 5.4.3, also calibrating RL motion could further improve the image quality. This could be achieved by using a sagittal and a coronal calibration slice, one acquired in diastole and one in systole of each cardiac cycle. This two-orientation-calibration was done already in section 5.4.1 for the retrospective motion correction.

The patient-specific linear model proved to be useful for approximating the respiratory motion of the left ventricle. Figure 6.4 shows that the calibration worked well (lowest R^2 values is 0.8 for HF), and there are only small differences (i.e., hysteresis effects) between inspiration and expiration. More advanced models, such as affine motion models or taking hysteresis effects between inspiration and expiration into account, could improve the prediction of respiratory motion and image quality [46, 135, 156].

Currently, the same motion model for each slice position was used. The registration is carried out for the entire left ventricle, so the motion model fits very well for a mid-ventricular region but is less accurate for apical regions. The further the scan position deviates from the original calibration plane, the greater the errors of the correction since the motion model no longer fits there. For example, in Figure 6.9 for the LA, the motion correction in the apex works less accurately than for the mid-ventricular region, where the PT was calibrated for. Also, slices 1 and 10 in Figure 6.11 displaying the apex and the base of the ventricle, respectively, show more motion artifacts than the slices covering the mid-ventricular region. Affine motion models would allow to adapt the motion model better to the current slice position and overcome this problem.

A median filter with a width of 100 readouts was applied to the PT to reduce noise

in the signal. Therefore, the PT of the first 100 readouts may not be as accurate as of the following signal. However, this did not have any visible effect on the cine images since at most 7 readouts per cardiac phase are affected. In addition, the filter leads to a temporal smoothing of the motion signal and hence a short delay of 50 samples, corresponding to 285 ms for the cine scans, between the estimated and true motion of the heart. However, this delay is short compared to the duration of a respiratory cycle. Other filters could overcome this problem, such as Kalman filters [134], which have already been used with the PT for prospective cardiac triggering [125].

Applying the individual motion correction steps showed that after only applying the through-plane correction, motion artifacts were more pronounced than without correction, see Figure 6.7. That is because through-plane correction is performed along the slice normal and not along the direction of motion, which inevitably leads to additional in-plane shifts. Combining both through-plane (slice-tracking) and in-plane correction successfully minimized motion artefacts.

The motion model was optimized for the left ventricle but is applied globally to the entire slice. The retrospective correction reduces motion artifacts for the ROI, but the surrounding static tissue (e.g., back and spine) or tissue moving differently to the heart (e.g., liver), is wrongly corrected, leading to residual artifacts for segmented k-space acquisitions.

A correction with the PT could work even better for trajectories that sample the k-space center multiple times (i.e., radial sequences) because these sequences are more robust against motion artifacts, and, therefore, wrongly corrected tissues would produce fewer artifacts.

For the comparison between the breathhold method and PT-MOCO, the left ventricular blood pool areas were determined, instead of the EF, because only one slice in SAX was acquired. The breathhold scan was always performed in end-expiratory state. In contrast, the respiratory state used for slice tracking was arbitrary, and the motion-corrected image may show a different SAX position and lead to errors in the quantitative comparison.

Based on the PT and the dynamic images used for calibration, end-expiration could be identified and used as a reference for the motion model to ensure slice tracking is carried out to a more well-defined motion state.

The PT is independent of k-space sampling and thus could also be combined with other sampling trajectories. Motion information is available with a high temporal resolution, taking also variations in the breathing cycles into account. In addition, in this prospective implementation, motion corruption is prevented during data acquisition and, therefore, no additional reconstruction time for a retrospective motion correction [57, 157] is needed. This makes this approach easy to integrate into clinical practice.

CNR and sharpness of the endocardium show a significant improvement using PT-MOCO compared to the uncorrected cine scan but are still not as good as breathhold

acquisitions.

For healthy subjects, a breathhold acquisition will provide the best image quality. Still, for patients having difficulties holding their breath, the PT-MOCO approach can improve the image quality significantly compared to an uncorrected free-breathing acquisition. Nevertheless, studies on patients are still required to assess the applicability of this approach in clinical routine. So far, this method was used for cine imaging, but other continuous acquisitions, like MRF [158] or T_1 mapping [159] could also benefit from the method.

In the next chapter, the motion correction approach is tested for T_1 mapping.

6.6 Conclusion

The PT provides a suitable motion signal for prospective respiratory motion correction. PT-MOCO showed a significant improvement in image quality compared to an uncorrected free-breathing acquisition for all subjects. Further studies are required to assess this method for clinical application. The next chapter evaluates whether the prospective motion correction method with the PT is feasible for cardiac T1 mapping.

7 | Pilot tone–based prospective correction of respiratory motion for free-breathing myocardial T1 mapping and cine imaging

7.1 Introduction

Parts of this chapter have been published in J2 and C3.

T_1 mapping is a non-invasive tool to diagnose and investigate various pathological changes in the myocardium, [114, 160, 161]. Ischemic and nonischemic cardiomyopathies [162, 163] like fibrosis [164, 165], amyloidosis [166] and iron overload [167] can be detected with native T_1 mapping, i.e., without administration of a contrast agent. Furthermore, with a contrast agent, the myocardial extracellular volume (ECV) can be calculated by measuring native and postcontrast T_1 [168] allowing, for instance, better diagnosis of myocarditis [164, 169].

Common techniques for myocardial T_1 mapping include modified Look-Locker Inversion recovery (MOLLI) and SAturation-recovery single-SHot Acquisition (SASHA) [114, 170, 171]. For these techniques, after an inversion or saturation pulse multiple images are acquired in a predefined cardiac phase but at different inversion or saturation times. A model is then fitted to these images to calculate the T_1 for each voxel. Despite the fact that these images provide accurate T_1 maps, data acquisition is not very efficient, because only a small part of the cardiac cycle is utilized to obtain diagnostic information. In addition, the cardiac phase in which the T_1 map should be acquired, has to be defined prior to the scan and cannot retrospectively be optimized. This is particularly challenging for patients suffering from irregular heartbeats. Recently, a continuous radial acquisition has been proposed, which allows for the reconstruction of T_1 maps in different cardiac phases from the same scan [159]. Cine images can also be reconstructed from the same data, allowing to retrospectively optimize the selection of the cardiac phase.

Nevertheless, respiratory motion is still a major cause of artifacts in the estimation of T_1. If the whole heart is to be covered, several breathholds are necessary since only one slice is acquired per breathhold. Although patients are asked to hold their breath, previous studies on T_1 mapping have shown that respiratory motion of the heart was still present in more than 40% of patients due to limited breathholding capability [5, 172]. This leads to misalignment between the qualitative images

acquired at different inversion times and errors in the voxel-wise T_1 estimation.

Retrospective motion correction approaches have been proposed to compensate for this by realigning the obtained qualitative images but they can only correct for in-plane motion and not through-plane motion [5, 173, 174]. To ensure both in-plane and through-plane motion correction of 2D imaging, slice tracking approaches are required, which update the slice position in real-time during data acquisition. Slice tracking using an MR-navigator has also been proposed for motion correction of free-breathing T_1 mapping [8, 42, 175]. Nevertheless, this approach is not applicable to a continuous MR scan because respiratory navigators would interrupt the data acquisition.

This chapter presents the use of a PT-based motion correction for free-breathing myocardial T_1 mapping and simultaneous cine imaging. During the measurements, the slice position is adapted in nearly real-time, and the motion of the heart during breathing is tracked. This ensures that data at different inversion times are acquired at the same position in the heart during the entire respiratory cycle. In addition to this prospective through-plane motion correction, in-plane motion correction is also carried out during image reconstruction based on the quantitative PT signal. This technique is used for high-resolution T_1 maps without the need for breathholding. A feasibility study of the method is conducted in a motion phantom and 11 healthy subjects.

7.2   Methods

An overview of the method is given in Figure 7.1. A continuous radial acquisition with multiple inversion pulses at predefined time points is used to obtain T_1 maps and cine data [176]. For the motion correction approach, the PT is first calibrated to the motion of the heart via a calibration scan that consists of sagittal ECG-triggered images, one image acquired per cardiac cycle over several breathing cycles. Two motion models for HF and AP direction are derived from the calibration. With the calibrated PT signal, the respiratory motion in HF and AP direction is then estimated for every readout during the subsequent scans. Through-plane motion correction is applied during measurements by changing the frequency of the RF pulse, thus enabling prospective slice tracking. In-plane motion is corrected retrospectively based on the PT and the motion models. Additionally, non-rigid image registration is used retrospectively to estimate and correct any residual motion not captured by the PT.

7.2.1   Calibration scan

For the calibration scan, the PT and 45 sagittal 2D images of the heart are acquired simultaneously in $\approx$45 s, such that the whole breathing cycle is displayed a few times. A ROI covering the heart is chosen prior to the scan. For this, the manually defined
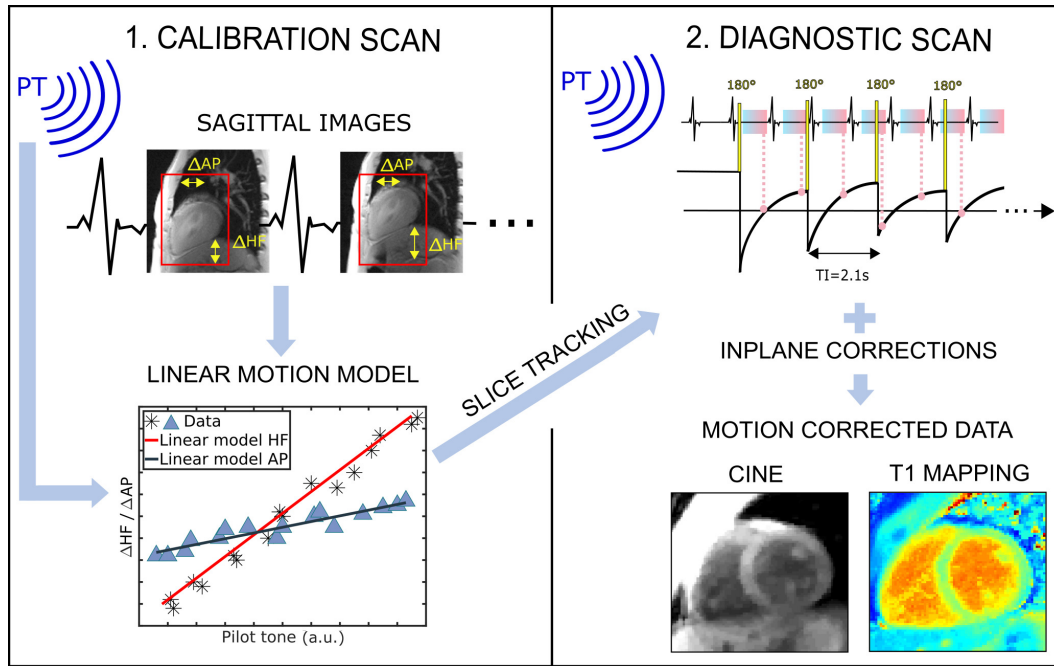
Figure 7.1: *The motion correction method with the PT consists of two steps, the calibration scan, and the T_1 mapping scan. During the calibration, HF and AP motion of the ROI covering the heart are registered and correlated with the PT by two motion models. During the motion corrected T_1 mapping scans, the RF excitation pulse is adjusted for every readout to follow the heart motion during the scan (slice tracking). In-plane motion correction is applied to the acquired k-space data retrospectively. A modified version of this figure was published in J2.*

shimming volume was utilized. Translational motion of the heart in HF and AP direction is then estimated using image registration. The registered displacement of the heart and HF and AP direction, and the pilot tone can then be correlated by linear motion models, as described previously in section 4.2.2. In the subsequent T_1 mapping scan, these models are used to predict the shift of the heart based on the obtained PT signal. The accuracy of the motion correction achieved by the PT is limited by the linear motion model and the calibration scan, which only covers motion in the sagittal plane.

7.2.2 Continuous radial acquisition

To obtain T_1 maps and functional cine images from the same raw data, a continuous golden-angle radial data acquisition is used [176]. Seven inversion pulses, indicated as yellow bars in Figure 7.2, are applied repeatedly with a fixed predefined delay of 2.1 s. This delay has been shown to allow for accurate T_1 mapping for a wide range of different heart rates [159, 176]. The start of the scan is triggered to mid-diastole, but the following inversion pulses and acquisitions are carried out independent of the cardiac phase. From the same raw data cine images can be reconstructed that allow to differentiate between cardiac phases and enable T_1 mapping for diastole and

systole.

7.2.3 Motion correction

The imaging slice orientation is oblique. Because the PT frequency position must not change during acquisition, only shifts along the slice normal are applied prospectively. For this, the excitation RF pulse is adjusted for each readout without delay. The adapted slice position $\Delta \overrightarrow{SL}$ is then the orthogonal projection of the predicted shifts ΔHF_{pred} and ΔAP_{pred} onto the slice normal $(\overrightarrow{SN})$ of the scan orientation, as previously described in section 6.2.1. A retrospective in-plane correction of translational motion, as described in section 6.2.2 with the correction values ΔPE and ΔRO is also performed.

The entire process of extracting the PT signal from the raw data and calculating the corresponding slice shifts is implemented in the reconstruction pipeline of the vendor allowing direct communication with the running sequence.

After motion correction, artifacts induced by RL heart motion, which is not accounted for in the motion model, might be present. It is assumed that the amplitude of this residual motion is small. Therefore, it is sufficient to subdivide the acquired data into four different motion states based on the PT signal, to resolve the motion accurately.

The non-rigid image registration using a b-spline-based algorithm with mutual information as similarity metric is carried out using regularization with a bending energy penalty [177]. The first 100 readouts were not used to estimate the motion fields because after the first inversion pulse, the received MR signal is in a very different transient state before reaching a steady-state compared to the rest of the acquisition. Also, the PT of the first 100 readouts may not be as accurate as the following signal because a median filter with a width of 100 readouts was applied to the PT to reduce noise in the signal. This affects less than 5% of the total number of radial lines and, hence, there is still sufficient data available for motion estimation. The obtained motion fields are then applied in subsequent motion-corrected image reconstruction to further minimize respiratory motion artifacts [57, 157, 178].

7.2.4 Cine reconstruction

Cine images are reconstructed from the same raw data used for T_1 mapping by resorting the radial lines into different cardiac phases based on the recorded ECG signal [159]. In addition to the first 100 readouts not used for motion correction, image data acquired after an inversion pulse are excluded in the reconstruction to ensure a consistent dark blood contrast over all cardiac phases [176]. Respiratory motion fields are applied during TV-regularized respiratory motion-corrected image reconstruction [179]. This image reconstruction problem is solved iteratively, and the motion fields are included in the MR acquisition model [57]. The acquisition model, therefore, describes the weighting due to multiple receiver coils, motion

transformation, Fourier encoding and radial k-space sampling. Total variation (TV) regularization is applied spatially ($\lambda=10^{-3}$). Coil sensitivities were calculated combining all radial data. From the reconstructed cine images the rest period in diastole or systole are visually selected.

The cine images reconstructed from these data show a dark-blood contrast. This contrast results from applying global inversion pulses in the sequence and the fact that the T_1 of blood is longer than that of myocardium (1900 ms compared to 1100-1350 ms at 3T [180, 181]). To enhance contrast, only data are used where the signal from myocardium is already positive during relaxation. The signal of blood is not yet completely positive but still partly negative because of the longer T_1, resulting in a cancellation of blood signal intensities. [159].

Also reference cine images are acquired as in the previous chapter 6. These images show a bright-blood contrast, because no global pulses are applied and blood flows constantly into the 2D imaging plane. For GRE sequences the short TR lead to a reduction of the signal from static tissue in the slice because of saturation of the magnetization. The new blood flowing into the slice can be completely magnetized and thus emit a higher signal ("inflow effect") [182].

7.2.5 T1 mapping analysis

T_1 mapping is carried out for a predefined cardiac phase (e.g., mid-diastole or mid-systole). The acquisition windows for diastole are illustrated as part of an ECG signal in Figure 7.2. The pink region corresponds to mid-diastole. One T_1-weighted image per cardiac cycle is reconstructed with 43 radial lines for diastole, corresponding to an acquisition window of 202 ms. Because the cardiac cycle and the pattern of the inversion pulses are asynchronous, the images correspond to different inversion times (TI).
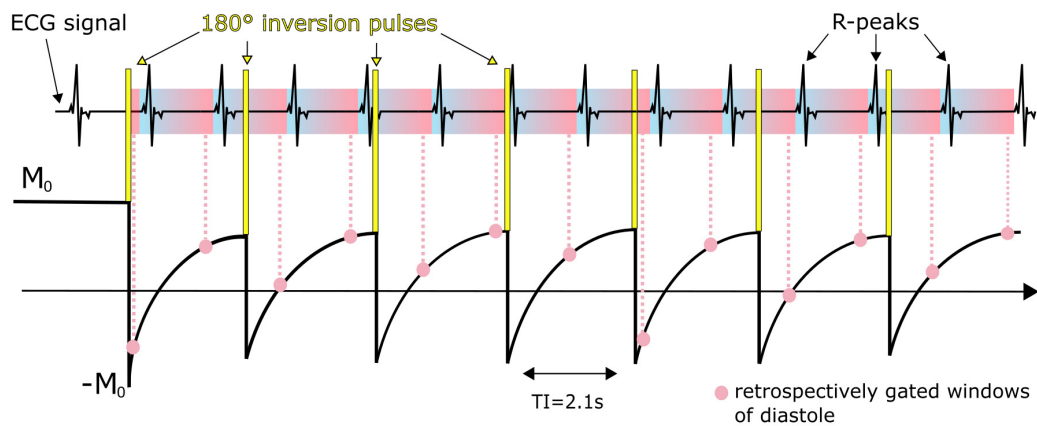
Figure 7.2: *Magnetization curve for continuously acquired data with seven inversion RF-pulses. In this scheme, only data from mid-diastole, indicated with pink dots, are used for T_1 reconstruction. This figure was published in J2.*

T_1 maps are reconstructed using the same TV-regularized image reconstruction as above. The respiratory motion fields are applied during image reconstruction to ensure all TI images are in the same respiratory phase. The longitudinal magnetization M after an inversion pulse can be described with a Look-Locker model [112, 113]. An extended inversion recovery Look-Locker model is used in a three-parameter fit to estimate M_0, T_1 and the flip angle (FA) voxel-wise [176]:

$$M(t) = M_0^{eff} - (M_j^+ + M_0^{eff})e^{-(t-(j-1)TI)/T_1^{eff}}, \qquad (20)$$

where j is the number of inversion, $M(t)$ is the relaxation after j's inversion, and M^+ is the magnetization before an IR pulse. The steady-state magnetization is defined as [113]:

$$M_0^{eff} = M_0 T_1^{eff} T_1^{-1} \qquad (21)$$

and T_1^{eff} is the effective relaxation time for low flip angles:

$$T_1^{eff} = [1/T_1 - (1/TR \ln(\cos(\alpha)))]^{-1}. \qquad (22)$$

Besides the mid-diastolic T_1 maps, systolic T_1 maps are reconstructed. To find the systolic cardiac phase, cine images are reconstructed, and the systole is visually selected. The cine images are used as a cardiac motion scout. The radial sequence provides optimal results for mid-diastole, i.e., it is started using cardiac triggering in mid-diastole. To accurately determine the T_1 for systole as well, the M_0, which is included in the fitting process for the generation of the systolic T_1 maps, is taken from the previously reconstructed diastolic T_1 maps.

7.3 Experiments

All measurements were performed with inhouse-programmed sequences on a 3T scanner (MAGNETOM Verio, Siemens Healthcare, Erlangen, Germany) on 11 healthy subjects (7 male, 4 female, age 30±7 years, weight 72±11 kg) after approval of the local ethics board. Written informed consent was obtained in all cases. In addition, phantom scans were carried out with an inhouse-built T_1 phantom placed on a moving cart, allowing for translational motion along the bore direction [183]. The diameter of the tubes inside the phantom is 2.75 cm and the motion amplitude in HF direction is 26.7 mm. The parts of image reconstruction and evaluation, which were required to apply the prospective correction, were implemented on the scanner, customizing the reconstruction chain (software syngo.MR B17). Retrospective motion correction, image reconstruction, and estimation of T_1 were carried out using Python 3.7.
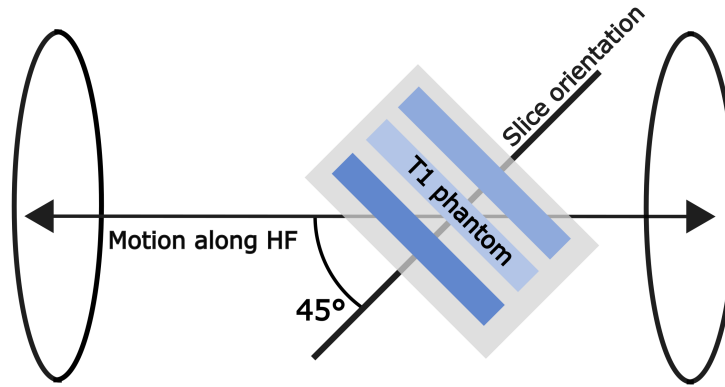
Figure 7.3: *Phantom setup showing the T_1 phantom and slice orientation tilted to the long axis in head-feet direction. This figure was published in J2.*

7.3.1 Scan parameters

For calibration, 2D ECG-triggered data were acquired over 45 cardiac cycles and 7.2±3.3 respiratory cycles in the diastolic phase in sagittal view with FOV=320×320 mm^2, voxel size=1.7×1.7×8 mm^3, TE/TR=2.1/4.7 ms and FA=5° using an in-house-modified spoiled gradient-echo sequence.

The simultaneous cine and T_1 mapping scan was performed continuously during ≈15 s using an inhouse-modified 2D spoiled gradient echo sequence (FOV=320×320 mm^2, voxel size=1.7×1.7×8 mm^3, TE/TR=2.1/4.7 ms) with a golden-angle radial trajectory [159] resulting in a total to 3080 radial lines. Seven inversion pulses were applied every 2.1 s independent of the cardiac cycle. The scan was carried out during free-breathing without (uncorrected) and with motion correction (corrected) and during a breathhold.

For comparing the cine data, a breathhold reference scan was acquired with the same scan parameters as used in section 6.3.3 for the cine scans (FOV=320×320 mm^2, voxel size=1.7×1.7×8 mm^3, TE/TR=3.2/5.9 ms, FA=12°, retrospectively ECG-gated).

An inversion recovery spin echo sequence (TI=25/50/300/600/1200/2400/4800 ms, TE/TR=12/8000 ms) was used to obtain reference T_1 values for the phantom.

In vivo a standard 5(3)3 MOLLI sequence with FOV=360x360 mm^2, slice thickness=8 mm, and in-plane resolution=1.4×1.4 mm^2 was used. MOLLI data were post-processed, and T_1 fitted inline at the scanner [184]. In addition, cine images with a standard gradient-echo sequence, FOV=320×320 mm^2, voxel size=1.7×1.7×8 mm^3, TE/TR=3.22/5.9 ms, and FA=12° were acquired.

In all subjects, a mid-ventricular SAX image was obtained. Additionally, a full stack of 10 SAX images, 4CHV images, and LA images were acquired in different subjects of this cohort. To reconstruct phantom T_1 maps comparable to the *in vivo* measurements, an ECG of a subject was used for cardiac gating of the phantom data. The phantom setup is displayed in Figure 7.3.

7.3.2 Analysis

For the analysis of the phantom data, nine ROIs were manually drawn in the center of each tube, and mean T_1 values were calculated and compared between the reference scans and the uncorrected and corrected scans, respectively. *In vivo* data were analyzed by segmenting the left ventricle, according to the American Heart Association consensus statement [185], and comparing T_1 values of the six segments of all subjects of the breathhold data with the uncorrected and corrected data, respectively. The effect of the motion fields is determined by calculating the R^2 of the T_1 fit of these segments with and without applied motion fields. MATLAB R2017a and Python 3.7 were used for the analysis. Statistical data result from the Wilcoxon test, where p-values <0.05 are classified as significant.

7.4 Results

7.4.1 Phantom
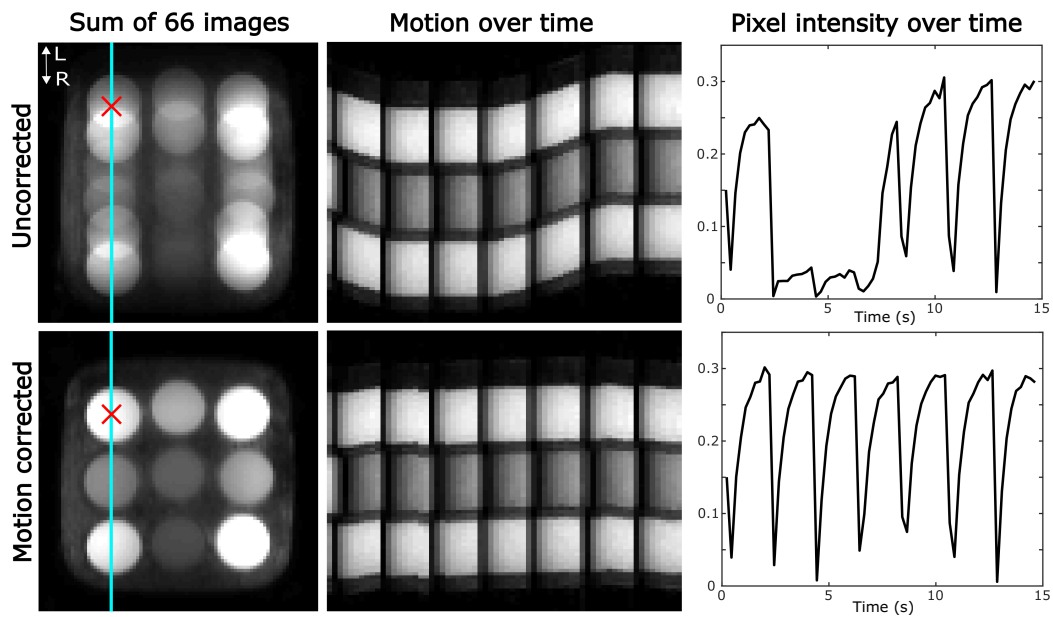
Figure 7.4: *Comparison of uncorrected (top) and corrected (bottom) data. Left: 66 images, each reconstructed from 43 radial lines were overlayed. Middle: Single line from the left image (cyan) displayed over $\approx$15 s to show the change in phantom position during measurement. Black dropouts are due to the inversion pulses. Right: Intensity change of one pixel (red cross) over $\approx$15 s. This figure was published in J2.*

Due to the angulation of the phantom through-plane and in-plane motion were present. The shift along HF estimated with the calibration scan was 21.8 mm. The correction applied during the diagnostic scan was 15.5 mm for through-plane motion and 15.4 mm for in-plane motion in readout direction.

Figure 7.4 gives an overview of 66 images, each reconstructed from 43 radial lines with and without motion correction. To reconstruct phantom T_1 maps comparable

(A)

(B)
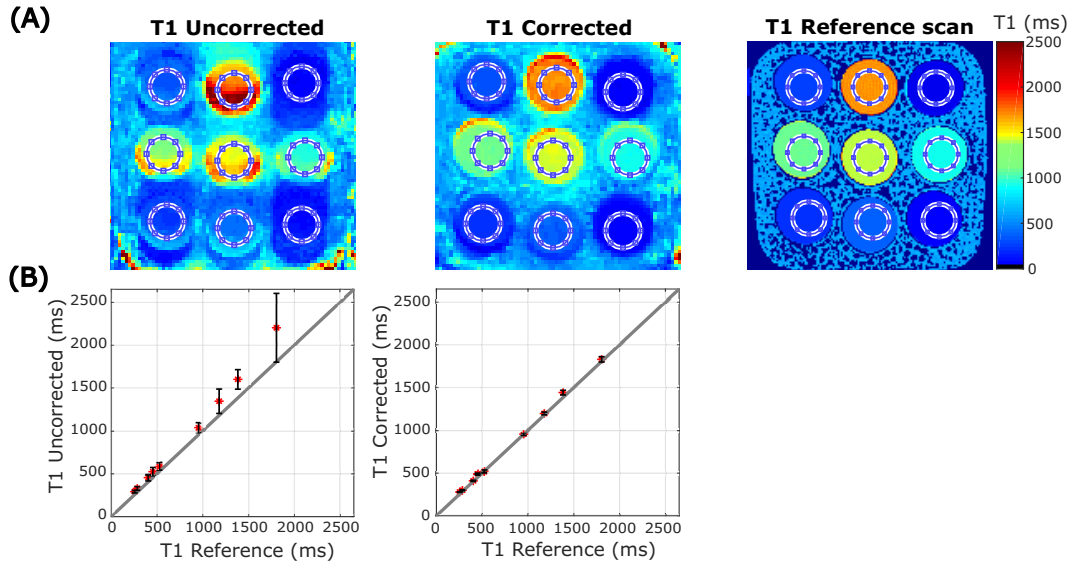
Figure 7.5: *(A) T_1 maps of a moving phantom without motion correction and with motion correction. For comparison, a reference scan was performed using an inversion recovery spin echo sequence. Circles indicate the ROI. (B) T_1 of the tubes for the uncorrected with 14±4% difference and the corrected scans with 3±4% difference compared to the reference. The gray line indicates the identity line. This figure was published in J2.*

to the *in vivo* measurements, an ECG of a subject was used for cardiac gating of the phantom data yielding 16 images. The circular ROI was manually placed in the center of each tube with a diameter of 1.7 cm each not covering the residual motion artifacts at the border of the tubes. In Figure 7.5 the resulting T_1 maps are displayed (A), and the T_1 values of the uncorrected and corrected scans were compared to the reference T_1 (B). T_1 of the surrounding material is 713±23 ms. T_1 of the uncorrected data were significantly higher by 14±4% (p=0.008) than the reference T_1 values. This is because the model fitting based on the reconstructed images does not work for some pixels, due to the motion of the phantom, and the T_1 values are overestimated. The difference between the corrected T_1 values and the reference T_1 values was 3±4% and was significant (p=0.02). The T_1 maps of the reference scan have a higher resolution and its acquisition time was 7× 23 min during which the phantom was motionless, such that the estimation of T_1 is very accurate.

7.4.2 In vivo

T_1 maps of one subject were excluded from analysis because the reference breathhold scan was mistriggered, which affected the comparability. The mean amplitude of the respiratory induced heart motion across all subjects in the two calibration directions HF and AP were 13.9±6.5 and 4.8±3.4 mm, respectively. The mean through-plane motion $\Delta\overrightarrow{SL}$ corrected during the running sequence with the PT was 7.4±3.7 mm. Retrospective in-plane motion correction based on the PT was applied for a mean

motion amplitude of 6.5±5.2 mm. The average amplitude of the non-rigid MF in a ROI around the heart was 1.1±0.4 mm.

Three *in vivo* T_1 maps of the systolic heart phase acquired during free-breathing without correction and with correction are shown in Figure 7.6. For comparison, data were also acquired during a single breathhold and using MOLLI as a visual reference. Each method was acquired in a separate scan resulting in small differences in the visualized anatomy. Motion artifacts were reduced by applying the motion correction method. T_1 maps are visually comparable to T_1 maps obtained by the MOLLI sequence. 15±3 T_1-weighted source images went into estimating the T_1 maps on average. Motion artifacts were reduced by applying the motion correction method. T_1 maps are visually comparable to T_1 maps obtained by the MOLLI.

Figure 7.7 shows Bull's-eye plots representing the mean T_1 values and standard deviations of ten subjects for 6 myocardial segments. Differences of the uncorrected data to breathhold data and corrected data to breathhold data were calculated, and segments marked with * are classified as significantly different. The mean values across all segments and subjects for the uncorrected data are 1557±377 ms, for the corrected data 1283±33 ms, and for the breathhold data 1240±57 ms. Motion correction resulted in T_1 values being more uniform as for the uncorrected T_1 maps
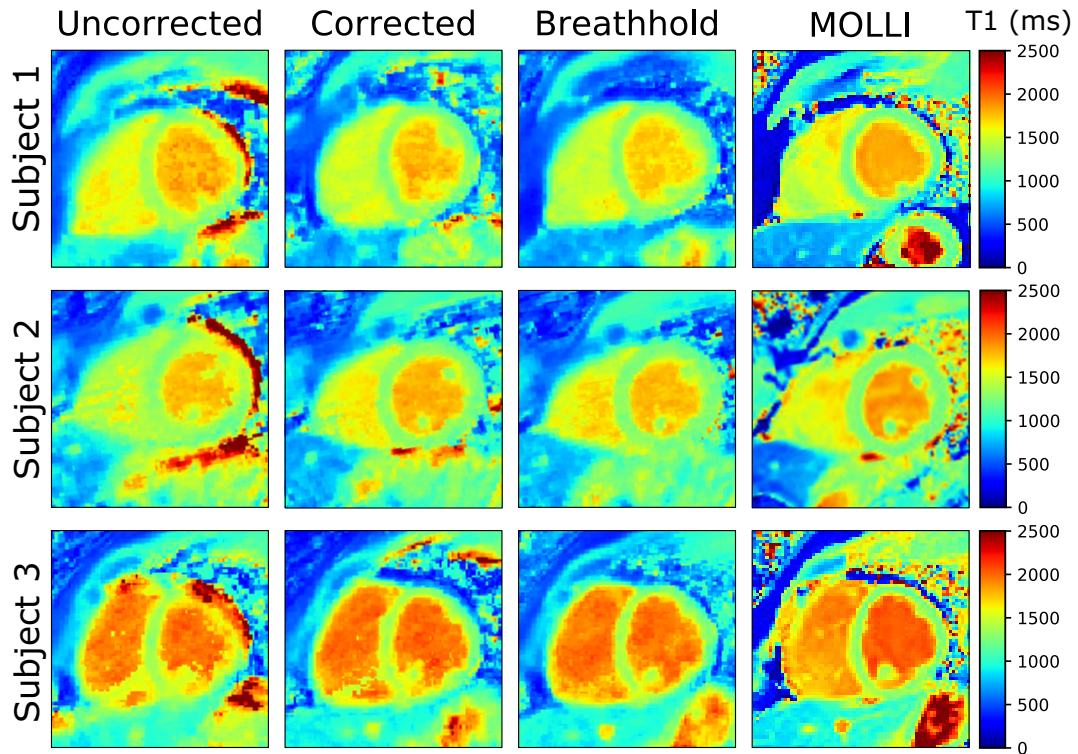
Figure 7.6: *Native T_1 maps of three subjects acquired with a continuous radial trajectory during free-breathing without (uncorrected) and with motion correction (corrected). For comparison, T_1 maps acquired during a breathhold and MOLLI (also acquired during a breathhold) are displayed. Each method is acquired in a separate scan resulting in small differences in the visualized anatomy. This figure was published in J2.*
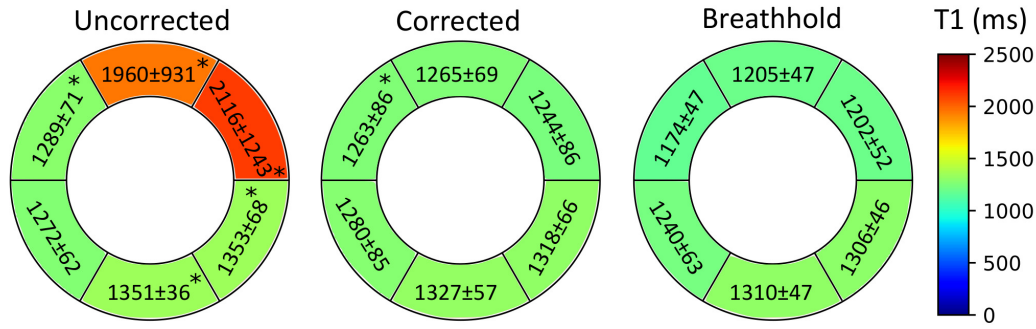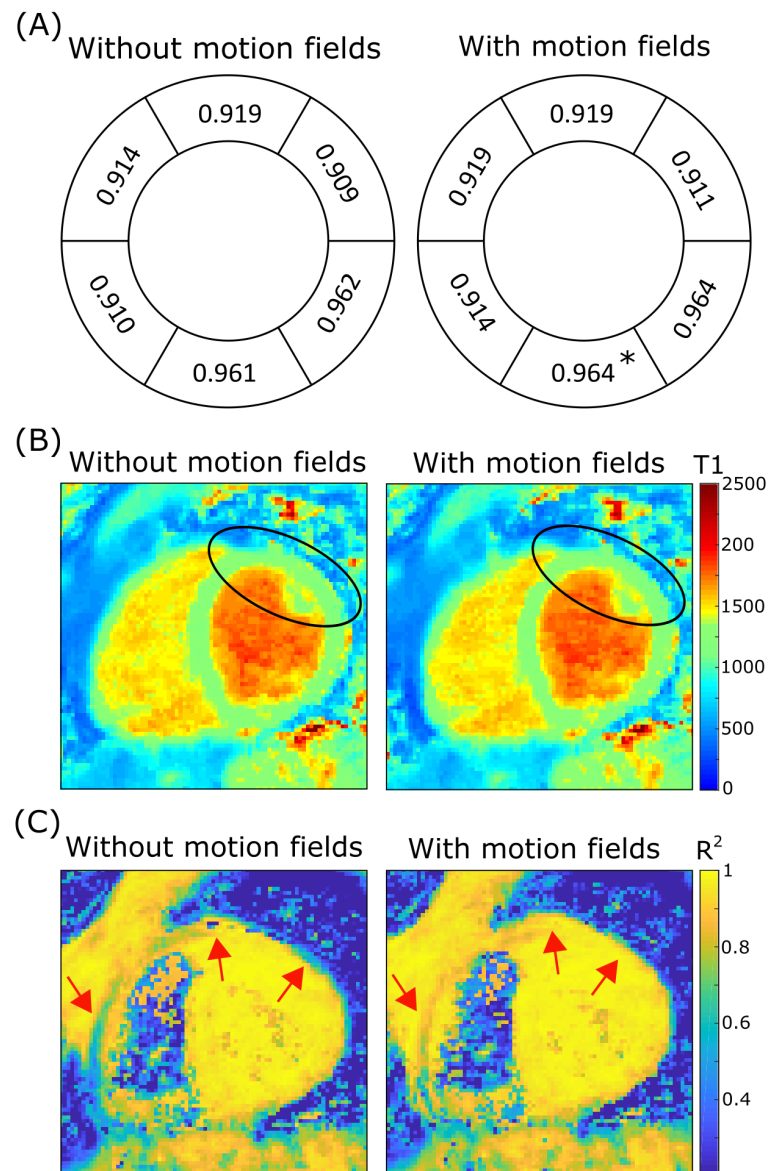
Figure 7.7: *Bull's-eye plots representing six myocardial segments of mid-ventricular slices displaying T_1 and standard deviations averaged across 10 subjects in milliseconds. Segments marked with * are classified as significantly different. This figure was published in J2.*

across the myocardium. Respiratory motion led to an average overestimation of T_1 values by $26\pm31\%$ compared to breathhold T_1 maps. Average difference of T_1 between breathhold and the free-breathing approach was $3\pm2\%$ ($p<0.05$). The greatest improvements were achieved for the anterior and anterolateral segments, i.e., the segments directly adjacent to the lung. Averaged over these two segments, the T_1 values before correction were $69\pm7\%$ higher than the reference breathhold values. This difference was reduced to $4\pm1\%$ with the motion correction.

The mean R^2 of the fitted T_1 model without applied motion fields and with motion fields for 6 segments and 10 subjects are displayed in Figure 7.8A. Differences of the R^2 without and with motion fields are not significant except in the inferior segment. Figure 7.8B and 7.8C show the T_1 maps of a subject and the corresponding R^2 of the model fit. The arrows point to areas where the motion fields result in improvements of the fit. Although the differences in T_1 are very small between these two reconstructions, the non-rigid motion correction leads to an improvement in R^2 especially along the edges of the myocardium suggesting a better alignment between the images used for the T_1 fit.

Cine images with 28 ± 3 heart phases were reconstructed from the same k-space data as the T_1 maps. Figure 7.9 shows systolic and mid-diastolic images acquired during free-breathing with and without motion correction and additionally acquired during a breathhold. As a reference, a standard GRE cine is also shown. With motion correction, respiratory artifacts were strongly reduced and the visibility of the myocardium was improved. This enabled accurate determination of static periods in cardiac cycle.

Figure 7.8: *(A) Bull's-eye plots representing the R^2 of T_1 model for T_1 maps without applied motion fields and with motion fields. * indicates the segment where the differences are significant (B) T_1 maps of a subject without motion fields and with motion fields (C) R^2 map of the same subject with arrows pointing at regions where the motion fields result in improvements of the fit. Parts of this figure were published in J2.*
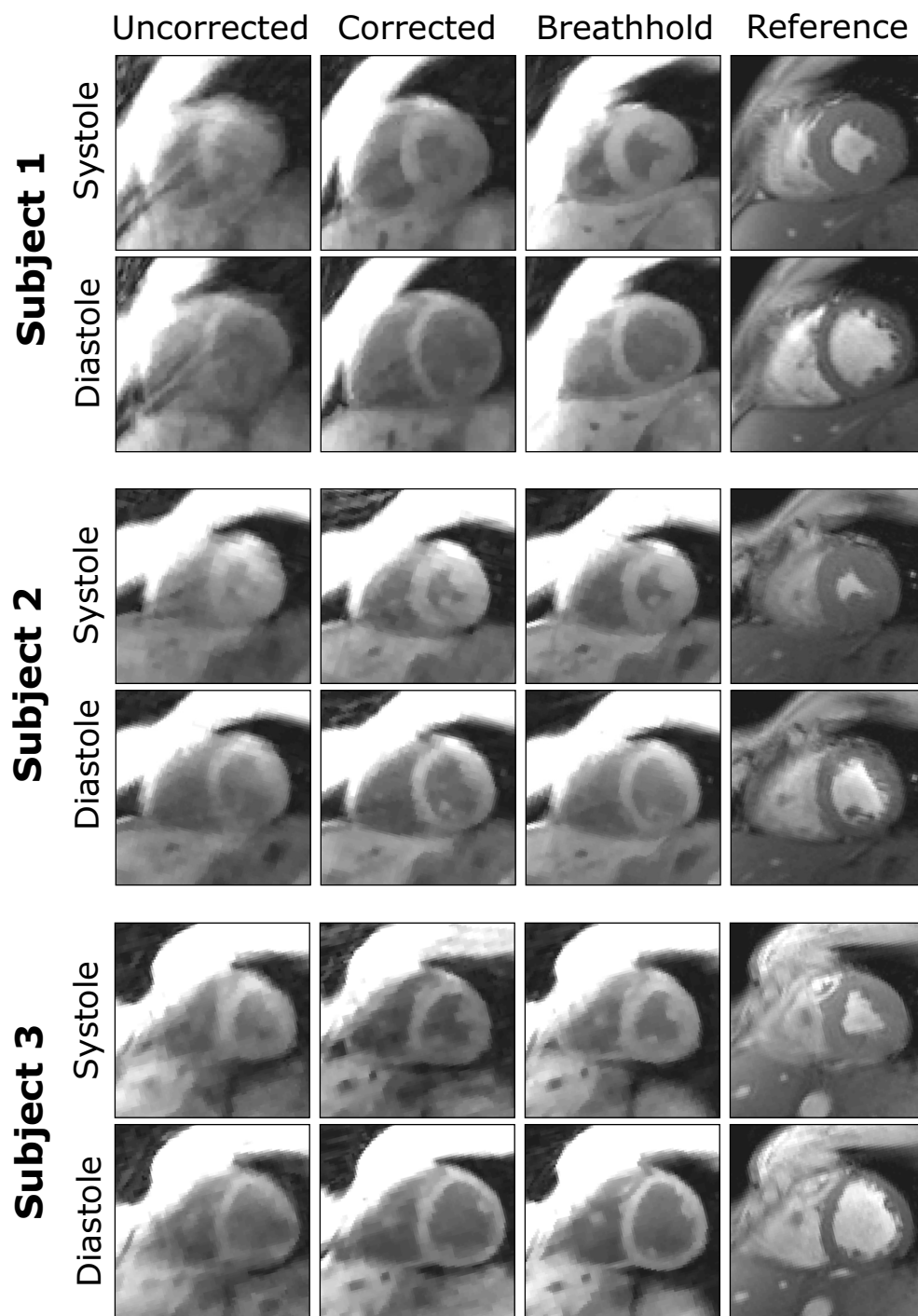
Figure 7.9: *Systole and mid-diastole of three subjects acquired during free-breathing with and without correction. For comparison, breathhold data is also shown together with reference data. This figure was published in J2.*

Furthermore, the T_1 maps reconstructed in systole and diastole with motion correction and during a breathhold are shown in Figure 7.10 for two subjects. In order to identify peak systole and optimize the reconstruction window to minimize cardiac motion artifacts, cine images were used as a scout. 30 and 23 radial lines corresponding to a reconstruction window of 141 and 108 ms were used for subject 4 and 5, respectively. The same window duration for systolic and diastolic static periods were used for better comparability.
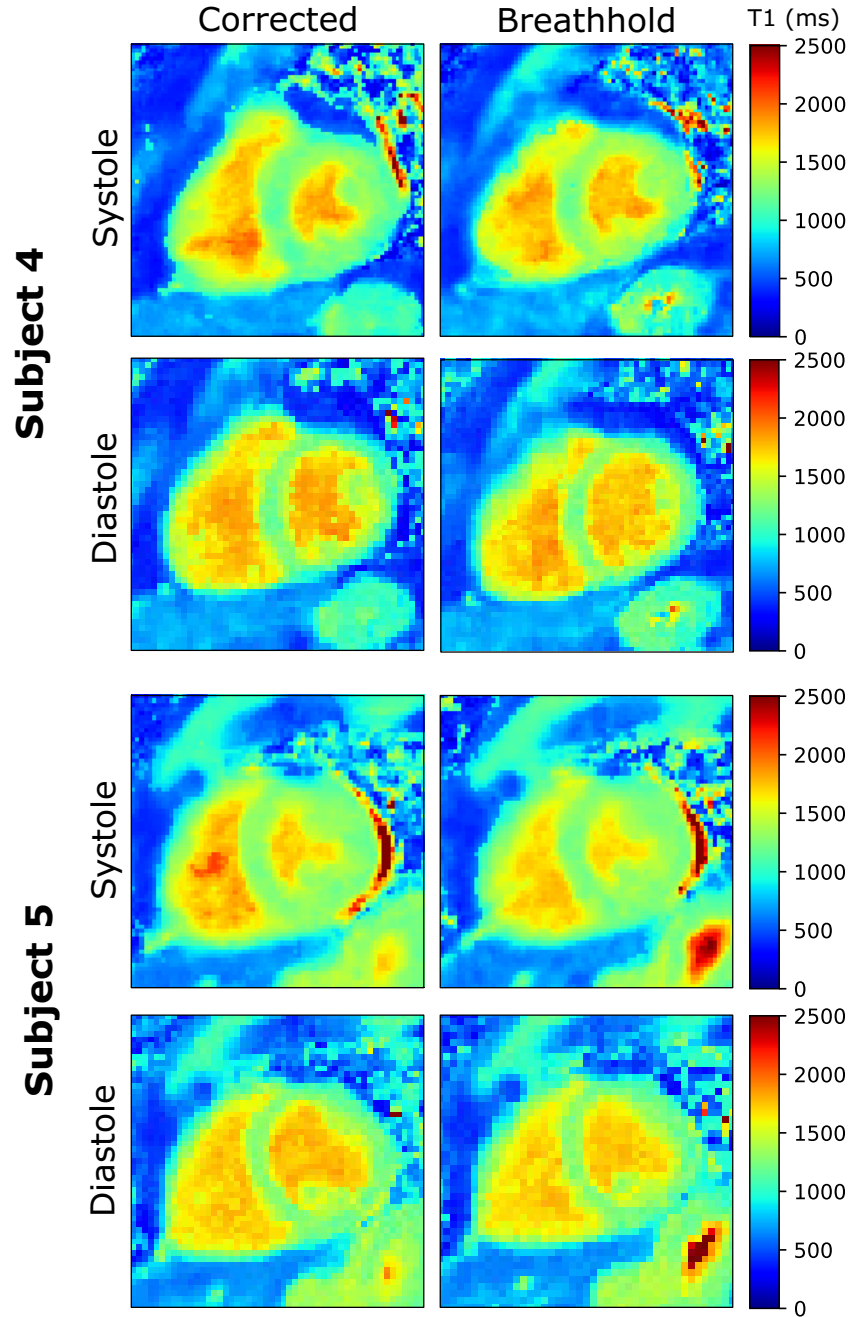
Figure 7.10: *Native T_1 maps of systolic and diastolic heart phases of two subjects with motion correction (corrected) and for comparison of breathhold data acquired during a separate scan. This figure was published in J2.*
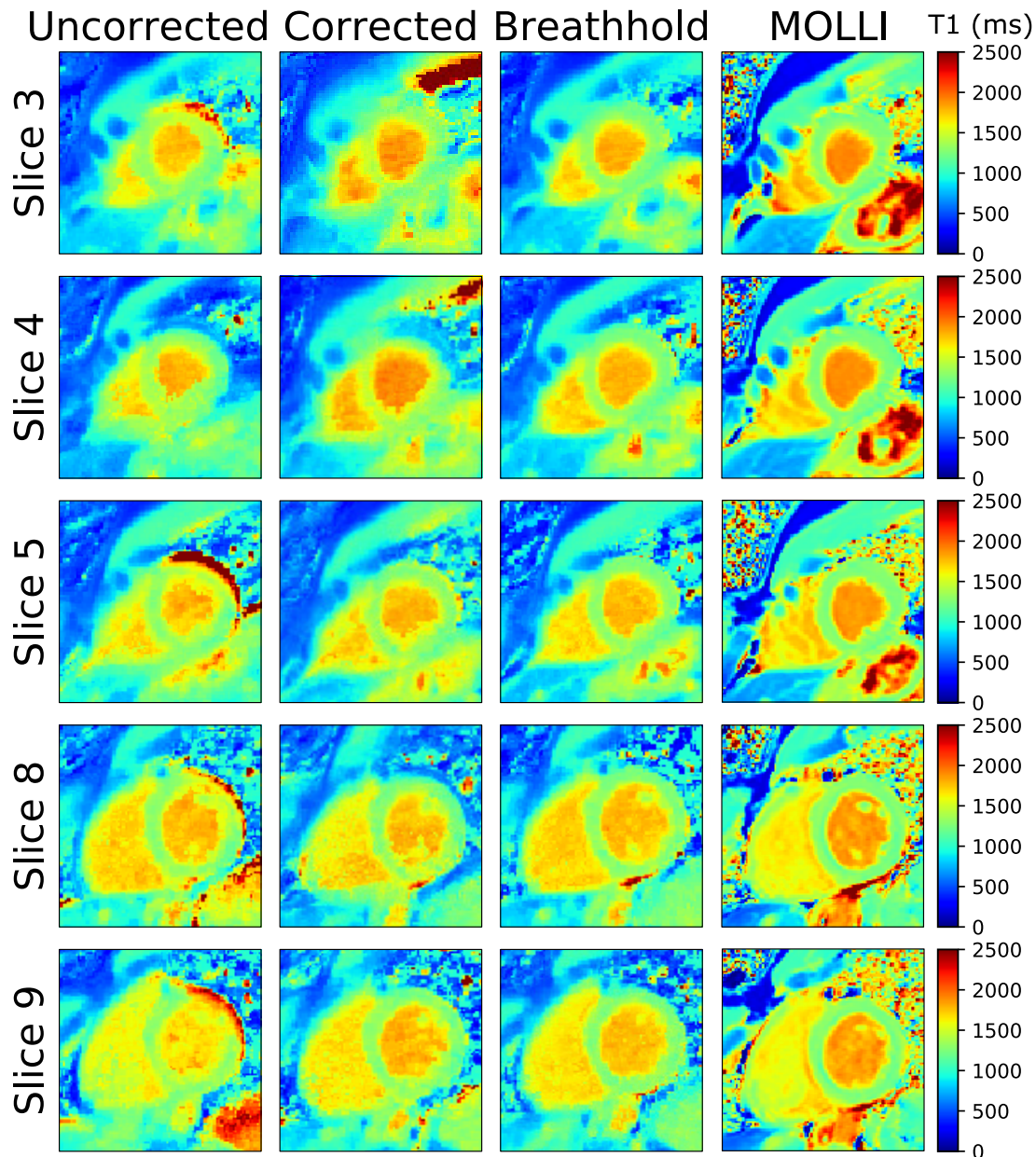
Figure 7.11: *SAX T_1 maps in one healthy subject. 10 slices (5 displayed) were recorded, covering the complete left ventricle. The same calibration data was used for all corrected images. For comparison, resulting maps of a breathhold scan and MOLLI are displayed. Motion correction leads to a reduction of respiratory artifacts. Each method is acquired in a separate scan resulting in small differences in the visualized anatomy. This figure was published in J2.*

Figure 7.11 shows five out of 10 T_1 maps of Subject 2 covering the left ventricle in SAX acquired during free-breathing without correction and with correction. The motion correction was based on the same calibration scan for all slices. Again, for comparison, data were also acquired during a single breathhold and using MOLLI as a visual reference.
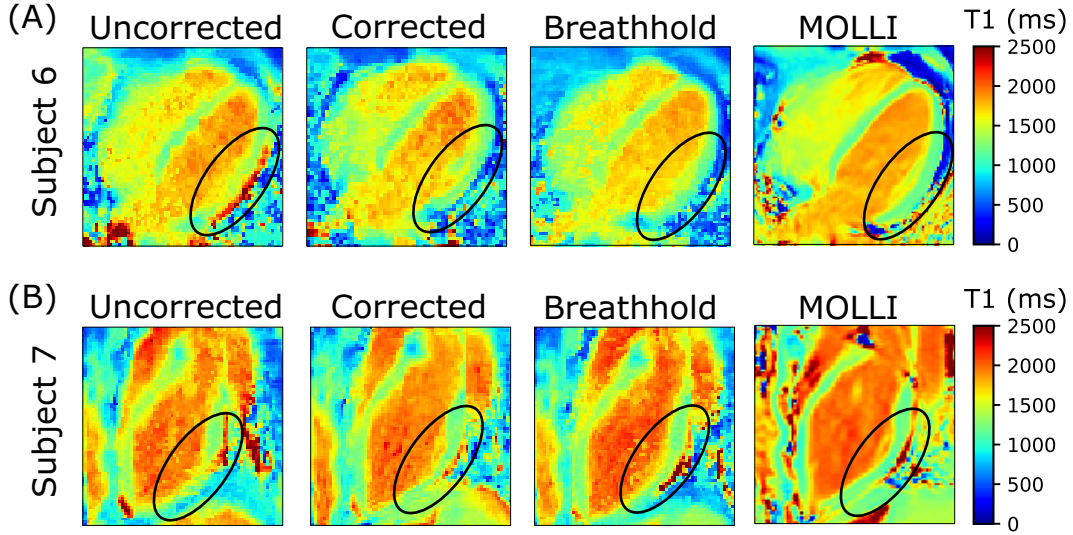
Figure 7.12: *(A) Mid-diastole in 4CHV and (B) LA for two subjects acquired during free-breathing with and without correction. For comparison, breathhold data is also shown together with MOLLI data. The black circles highlight the lateral wall of the left ventricle. This figure was published in J2.*

In Figure 7.12 T_1 maps of two different subjects in 4CHV and LA are shown with and without motion correction under free-breathing conditions. For comparison, a breathhold scan and a MOLLI T_1 map are also displayed. The T_1 values in the lateral wall of the left ventricle, as highlighted with black circles in Figure 7.12, are more uniform with motion correction than without motion correction.

7.5 Discussion

In this chapter, the feasibility of PT-based prospective motion correction for free-breathing T_1 mapping and simultaneous cine imaging was shown using the PT as a motion surrogate. Phantom and *in vivo* measurements demonstrated improved image quality and T_1 quantification using the motion correction approach compared to motion uncorrected imaging.

In a phantom study, T_1 values obtained with motion correction showed accurate T_1 quantification over a wide range of T_1. Changes of the phantom over time due to motion lead to inaccurate T_1 estimation, especially in areas with large differences between neighboring T_1 values. The material, surrounding the nine tubes, had a low T_1 of 713±23 ms. Therefore, the error of T_1 quantification was highest for tubes with a high T_1 value.

A similar effect could be seen in the in-vivo applications. The highest errors in T_1 quantification were found in the anterior and anterolateral segments which border to the lung and showed very large signal differences. Significant differences were found between the uncorrected scan and the breathhold scan for all segments except the inferoseptal segment. The motion-corrected T_1 maps showed very similar T_1 values to the breathhold scan, except for the anteroseptal segment. Nevertheless, in this

segment T_1 values were lower in the breathhold scan compared to the other segments. The breathhold scan was always performed in the end-expiratory state. However, for slice tracking, an arbitrary breathing state was used. The motion-corrected image may, therefore, show a different position in the SAX and could lead to errors in the quantitative comparison.

Variations in heart rate or arrhythmias may result in TI images acquired at different cardiac phases and produce inaccuracies in the T_1 maps [115, 186]. For such patients, the short resting phase of systole must be found very precisely. For this purpose, cine images were reconstructed, which were used as temporal scout to find the systole. The cine images reconstructed from the continuous data acquisition showed poorer image quality compared to a conventional cine scan. Nevertheless, they provided cardiac motion information which allowed for the retrospective optimization of the data used for T_1 mapping.

The calibration scan was performed in a mid-ventricular ROI. As a result, the motion of the mid-ventricular area was assumed to be estimated best. Nevertheless, high image quality could be seen for all SAX images in the full stack of slices of a subject, covering 8 cm along the long axis of the heart. A radial acquisition scheme was chosen because it allowed combining cine imaging and T_1 mapping in one scan. In addition, radial acquisitions are more robust against motion artifacts.

One of the limitations of this study is, that the rigid motion correction was only performed for HF and AP direction (i.e., the two prominent directions of motion [28]) was performed. Additional correction of RL motion could further improve image quality. Also, the same motion model for inspiration and expiration was used, neglecting any hysteresis effects. Nevertheless, previous results (section 6.4.2 Fig. 6.4) have shown that these effects are small.

The correction of each individual readout line leads to inconsistency for static tissue, which is then seen as streaking. But the T1 fit is not affected by this, because these streaking artifacts are incoherent along time.

Depending on the subject and the selected slice orientation, the motion amplitude varied. The determined motion model and correction parameters were only valid for the chosen heart region but were applied globally to all image data. The surrounding static tissue (e.g., back and spine) or tissue that moves differently from the heart (e.g., liver) are wrongly corrected, which can result in artifacts. However, for radial trajectories, these artifacts mainly lead to streaking artifacts which did not impair the T_1 estimation of the heart in this study.

After PT-based rigid motion correction in the cardiac region, the residual motion fields were on average small (1.1±0.4 mm) for SAX orientation, which indicated that the PT-based motion correction was already very accurate.

Although motion artifacts are not immediately visible in the T_1 maps, respiratory motion still impacted T_1 quantification, as was shown in Figure 7.8C. The small differences of R^2 are because the selected segments do not necessarily include tissue transitions and because the T_1 values are averaged across the segment. The

additional motion correction with the motion fields could further minimize residual motion and improve T_1 fitting. Correction of in-plane respiratory motion is applied retrospectively, and motion fields were estimated from the same data used for T_1 mapping. Hence this step did not require any additional scan time.

For the reconstruction of the T_1 maps for systole, the model parameter M_0 was taken from the model fit of the previously reconstructed diastolic images. To improve the T_1 quantification, the same sequence could be started in systole instead of mid-diastole.

Studies in patients who may have more complicated cardiac motion due to disease are still needed to assess the applicability of this approach to routine clinical practice.

7.6 Conclusion

In this chapter, free-breathing myocardial T_1 mapping and simultaneous cine imaging using a radial acquisition trajectory combined with a PT-based prospective respiratory motion correction was presented. The method was tested on a motion phantom and improved the T_1 estimation accuracy compared to uncorrected data. Also, for the motion corrected *in vivo* data more accurate T_1 values were obtained for the myocardium than for the uncorrected data. Cine images showed fewer motion artifacts using the motion correction approach. A future application of the method would be high-resolution T_1 mapping, where the scan time is longer than a breathhold. Further studies are needed to confirm this method in clinical practice.

8 | Summary

In this thesis, a novel PT-based respiratory motion correction method for cardiac MRI was developed. This real-time approach is particularly beneficial when breath-holding techniques can not be applied. The PT technology provides a stable motion surrogate which is independent of the MR data acquisition and its signal sampling does not interrupt the steady-state during the measurement. Because of these features, the technology is widely suited for many applications.

In this work, the robustness of the PT was shown to be comparable to other motion surrogates. The scale-free PT signal was successfully converted into a quantitative surrogate by performing calibration scans and deriving motion models. Furthermore, it was demonstrated that the motion correction technique is applicable to retrospective correction of 3D data and prospective correction of 2D images, where data was recorded using a Cartesian as well as a radial sampling scheme. The presented respiratory motion correction method was tested on a phantom and on healthy subjects and improved image quality compared to the uncorrected data in three different applications.

In chapter 3 the experimental setup of the motion phantom and the PT as well as the acquisition framework was presented. The adjustable parameters, i.e., amplitude and frequency, were optimized by testing various settings, such that a robust motion surrogate signal was available for further experiments. Image quality impairment due to the PT was minimized by subtracting a PT model signal from the k-space data.

Because the PT is a very sensitive detector its signal was degraded by high frequency noise due to vibrations. By applying an adaptive median filter with a sliding window step size of 100, the noise was removed from the signal. A signal delay of ≈0.6 s was introduced, which is short compared to the length of a respiratory cycle.

Chapter 4 addressed the calibration procedure of motion surrogates to respiratory heart motion. Utilizing calibration scans, subject-specific linear motion models were derived. With the models the qualitative PT was converted to a quantitative motion signal. Further, the temporal stability of the PT in conjunction with the models was tested and was found to be very high, with only a small increase of the mean absolute error (MAE) between the predicted and the registered shift by approximately 1.6 mm in the HF direction after a period of ≈8 min. On a phantom it was shown that the PT with the motion model is long-term stable with an MAE of less than 2.5 mm after ≈53 min in HF direction.

Other commonly used motion surrogates, i.e., the respiratory belt and the MR-navigator, were compared with the PT by acquiring cardiac MR data simultaneously with the surrogates. Linear motion models from the calibration scan yielded the

highest R^2 and best temporal stability for the MR-navigator (R^2=0.95), followed by the PT (R^2=0.79) and the respiratory belt (R^2=0.75). The smallest R^2 resulted from the respiratory belt because the temporal synchronization of the belt with the MR data was possibly not accurate, due to the different temporal resolutions of the surrogate signals.

In chapter 5 motion correction was performed retrospectively on 3D data using the three motion surrogates. The PT and the MR-navigator led to an improvement in visibility of the coronary artery. However, the advantage of the PT over the MR-navigator is its applicability also for continuous scans.

Also, the PT was initially tested for prospective motion correction in chapter 5. For this purpose, dynamic transverse 2D images of the heart were corrected prospectively along the dominant HF motion direction. This method was successful in reducing respiratory motion artifacts and served as a proof-of-concept for a prospective motion correction.

Further, the dominant respiratory motion amplitudes of the heart during an MR examination were determined to gain more information for the specific design of the calibration scan. Existing data of a study on 23 subjects was analyzed. The mean motion magnitudes for normal breathing were 8.53±2.55 mm, 2.07±0.97 mm and 1.52±0.92 mm for HF, AP and RL direction, respectively, and are in accordance with literature [147].

The objective in chapter 6 was to apply the PT-based motion correction to continuous cine imaging with oblique slice orientation. Because for the prospective motion correction the time between calibration scan and motion correction scan should be kept short, only sagittal 2D images were acquired for the calibration, as this orientation captures the two dominant directions of motion, HF and AP.

Again dynamic images were acquired, but the slice orientation was changed from transverse to short axis. It was shown on *in vivo* data, that the sharpness of anatomical regions (e.g., the heart) enhanced. The surrounding static tissue (e.g., spine) or tissue moving differently to the heart (e.g., liver), was wrongly corrected and lead to residual artifacts in the images.

From the calibration scans it has been shown on 10 subjects, that only small differences (i.e., hysteresis effects) between inspiration and expiration were found. Therefore, subject-specific linear models were a suitable solution for approximating the respiratory motion of the heart.

The quality of the PT-corrected cine images improved for all subjects relative to the uncorrected images. Analysis of the left ventricular blood pool areas showed that the mean differences between the breathhold method and the motion correction with the PT were <3%, with SDs of 13% and 15% for systole and diastole, respectively, and not significant. Compared to the uncorrected images, CNR was improved by 75±47% and the sharpness of endocardium was improved by 30±27% using the PT approach. There was no significant difference between PT-corrected data and breathhold data.

In addition to the qualitative cine images, the proposed PT motion correction method also improved quantitative cardiac T_1 maps, presented in chapter 7. Motion correction was extended by a retrospective non-rigid correction step, and resulted in T_1 values across the myocardium being more uniform as for the uncorrected T_1 maps. Without motion correction respiratory motion led to an overestimation of T_1 values by $26\pm31\%$ compared to breathhold T_1 maps, which was successfully corrected using the PT-based approach ($3\pm2\%$ (p<0.05)). Specifically in the segments which border the lung, i.e., anterior and anterolateral segments, the average T_1 values before correction were $69\pm7\%$ higher than the reference breathhold data. After motion correction, average errors in these two segments were reduced to $4\pm1\%$.

The non-rigid motion fields that were estimated retrospectively did not lead to a visible change of the T_1 maps. A significant difference of the R^2 without and with motion field correction was found only in the inferior segment. The fact that the application of motion fields to the image data causes only such small effects underlines that the rigid correction with the PT is already very accurate.

Nevertheless, improvements of the novel method could still be achieved in the future. Throughout this work, the PT was recorded with the same coils as were used for imaging. Although the main PT signal can be removed from the oversampling region, even a small residual signal can impair the final image quality. The setup could be optimized, such that the PT is recorded by an independent integrated receiver coil, which would allow for the PT to be shifted even further away from the imaging signal and hence reduce the negative effect of any residual PT signals.

In order to get a signal, free of artifacts caused by vibrations, it would be possible to integrate the PT emitter within the receiver coils. This would eliminate the sources of error that degrade the PT signal, which were presented in chapter 3.

With signal quality improvements, other optimization steps would be enabled, for example, multiple receive channel signals could be combined for a more robust surrogate signal. A coil combination would have the advantage that it would sample signals at different spatial points and in combination with a PCA possibly result in a more reliable and noise reduced surrogate.

Furthermore, prediction filters like the Kalman filter could be applied to the signal. The filter determines an adaptive forecast based on the analysis of previous estimations [134]. Applying this predict-ahead filter could compensate even the delay of a single TR, and thus be suitable for real-time applications.

Another field for optimization is the use of more advanced models, such as affine motion models [46, 47, 187]. With these motion models, different breathing types can be classified, such as deep breathing and short breathing, and also hysteresis effects could be included [135]. Affine correction could be applicable to the whole heart and would be more accurate. But the computational complexity and processing time would also increase.

Besides the potential improvements, there are also new future perspectives. In this study, T_1 maps were reconstructed for two cardiac phases from the data acquired

with the applied radial sequence. Previously, Becker et al. [176] used this sequence to obtain T_1 maps for multiple cardiac phases. In the future, it could be a goal to use the respiratory motion correction method presented here for free-breathing cardiac-resolved T_1 mapping.

Also, the PT could be used for other MR imaging strategies for the heart that are limited by breathhold duration (e.g., perfusion or MRF). With the PT, free-breathing acquisitions with accurate prospective motion correction can be performed for up to ≈ 53 min, as the PT is temporally stable and available with high temporal resolution.

Other fields of application of the PT are multimodal approaches, e.g., when MRI is combined with PET [124] or motion correction is applied for other organs that are also affected by respiratory motion such as the liver.

An advantage of the PT technology, not highlighted in this work, is its applicability as an alternative to an ECG signal. Conventionally, the ECG electrodes are attached to the chest in proximity to the heart. The electrodes may impair MR image quality, and the correct placement costs patient preparation time. Both of these issues could be avoided with the PT. For this technique, the PT signal transmitter and emitter are placed close to the heart. The beating motion of the heart can be extracted by applying a PCA to the PT signal and separate the cardiac and respiratory components. Studies regarding cardiac triggering with the PT were recently conducted [122, 125, 188]. Using the PT as an alternative to the ECG would be of advantage in clinical environment.

In this work, it was shown for the first time that the use of the PT allows accurate prospective correction for free-breathing CMR acquisitions. With further optimization, e.g., calibration with advanced motion models and better integration of the hardware into the scanner, the PT could enable high-resolution sequence-independent respiratory motion corrected CMR.

References

1. OECD (2021), Cardiovascular Disease and Diabetes: Policies for Better Health and Quality of Care. doi: 10.1787/9789264233010-en.

2. Von Knobelsdorff-Brenkenhoff, F. & Schulz-Menger, J. Role of cardiovascular magnetic resonance in the guidelines of the European Society of Cardiology. *Journal of Cardiovascular Magnetic Resonance* **18,** 1–18 (2016).

3. Kramer, C. M. *et al.* Standardized cardiovascular magnetic resonance imaging (CMR) protocols: 2020 update. *Journal of Cardiovascular Magnetic Resonance* **22,** 1–18 (2020).

4. Jerosch-Herold, M. & Kwong, R. Y. Cardiac T1 imaging. *Topics in Magnetic Resonance Imaging* **23,** 3–11 (2014).

5. Xue, H. *et al.* Motion Correction for Myocardial T1 Mapping Using Image Registration with Synthetic Image Estimation. *Magnetic Resonance in Medicine* **67,** 1644–1655 (2012).

6. Li, D. *et al.* Coronary Arteries: Three-dimensional MR Imaging with Retrospective Respiratory Gating. *Radiology* **201,** 857–863 (1996).

7. Chuang, M. L. *et al.* Adaptive Correction of Imaging Plane Position in Segmented K-Space Cine Cardiac MRI. *Journal of Magnetic Resonance Imaging* **7,** 811–814 (1997).

8. Bush, M. A. *et al.* Prospective correction of patient-specific respiratory motion in T1 and T2 mapping. *Magnetic Resonance in Medicine* **00,** 1–13 (2020).

9. Santelli, C. *et al.* Respiratory Bellows Revisited for Motion Compensation: Preliminary Experience for Cardiovascular MR. *Magnetic Resonance in Medicine* **65,** 1098–1103 (2011).

10. Speier, P., Fenchel, M. & Rehner, R. *PT-Nav: a novel respiratory navigation method for continuous acquisitions based on modulation of a pilot tone in the MR-receiver* in *Proc ESMRMB Congress 2015* (2015), 97–98.

11. Schroeder, L. *et al.* Two-Dimensional Respiratory-Motion Characterization for Continuous MR Measurements Using Pilot Tone Navigation. *Proc. Intl. Soc. Mag. Reson. Med. 24,* 3103 (2016).

12. Mayer, P. At the Heart of the Matter: An Overview of Adult Echocardiography for the Non-Cardiac Sonographer. *Journal of Diagnostic Medical Sonography* **31,** 221–232 (2015).

13. Scully, P. R., Bastarrika, G., Moon, J. C. & Treibel, T. A. Myocardial Extracellular Volume Quantification by Cardiovascular Magnetic Resonance and Computed Tomography. *Current Cardiology Reports* **20,** 2–11 (2018).

14. Bluemke, D. & Pattanayak, P. Tissue Characterization of the Myocardium: State of the Art Characterization by MR and CT Imaging. *Radiol Clin North Am* **53,** 413–423 (2015).

15. Bing, R. & Dweck, M. R. Myocardial fibrosis: Why image, how to image and clinical implications. *Heart* **105,** 1832–1840 (2019).

16. Renz-Polster, H. & Krautzig, S. *Basislehrbuch Innere Medizin* 4th ed., 29. ISBN: 9783437410536 (Uran & Fischer Verlag / Elsevier, 2008).

17. Chambers, D., Huang, C. & Matthews, G. in *Basic Physiology for Anaesthetists* 111–116 (Cambridge University Press, 2019). ISBN: 9781108565011.

18. Herring, N. & Paterson, D. J. *Levick's Introduction Cardiovascular Physiology* 6th ed., 448. ISBN: 1498739849 (Taylor & Francis Group, 2018).

19. Calvert, J. W. & Lefer, D. J. in *Muscle* 2nd ed., 57–66 (Elsevier Inc., 2012). ISBN: 9780123815101.

20. *Medienwerkstatt Wissenskarten Blutkreislauf, URL: https://www.medienwerkstatt-online.de/lws_wissen/vorlagen/ showcard.php?id=2261&edit=0, [Online accessed: 2021/08/04, 11:02]*

21. Pouget, J. M. & Harris, W. S. Systolic time intervals in man. *American Heart Journal* **86,** 286 (1973).

22. Scheffler, K. & Lehnhardt, S. Principles and applications of balanced SSFP techniques. *European Radiology* **13,** 2409–2418 (2003).

23. Zhang, S. *et al.* Real-time magnetic resonance imaging of cardiac function and flow-recent progress. *Quantitative imaging in medicine and surgery* **4,** 313–329 (2014).

24. Tsao, J., Boesiger, P. & Pruessmann, K. P. k-t BLAST and k-t SENSE: Dynamic MRI With High Frame Rate Exploiting Spatiotemporal Correlations. *Magnetic Resonance in Medicine* **50,** 1031–1042 (2003).

25. Blaimer, M. *et al.* SMASH, SENSE, PILS, GRAPPA: how to choose the optimal method. *Topics in magnetic resonance imaging : TMRI* (2004).

26. Larkman, D. J. & Nunes, R. G. Parallel magnetic resonance imaging. *Phys Med Biol* **52,** 15–55 (2007).

27. Petitjean, C., Rougon, N. & Cluzel, P. Assessment of myocardial function: A review of quantification methods and results using tagged MRI. *Journal of Cardiovascular Magnetic Resonance* **7,** 501–516 (2005).

28. Scott, A. D., Keegan, J. & Firmin, D. N. Motion in Cardiovascular MR Imaging. *Radiology* **250,** 331–351 (2009).

29. McLeish, K., Hill, D. L., Atkinson, D., Blackall, J. M. & Razavi, R. A Study of the Motion and Deformation of the Heart Due to Respiration. *IEEE Transactions on Medical Imaging* **21,** 1142–1150 (2002).

30. Ludwig, J., Speier, P., Seifert, F., Schaeffter, T. & Kolbitsch, C. Pilot tone–based motion correction for prospective respiratory compensated cardiac cine MRI. *Magnetic Resonance in Medicine* **00,** 1–14 (2020).

31. Saremi, F., Grizzard, J. D. & Kim, R. J. Optimizing cardiac MR imaging: Practical remedies for artifacts. *Radiographics* **28,** 1161–1187 (2008).

32. Paling, M. & Brookeman, J. Respiration Artifacts in MR Imaging: Reduction by Breath Holding. *Journal of Computer Assisted Tomography* **10,** 1080–1082 (1986).

33. McClelland, J., Hawkes, D., Schaeffter, T. & King, A. Respiratory motion models: A review. *Medical Image Analysis* **17,** 19–42 (2013).

34. Forman, C. *et al.* High-Resolution 3D Whole-Heart Coronary MRA: A Study on the Combination of Data Acquisition in Multiple Breath-Holds and 1D Residual Respiratory Motion Compensation. *Magnetic Resonance Materials in Physics, Biology and Medicine* **27,** 435–443 (2014).

35. Feinberg, D. A., Rofsky, N. M. & Johnson, G. Multiple Breath-Hold Averaging (MBA) Method for Increased SNR in Abdominal MRI. *Magnetic Resonance in Medicine* **34,** 905–909 (1995).

36. Danias, P. G. *et al.* Navigator Assessment of Breath-Hold Duration: Impact of Supplemental Oxygen and Hyperventilation. *American Journal of Roentgenology* **171,** 395–397 (1998).

37. Ehman, R., McNamara, M., Pallack, M., Hricak, H. & Higgins, C. Magnetic Resonance Imaging with Respiratory Gating: Techniques and Advantages. *American Journal of Roentgenology* **143,** 1175–1182 (1984).

38. Stuber, M., Botnar, R. M., Danias, P. G., Kissinger, K. V. & Manning, W. J. Submillimeter Three-dimensional Coronary MR Angiography with Real-time Navigator Correction: Comparison of Navigator Locations. *Radiology* **212,** 579–587 (1999).

39. Kellman, P. *et al.* High Spatial and Temporal Resolution Cardiac Cine MRI from Retrospective Reconstruction of Data Acquired in Real Time Using Motion Correction and Resorting. *Magnetic Resonance in Medicine* **62,** 1557–1564 (2009).

40. Schmidt, J. F. M., Buehrer, M., Boesiger, P. & Kozerke, S. Nonrigid retrospective respiratory motion correction in whole-heart coronary MRA. *Magnetic Resonance in Medicine* **66,** 1541–1549 (2011).

41. Peters, D. C., Nezafat, R., Eggers, H., Stehning, C. & Manning, W. J. 2D Free-Breathing Dual Navigator-Gated Cardiac Function Validated Against the 2D Breath-Hold Acquisition. *Journal of Magnetic Resonance Imaging* **28,** 773–777 (2008).

42. Bush, M. A., Ahmad, R., Jin, N., Liu, Y. & Simonetti, O. P. Patient specific prospective respiratory motion correction for efficient, free-breathing cardiovascular MRI. *Magnetic Resonance in Medicine* **81,** 3662–3674 (2019).

43. Zaitsev, M., Dold, C., Sakas, G., Hennig, J. & Speck, O. Magnetic resonance imaging of freely moving objects: Prospective real-time motion correction using an external optical motion tracking system. *NeuroImage* **31,** 1038–1050 (2006).

44. Buehrer, M., Curcic, J., Boesiger, P. & Kozerke, S. Prospective self-gating for simultaneous compensation of cardiac and respiratory motion. *Magnetic Resonance in Medicine* **60,** 683–690 (2008).

45. Zaitsev, M., Maclaren, J. & Herbst, M. Motion Artifacts in MRI: A Complex Problem With Many Partial Solutions. *Journal of Magnetic Resonance Imaging* (2015).

46. Manke, D., Nehrke, K. & Börnert, P. Novel Prospective Respiratory Motion Correction Approach for Free-Breathing Coronary MR Angiography Using a Patient-Adapted Affine Motion Model. *Magnetic Resonance in Medicine* **50,** 122–131 (2003).

47. Nehrke, K. & Börnert, P. Prospective Correction of Affine Motion for Arbitrary MR Sequences on a Clinical Scanner. *Magnetic Resonance in Medicine* **54,** 1130–1138 (2005).

48. Manke, D., Bornert, P., Nehrke, K., Aldefeld, B. & Dossel, O. *Real-time Motion Correction of Linear Expansion in MRI by Navigator-based Gradient Scaling* in *Proceedings of the 8th Annual Meeting of ISMRM* (2000).

49. Aitken, A. P., Henningsson, M., Botnar, R. M., Schaeffter, T. & Prieto, C. 100% Efficient Three-Dimensional Coronary MR Angiography with Two-Dimensional Beat-to-Beat Translational and Bin-to-Bin Affine Motion Correction. *Magnetic Resonance in Medicine* **74,** 756–764 (2015).

50. Wang, Y., Riederer, S. J. & Ehman, R. L. Respiratory Motion of the Heart: Kinematics and the Implications for the Spatial Resolution in Coronary Imaging. *Magnetic Resonance in Medicine* **33,** 713–719 (1995).

51. Henningsson, M. & Botnar, R. M. Advanced Respiratory Motion Compensation for Coronary MR Angiography. *Sensors* **13,** 6882–6899 (2013).

52. Bhat, H., Ge, L., Nielles-Vallespin, S., Zuehlsdorff, S. & Li, D. 3D Radial Sampling and 3D Affine Transform-based Respiratory Motion Correction Technique for Free-breathing Whole-Heart Coronary MRA with 100% Imaging Efficiency. *Magnetic Resonance in Medicine* **65,** 1269–1277 (2011).

53. Pang, J. *et al.* Whole-Heart Coronary MRA with 100% Respiratory Gating Efficiency : Self-Navigated Three-Dimensional Retrospective Image-Based Motion Correction (TRIM). *Magnetic Resonance in Medicine* **71,** 67–74 (2014).

54. Luo, J. *et al.* Nonrigid Motion Correction With 3D Image-Based Navigators for Coronary MR Angiography. *Magnetic Resonance in Medicine* **77,** 1884–1893 (2017).

55. Prieto, C. *et al.* Highly efficient respiratory motion compensated free-breathing coronary MRA using golden-step Cartesian acquisition. *Journal of Magnetic Resonance Imaging* **41,** 738–746 (2015).

56. Manke, D., Nehrke, K., Börnert, P., Rösch, P. & Dössel, O. Respiratory Motion in Coronary Magnetic Resonance Angiography: A Comparison of Different Motion Models (2002).

57. Batchelor, P. G. *et al.* Matrix Description of General Motion Correction Applied to Multishot Images. *Magnetic Resonance in Medicine* **54,** 1273–1280 (2005).

58. Hansen, M. S., Sørensen, T. S., Arai, A. E. & Kellman, P. Retrospective Reconstruction of High Temporal Resolution Cine Images from Real-Time MRI Using Iterative Motion Correction. *Magnetic Resonance in Medicine* **68,** 741–750 (2012).

59. Pereira, C. B. *et al.* Remote monitoring of breathing dynamics using infrared thermography. *Biomedical Optics Express* **6** (2015).

60. Abbas, K., Heimann, K., Jergus, K., Orlikowsky, T. & Leonhardt, S. Neonatal non-contact respiratory monitoring based on real-time infrared thermography. *BioMedical Engineering Online* **10,** 1–17 (2011).

61. Krug, J. W., Odenbach, R., Boese, A. & Friebe, M. Contactless respiratory monitoring system for magnetic resonance imaging applications using a laser range sensor. *Current Directions in Biomedical Engineering* **2,** 719–722 (2016).

62. Kording, F. *et al.* Dynamic fetal cardiovascular magnetic resonance imaging using Doppler ultrasound gating. *Journal of Cardiovascular Magnetic Resonance* **20,** 1–10 (2018).

63. Neumann, T., Ludwig, J., Kerkering, K. M., Seifert, F. & Kolbitsch, C. *Ultra-wideband radar for respiratory motion correction of T1 mapping in the liver* in *Proceedings of the 9th Annual Meeting of ISMRM* (2021).

64. Thiel, F., Kosch, O. & Seifert, F. Ultra-Wideband Sensors for Improved Magnetic Resonance Imaging, Cardiovascular Monitoring and Tumour Diagnostics. *Sensors* **10,** 10778–10802 (2010).

65. Immoreev, I. & Tao, T. H. UWB Radar for Patient Monitoring. *IEEE Aerospace and Electronic Systems Magazine,* 11–18 (2008).

66. Kudielka, G., Hardy, C., Vuissoz, P.-A., Felblinger, J. & Brau, A. *Utilization of the receive coil for cardiovascular and respiratory motion representation* in *Proceedings of the 23th Annual Meeting of ISMRM, Toronto, Canada* (2015), 705.

67. Buikman, D., Helzel, T. & Röschmann, P. The RF Coil as a Sensitive Motion Detector for Magnetic Resonance Imaging. *Magnetic Resonance Imaging* **6,** 281–289 (1988).

68. Graesslin, I. *et al. Advancements in Contact-free Respiration Monitoring using RF Pick-up coils* in *Proceedings of the 18th Annual meeting of ISMRM* (2010).

69. Andreychenko, A. *et al.* Thermal Noise Variance of a Receive Radiofrequency Coil as a Respiratory Motion Sensor. *Magnetic Resonance in Medicine* **77,** 221–228 (2017).

70. Navest, R. J., Andreychenko, A., Lagendijk, J. J. & Van Den Berg, C. A. *Prospective Respiration Detection in Magnetic Resonance Imaging by a non-interfering Noise Navigator* in *IEEE Transactions on Medical Imaging* (2018).

71. Andreychenko, A. *et al. Noise variance of an RF receive array reflects respiratory motion: a novel respiratory motion predictor* in *Proceedings of the 22th Annual Meeting of ISMRM* (2014).

72. Ma, L. E. *et al.* 5D Flow MRI: A Fully Self-gated, Free-running Framework for Cardiac and Respiratory Motion–resolved 3D Hemodynamics. *Radiology: Cardiothoracic Imaging* **2** (2020).

73. Glover, G. H. & Lai, S. Self-Navigated Spiral fMRI: Interleaved versus Single-shot. *Magnetic Resonance in Medicine* **39,** 361–368 (1998).

74. Piccini, D., Littmann, A., Nielles-Vallespin, S. & Zenge, M. O. Respiratory Self-Navigation for Whole-Heart Bright-Blood Coronary MRI: Methods for Robust Isolation and Automatic Segmentation of the Blood Pool. *Magnetic Resonance in Medicine* **68,** 571–579 (2012).

75. Henningsson, M., Smink, J., van Ensbergen, G. & Botnar, R. Coronary MR Angiography Using Image-Based Respiratory Motion Compensation With In-line Correction and Fixed Gating Efficiency. *Magnetic Resonance in Medicine* **79,** 416–422 (2018).

76. Uribe, S. *et al.* Whole-Heart Cine MRI Using Real-Time Respiratory Self-Gating. *Magnetic Resonance in Medicine* **57,** 606–613 (2007).

77. Ehman, R. L. & Felmlee, J. P. Adaptive Technique for High-Definition MR Imaging of Moving Structures. *Radiology* **173,** 255–263 (1989).

78. Danias, P. G. *et al.* Prospective Navigator Correction of Image Position for Coronary MR Angiography. *Radiology* **203,** 733–736 (1997).

79. Nehrke, K. & Manke, D. Advanced Navigator Techniques. *International Journal of Bioelectromagnetism* **2** (2000).

80. Larson, A. C. *et al.* Preliminary Investigation of Respiratory Self-Gating for Free-Breathing Segmented Cine MRI. *Magnetic Resonance in Medicine* **53,** 159–168 (2005).

81. Scott, A. D., Keegan, J. & Firmin, D. N. Beat-to-beat respiratory motion correction with near 100% efficiency: A quantitative assessment using high-resolution coronary artery imaging. *Magnetic Resonance Imaging* **29,** 568–578 (2011).

82. Bonanno, G. *et al.* Self-Navigation with Compressed Sensing for 2D Translational Motion Correction in Free-Breathing Coronary MRI: A Feasibility Study. *PLoS ONE* **9** (2014).

83. Henningsson, M., Smink, J., Razavi, R. & Botnar, R. M. Prospective Respiratory Motion Correction for Coronary MR Angiography Using a 2D Image Navigator. *Magnetic Resonance in Medicine* **69,** 486–494 (2013).

84. Cassar, A., Holmes, D. R., Rihal, C. S. & Gersh, B. J. Chronic Coronary Artery Disease: Diagnosis and Management. *Mayo Clinic Proceedings* **84,** 1130–1146 (2009).

85. Finegold, J. A., Asaria, P. & Francis, D. P. Mortality from ischaemic heart disease by country, region, and age: Statistics from World Health Organisation and United Nations. *International Journal of Cardiology* **168,** 934–945 (2013).

86. Grothues, F. *et al.* Comparison of Interstudy Reproducibility of Cardiovascular Magnetic Resonance With Two-Dimensional Echocardiography in Normal Subjects and in Patients With Heart Failure or Left Ventricular Hypertrophy. *The American Journal of Cardiology* **90,** 29–34 (2002).

87. Groeneveld, N. S. *et al.* CT angiography vs echocardiography for detection of cardiac thrombi in ischemic stroke: a systematic review and meta-analysis. *Journal of Neurology* **267,** 1793–1801 (2020).

88. Sakuma, H. Coronary CT versus MR Angiography: The Role of MR Angiography. *Radiology* **258,** 340–349 (2011).

89. *COR MEDICAL GROUP, Coronary Artery Disease, Heart with Muscle Damage and a Blocked Artery, URL: https://www.cormedicalgroup.com/conditions/coronary-artery-disease/, [Online accessed: 2021/12/03, 14:58]*

90. Chang, S. A. & Kim, R. J. The use of cardiac magnetic resonance in patients with suspected coronary artery disease: A clinical practice perspective. *Journal of Cardiovascular Ultrasound* **24,** 96–103 (2016).

91. Zidi, A. *et al.* Value of Cine-MRI sequences before and after injection in the diagnosis of acute myocarditis. *La Tunisie Medicale* **94,** 469–473 (2016).

92. Natarajan, A., Nyktari, E., Baksi, A. J., Kindler, H. E. & Kilner, P. J. Cine acquisition strategies for visualizing atrial septal defects by CMR. *Journal of Cardiovascular Magnetic Resonance* **15,** 1–2 (2013).

93. Carr, J. C. *et al.* Cine MR Angiography of the Heart with Segmented True Fast Imaging with Steady-State Precession. *Radiology* **219,** 828–834 (2001).

94. Bradley, W., Waluch, V., Lai, K.-S., Fernandez, E. & Spalter, C. The Appearance of Rapidly Flowing Blood on Magnetic Resonance Images. *American Journal of Roentgenology* **143,** 1167–1174 (1984).

95. Hudsmith, L. E. *et al.* Determination of Cardiac Volumes and Mass with FLASH and SSFP Cine Sequences at 1.5 vs. 3 Tesla: A Validation Study. *Journal of Magnetic Resonance Imaging* **24,** 312–318 (2006).

96. Edelman, R. R., Wallner, B., Singer, A., Atkinson, D. J. & Saini, S. Segmented TurboFLASH: Method for Breath-Hold MR Imaging of the Liver with Flexible Contrast. *Radiology* **177,** 515–521 (1990).

97. McRobbie, D. W., Moore, E. A., Graves, M. J. & Prince, M. R. *MRI: From Picture to Proton* Second. ISBN: 9780521865272 (2017).

98. Rumberger, J. A. *et al.* Determination of Ventricular Ejection Fraction: A Comparison of Available Imaging Methods. *Mayo Clinic Proceedings* **72,** 860–870 (1997).

99. Verhaert, D. *et al.* Direct T2 Quantification of Myocardial Edema in Acute Ischemic Injury. *JACC Cardiovascular Imaging* **4,** 269–278 (2011).

100. Triadyaksa, P., Oudkerk, M. & Sijens, P. E. Cardiac T2* Mapping: Techniques and Clinical Applications. *Journal of Magnetic Resonance Imaging* **52,** 1340–1351 (2020).

101. Hinderer, S. & Schenke-Layland, K. Cardiac fibrosis – A short review of causes and therapeutic strategies. *Advanced Drug Delivery Reviews* **146,** 77–82 (2019).

102. McKenna, W. J., Maron, B. J. & Thiene, G. Classification, Epidemiology, and Global Burden of Cardiomyopathies. *Circulation Research* **121,** 722–730 (2017).

103. Villari, B. *et al.* Influence of Collagen Network on Left Ventricular Systolic and Diastolic Function in Aortic Valve Disease. *Journal of the American College of Cardiology* **22,** 1477–1484 (1993).

104. Hanlon, R. O. *et al.* Prognostic Significance of Myocardial Fibrosis in Hypertrophic Cardiomyopathy. *Journal of the American College of Cardiology* **56,** 867–874 (2010).

105. Burt, J. R., Zimmerman, S. L., Kamel, I. R., Halushka, M. & Bluemke, D. A. Myocardial T1 Mapping: Techniques and Potential Applications. *Radiographics* **34,** 377–395 (2014).

106. Kim, R. *et al.* The Use of Contrast-Enhanced Magnetic Resonance Imaging to Identify Reversible Myocardial Dysfunction. *New England Journal of Medicine* **343,** 1445–1453 (2000).

107. Haaf, P. *et al.* Cardiac T1 Mapping and Extracellular Volume (ECV) in clinical practice: A comprehensive review. *Journal of Cardiovascular Magnetic Resonance* **18,** 1–12 (2016).

108. Hamlin, S. A., Henry, T. S., Little, B. P., Lerakis, S. & Stillman, A. E. Mapping the Future of Cardiac MR Imaging: Case-based Review of T1 and T2 Mapping Techniques. *Radiographics* **34,** 1594–1612 (2014).

109. Aherne, E., Chow, K. & Carr, J. Cardiac T1 mapping: Techniques and Applications. *Journal of Magnetic Resonance Imaging* **51,** 1336–1356 (2020).

110. Taylor, A. J., Salerno, M., Dharmakumar, R. & Jerosch-Herold, M. T1 Mapping: Basic Techniques and Clinical Applications. *Journal of the American College of Cardiology* **9,** 67–81 (2016).

111. Everett, R. J. *et al.* Assessment of myocardial fibrosis with T1 mapping MRI. *Clinical Radiology* **71,** 768–778 (2016).

112. Look, D. C. & Locker, D. R. Time Saving in Measurement of NMR and EPR Relaxation Times. *The Review of Scientific Instruments* **41,** 250–251 (1970).

113. Deichmann, R. & Haase, A. Quantification of T1 Values by SNAPSHOT-FLASH NMR Imaging. *Journal of Magnetic Resonance* **96,** 608–612 (1992).

114. Messroghli, D. R. *et al.* Modified Look-Locker Inversion Recovery (MOLLI) for High-Resolution T1 Mapping of the Heart. *Magnetic Resonance in Medicine* **52,** 141–146 (2004).

115. Kellman, P. & Hansen, M. S. T1-mapping in the heart: accuracy and precision. *Journal of Cardiovascular Magnetic Resonance* **16,** 1–20 (2014).

116. Sass, M. & Ziessow, D. Error Analysis for Optimized Inversion Recovery Spin-Lattice Relaxation Measurements. *Journal of Magnetic Resonance* **25,** 263–276 (1977).

117. Nekolla, S., Gneiting, T., Syha, J., Deichmann, R. & Haase, A. T1 Maps by K-Space Reduced Snapshot-FLASH MRI. *Journal of Computer Assisted Tomography* **16,** 327–332 (1992).

118. Piechnik, S. K. *et al.* Shortened Modified Look-Locker Inversion recovery (ShMOLLI) for clinical myocardial T1-mapping at 1.5 and 3 T within a 9 heartbeat breathhold. *Journal of Cardiovascular Magnetic Resonance* **12,** 1–11 (2010).

119. Baudrexel, S., Noeth, U., Schuere, J.-R. & Deichmann, R. T1 Mapping With the Variable Flip Angle Technique: A Simple Correction for Insufficient Spoiling of Transverse Magnetization. *Magnetic Resonance in Medicine* **79,** 3082–3092 (2018).

120. Chow, K. *et al.* Saturation Recovery Single-Shot Acquisition (SASHA) for Myocardial T1 Mapping. *Magnetic Resonance in Medicine* **71,** 2082–2095 (2014).

121. Schröter, S., Bollenbeck, J., Fenchel, M., Speier, P. & Vester, M. *Patent US 2017/0160367 A1* 2017.

122. Bacher, M., Dornberger, B., Bollenbeck, J., Stuber, M. & Speier, P. *Listening in on the Pilot Tone: A Simulation Study* in *Proceedings of the 29th Annual meeting of ISMRM* (2021), 1364.

123. Schroeder, L. *et al. A Novel Method for Contact-Free Cardiac Synchronization Using the Pilot Tone Navigator* in *Proceedings of the 24th Annual Meeting of ISMRM* (2016), 0410.

124. Vahle, T. *et al. PET-MR Motion Correction of Entire Listmode Data Sets Using Pilot Tone Navigation* in *Proceedings of the 25th Annual Meeting of ISMRM* (2017), 3897.

125. Bacher, M., Speier, P., Bollenbeck, J., Fenchel, M. & Stuber, M. *Model-Based Lag Free Processing of Pilot Tone Navigator Data Enables Prospective Cardiac Triggering* in *Proceedings of the 26th Annual Meeting of ISMRM* (2018), 4913.

126. Bacher, M. *et al. Retrospective Analysis of Pilot Tone Derived Cardiac and Respiratory Motion Information in a Patient Cohort* in *Proceedings of the 28th Annual Meeting of ISMRM* (2020), 1212.

127. Bacher, M., Speier, P., Bollenbeck, J., Fenchel, M. & Stuber, M. *Pilot Tone Navigation Enables Contactless Prospective Cardiac Triggering: Initial Volunteer Results for Prospective Cine* in *Proceedings of the 26th Annual Meeting of ISMRM* (2018), 2960.

128. Speier, P., Bacher, M., Bollenbeck, J., Fenchel, M. & Kober, T. *Separation And Quantification Of Head Motion Modes By Pilot Tone Measurements* in *Proceedings of Joint Annual Meeting ISMRM-ESMRMB, Paris, France* (2018), 4101.

129. Huang, S., Boyacioglu, R., Bolding, R., Chen, Y. & Griswold, M. A. *Free-Breathing Abdominal Magnetic Resonance Fingerprinting Using a Pilot Tone Navigator* in *Proceedings of the 28th Annual Meeting of ISMRM* (2020), 0458.

130. Anand, S. & Lustig, M. *Beat Pilot Tone: Exploiting Preamplifier Intermodulation of UHF/SHF RF for Improved Motion Sensitivity over Pilot Tone Navigators* in *Proceedings of the 29th Annual Meeting of ISMRM* (2021), 0568.

131. Navest, R. J. M. *et al.* Understanding the physical relations governing the noise navigator. *Magnetic Resonance in Medicine* **00,** 1–12 (2019).

132. Solomon, E. *et al.* Free-breathing radial imaging using a pilot-tone radiofrequency transmitter for detection of respiratory motion. *Magnetic Resonance in Medicine* **85,** 2672–2685 (2021).

133. Foussier, J., Teichmann, D., Jia, J., Misgeld, B. & Leonhardt, S. An adaptive Kalman filter approach for cardiorespiratory signal extraction and fusion of non-contacting sensors. *BMC Medical Informatics and Decision Making* **14,** 1–15 (2014).

134. Spincemaille, P., Nguyen, T. D., Prince, M. R. & Wang, Y. Kalman Filtering for Real-Time Navigator Processing. *Magnetic Resonance in Medicine* **60,** 158–168 (2008).

135. King, A., Rhode, K., Razavi, R. & Schaeffter, T. An Adaptive and Predictive Respiratory Motion Model for Image-Guided Interventions: Theory and First Clinical Application. *IEEE Transactions on Medical Imaging* **28,** 2020–2032 (2009).

136. Von Knobelsdorff, F. *et al.* Sicherheit von nicht-aktiven kardiovaskulären Implantaten bei MRT-Untersuchungen – Update 2021. *Der Kardiologe* **15,** 262–271 (2021).

137. Niendorf, T. *et al.* Toward Single Breath-Hold Whole-Heart Coverage Coronary MRA Using Highly Accelerated Parallel Imaging With a 32-Channel MR System. *Magnetic Resonance in Medicine* **56,** 167–176 (2006).

138. Pednekar, A. S., Wang, H., Flamm, S., Cheong, B. Y. & Muthupillai, R. Two-center clinical validation and quantitative assessment of respiratory triggered retrospectively cardiac gated balanced-SSFP cine cardiovascular magnetic resonance imaging in adults. *Journal of Cardiovascular Magnetic Resonance* **20,** 1–11 (2018).

139. Paul, J. *et al.* High-Resolution Respiratory Self-Gated Golden Angle Cardiac MRI: Comparison of Self-Gating Methods in Combination with k-t SPARSE SENSE. *Magnetic Resonance in Medicine* **73,** 292–298 (2015).

140. King, A. P., Buerger, C., Tsoumpas, C., Marsden, P. K. & Schaeffter, T. Thoracic Respiratory Motion Estimation from MRI using a Statistical Model and a 2-D Image Navigator. *Medical Image Analysis* **16,** 252–264 (2012).

141. Hoogeman, M. *et al.* Clinical Accuracy of the Respiratory Tumor Tracking System of the CyberKnife: Assessment by Analysis of Log Files. *International Journal of Radiation Oncology Biol. Phys.* **74,** 297–303 (2009).

142. Von Siebenthal, M. *et al.* 4D MR imaging of respiratory organ motion and its variability. *Physics in Medicine and Biology* **52,** 1547–1564 (2007).

143. Peressutti, D., Rijkhorst, E., Barratt, D. C., Penney, G. P. & King, A. P. *Estimating and Resolving Uncertainty in Cardiac Respiratory Motion Modelling* in *9th IEEE International Symposium on Biomedical Imaging (ISBI)* (2012), 262–265.

144. Baumgartner, C. F., Kolbitsch, C., McClelland, J. R., Rueckert, D. & King, A. P. Autoadaptive motion modelling for MR-based respiratory motion estimation. *Medical Image Analysis* **35,** 83–100 (2017).

145. *NiftyReg. 2020. Available at: https://github.com/KCL-BMEIS/niftyreg [Online accessed: 2021/02/28, 9:53]*

146. Etienne, A. *et al.* "Soap-Bubble" Visualization and Quantitative Analysis of 3D Coronary Magnetic Resonance Angiograms. *Magnetic Resonance in Medicine* **48,** 658–666 (2002).

147. King, A. P. *et al.* A subject-specific technique for respiratory motion correction in image-guided cardiac catheterisation procedures. *Medical Image Analysis* **13,** 419–431 (2009).

148. Plein, S., Ridgway, J. P., Jones, T. R., Bloomer, T. N. & Sivananthan, M. U. Coronary Artery Disease: Assessment with a Comprehensive MR Imaging Protocol—Initial Results. *Radiology* **225,** 300–307 (2002).

149. Uecker, M., Zhang, S. & Frahm, J. Nonlinear Inverse Reconstruction for Real-Time MRI of the Human Heart Using Undersampled Radial FLASH. *Magnetic Resonance in Medicine* **63,** 1456–1462 (June 2010).

150. Nakamura, M. *et al.* Free-breathing real-time cardiac cine MR for evaluation of left-ventricular function: Comparison to standard multi-breath-hold cardiac cine MR in 50 patients. *Journal of Cardiovascular Magnetic Resonance* **18,** Q50 (Dec. 2016).

151. Pruessmann, K. P., Weiger, M., Scheidegger, M. B. & Boesiger, P. SENSE: Sensitivity Encoding for Fast MRI. *Magnetic Resonance in Medicine* **42,** 952–962 (1999).

152. Botnar, R. M., Stuber, M., Danias, P. G., Kissinger, K. V. & Manning, W. J. Improved Coronary Artery Definition With T2-Weighted, Free-Breathing, Three-Dimensional Coronary MRA. *Circulation* **99,** 3139–3148 (1999).

153. Cruz, G., Atkinson, D., Buerger, C., Schaeffter, T. & Prieto, C. Accelerated Motion Corrected Three-Dimensional Abdominal MRI Using Total Variation Regularized SENSE Reconstruction. *Magnetic Resonance in Medicine* **75,** 1484–1498 (2016).

154. Piccini, D. *et al.* Respiratory Self-navigated Postcontrast Whole-Heart Coronary MR Angiography: Initial Experience in Patients. *Radiology* **270,** 378–386 (2014).

155. Frauenrath, T. *et al.* Acoustic cardiac triggering: a practical solution for synchronization and gating of cardiovascular magnetic resonance at 7 Tesla. *Journal of Cardiovascular Magnetic Resonance* **12,** 1–14 (2010).

156. Nehrke, K., Börnert, P., Manke, D. & Böck, J. C. Free-breathing Cardiac MR Imaging: Study of Implications of Respiratory Motion—Initial Results. *Radiology* **220,** 810–815 (2001).

157. Kolbitsch, C. *et al.* Cardiac and Respiratory Motion Correction for Simultaneous Cardiac PET/MR. *The Journal of Nuclear Medicine* **58,** 846–852 (May 2017).

158. Jaubert, O. *et al.* Free-running cardiac magnetic resonance fingerprinting: Joint T1/T2 map and Cine imaging. *Magnetic Resonance Imaging* **68,** 173–182 (2020).

159. Becker, K. M., Schulz-Menger, J., Schaeffter, T. & Kolbitsch, C. Simultaneous high-resolution cardiac T1 mapping and cine imaging using model-based iterative image reconstruction. *Magnetic Resonance in Medicine* **00,** 1–12 (2018).

160. Messroghli, D. R. *et al.* Human myocardium: Single-breath-hold MR T1 mapping with high spatial resolution - Reproducibility study. *Radiology* **238,** 1004–1012 (2006).

161. Schelbert, E. B. & Messroghli, D. R. State of the Art: Clinical Applications of Cardiac T1 Mapping. *Radiology* **278,** 658–676 (2016).

162. Schulz-Menger, J. & Friedrich, M. G. Magnetic Resonance Imaging in Patients with Cardiomyopathies: When and Why. *Herz* **25,** 384–391 (2000).

163. Von Knobelsdorff-Brenkenhoff, F. & Schulz-Menger, J. Cardiovascular Magnetic Resonance Imaging in Ischemic Heart Disease. *Journal of Magnetic Resonance Imaging* **36,** 20–38 (2012).

164. Radunski, U. K. *et al.* CMR in patients with severe myocarditis: Diagnostic value of quantitative tissue markers including extracellular volume imaging. *JACC: Cardiovascular Imaging* **7,** 667–675 (2014).

165. Mewton, N., Liu, C. Y., Croisille, P., Bluemke, D. & Lima, J. A. Assessment of Myocardial Fibrosis With Cardiovascular Magnetic Resonance. *Journal of the American College of Cardiology* **57,** 891–903 (2011).

166. Fontana, M. *et al.* Native T1 mapping in Transthyretin Amyloidosis. *Journal of the American College of Cardiology* **7,** 157–165 (2014).

167. Sado, D. M. *et al.* Noncontrast Myocardial T1 Mapping Using Cardiovascular Magnetic Resonance for Iron Overload. *Journal of Magnetic Resonance Imaging* **41,** 1505–1511 (2015).

168. Jerosch-Herold, M. *et al.* Cardiac magnetic resonance imaging of myocardial contrast uptake and blood flow in patients affected with idiopathic or familial dilated cardiomyopathy. *American Journal of Physiology - Heart and Circulatory Physiology* **295,** 1234–1242 (2008).

169. Ugander, M. *et al.* Quantitative T1-maps delineate myocardium at risk as accurately as T2-maps - experimental validation with microspheres. *Journal of Cardiovascular Magnetic Resonance* **13,** O62 (2011).

170. Chow, K., Yang, Y., Shaw, P., Kramer, C. M. & Salerno, M. Robust free-breathing SASHA T1 mapping with high-contrast image registration. *Journal of Cardiovascular Magnetic Resonance* **18,** 1–14 (2016).

171. Roujol, S. *et al.* Accuracy, Precision, and Reproducibility of Four T1 Mapping Sequences: A Head-to-Head Comparison of MOLLI, ShMOLLI, SASHA, and SAPPHIRE. *Radiology* **272,** 683–689 (2014).

172. Xue, H. *et al.* Phase-Sensitive Inversion Recovery for Myocardial T1 Mapping with Motion Correction and Parametric Fitting. *Magnetic Resonance in Medicine* **69,** 1408–1420 (2013).

173. Shaw, J. L. *et al.* Free-breathing, non-ECG, continuous myocardial T1 mapping with cardiovascular magnetic resonance multitasking. *Magnetic Resonance in Medicine* **81,** 2450–2463 (2019).

174. Roujol, S. *et al.* Impact of motion correction on reproducibility and spatial variability of quantitative myocardial T2 mapping. *Journal of Cardiovascular Magnetic Resonance* **17,** 1–11 (2015).

175. Weingärtner, S., Roujol, S., Akçakaya, M., Basha, T. A. & Nezafat, R. Free-Breathing Multislice Native Myocardial T1 Mapping Using the Slice-Interleaved T1 (STONE) Sequence. *Magnetic Resonance in Medicine* **74,** 115–124 (2015).

176. Becker, K. M. *et al.* Fast myocardial T1 mapping using cardiac motion correction. *Magnetic Resonance in Medicine* **00,** 1–14 (2019).

177. Rueckert, D. *et al.* Nonrigid Registration Using Free-Form Deformations: Application to Breast MR Images. *IEEE Transactions on Medical Imaging* **18,** 712–721 (1999).

178. Buerger, C., Clough, R. E., King, A. P., Schaeffter, T. & Prieto, C. Nonrigid Motion Modeling of the Liver From 3-D Undersampled Self-Gated Golden-Radial Phase Encoded MRI. *IEEE Transactions on Medical Imaging* **31,** 805–815 (Mar. 2012).

179. Block, K. T., Uecker, M. & Frahm, J. Undersampled Radial MRI with Multiple Coils. Iterative Image Reconstruction Using a Total Variation Constraint. *Magnetic Resonance in Medicine* **57,** 1086–1098 (2007).

180. Stanisz, G. J. *et al.* T1, T2 Relaxation and Magnetization Transfer in Tissue at 3T. *Magnetic Resonance in Medicine* **54,** 507–512 (2005).

181. Bojorquez, J. Z. *et al.* What are normal relaxation times of tissues at 3 T? *Magnetic Resonance Imaging* **35,** 69–80 (2016).

182. Plein, S., Greenwood, J. & Ridgway, J. P. *Cardiovascular MR Manual: Components of CMR Protocols* 195–233. ISBN: 9783319209395 (2015).

183. Captur, G. *et al.* A medical device-grade T1 and ECV phantom for global T1 mapping quality assurance - the T1 Mapping and ECV Standardization in cardiovascular magnetic resonance (T1MES) program. *Journal of Cardiovascular Magnetic Resonance* **18,** 1–20 (2016).

184. Kellman, P., Herzka, D. A. & Hansen, M. S. Adiabatic Inversion Pulses for Myocardial T1 Mapping. *Magnetic Resonance in Medicine* **71,** 1428–1434 (2014).

185. Cerqueira, M. D. *et al.* Standardized Myocardial Segmentation and Nomenclature for Tomographic Imaging of the Heart: A Statement for Healthcare Professionals From the Cardiac Imaging Committee of the Council on Clinical Cardiology of the American Heart Association. *Circulation* **105,** 539–542 (2002).

186. Messner, N. M. *et al.* Saturation-Recovery Myocardial T1-Mapping during Systole: Accurate and Robust Quantification in the Presence of Arrhythmia. *Scientific Reports* **8,** 1–9 (2018).

187. Fischer, R. W. *et al.* Analysis of Residual Coronary Artery Motion for Breath Hold and Navigator Approaches Using Real-Time Coronary MRI. *Magnetic Resonance in Medicine* **55,** 612–618 (2006).

188. Falcão, M. B. *et al.* Pilot tone navigation for respiratory and cardiac motion-resolved free-running 5D flow MRI. *Magnetic Resonance in Medicine* **00,** 1–15 (2021).

List of Author's Publications

Journal Articles

J1 **Ludwig J**, Speier P, Seifert F, Schaeffter T, Kolbitsch C. Pilot tone–based motion correction for prospective respiratory compensated cardiac cine MRI. *Magnetic Resonance in Medicine,* 2020;00:1–14. https://doi.org/10.1002/mrm.28580

J2 **Ludwig J**, Kerkering KM, Speier P, Schaeffter T, Kolbitsch C, Pilot tone-based prospective correction of respiratory motion for free-breathing myocardial T1 mapping, *Magnetic Resonance Materials in Physics, Biology and Medicine,* 2022. https://doi.org/10.1007/s10334-022-01032-4

J3 Dietrich S, Aigner C, Kolbitsch C, **Ludwig J**, Mayer J, Schmidt S, Schaeffter T, Schmitter S, 3D Free-breathing Multi-channel absolute B1+ Mapping in the Human Body at 7T , *Magnetic Resonance in Medicine,* 2020. https://doi.org/10.1002/mrm.28602

Conference Proceedings

C1 **Ludwig J**, Speier P, Seifert F, Schaeffter T, Kolbitsch C, Comparison of three surrogate-based respiratory motion correction methods for 3D high resolution cardiac MRI, *Proceedings of the 26th Annual Meeting of ISMRM, Paris, France,* 2018.

C2 **Ludwig J**, Speier P, Seifert F, Schaeffter T, Kolbitsch C, Pilot tone-based prospective respiratory motion correction for 2D cine cardiac MRI, *Proceedings of the 27th Annual Meeting of ISMRM, Montréal, Canada,* 2019.

C3 **Ludwig J**, Kerkering KM, Speier P, Seifert F, Schaeffter T, Kolbitsch C, Pilot tone–based respiratory motion correction for 2D myocardial T1 mapping, *Proceedings of the 28th Annual Meeting of ISMRM, virtual,* 2020.

C4 Dietrich S, Aigner C, **Ludwig J**, Mayer J, Schmidt S, Kolbitsch C, Schaeffter T, Schmitter S, Respiration-Resolved 3D Multi-Channel B1 mapping of the body at 7T, *Proceedings of the 28th Annual Meeting of ISMRM, virtual,* 2020.

C5 Neumann T, **Ludwig J**, Kerkering KM, Seifert F, Kolbitsch C, Ultra-wide-band radar for respiratory motion correction of T1 mapping in the liver, *Proceedings of the 29th Annual Meeting of ISMRM, virtual,* 2021.

C6 Neumann T, **Ludwig J**, Kerkering KM, Speier P, Seifert F, Kolbitsch C, Prospective respiratory motion correction for 2D T1-Mapping in the liver using ultra-wideband radar system, *Proceedings of the 30th Annual Meeting of ISMRM, London,* 2022, (accepted).

List of Figures

List of Tables